Driver drowsiness detection using the Human-tenna effect

BSc thesis

Mathieu Demeestere
Peter Nagy
Sanne Romijn

Technische Universiteit Delft

TU Delft

Driver drowsiness detection using the Humantenna effect

BSc thesis

by

Mathieu Demeestere
Peter Nagy
Sanne Romijn

Project duration:	April 21, 2025 – June 27, 2025
Student number:	5693691 – Mathieu Demeestere
	4937635 – Peter Nagy
	5168600 – Sanne Romijn
Supervisor:	Hany Ayad Bastawrous
Thesis committee:	Willem van Driel
	Tomás Manzaneque
	Hany Ayad Bastawrous
Date:	June 25, 2025

TU Delft

Abstract

Drowsy driving is a significant contributor to road accidents with existing detection technologies often falling short due to intrusiveness or environmental sensitivity. This thesis presents a non-invasive method for detecting driver alertness using the Humantenna effect: the phenomenon whereby the human body passively couples with ambient 50 Hz electromagnetic fields. By capacitively coupling the human body into a sensor in the vehicle's steering wheel, grip strength and hand placement can be continuously monitored without requiring any wearable devices.

This project involves experimental validation of the Humantenna effect in a controlled environment, modelling of capacitive coupling as a function of grip strength, and the development of a custom amplifier circuit to condition the signal. Results demonstrate a consistent and measurable relation between grip strength and the amplitude of the 50 Hz signal. An operational amplifier-based configuration was found to be the most suitable for reliable signal conditioning. A functional multi-sensor prototype was developed and evaluated, indicating that the system is suitable for indoor use and scalable for integration into vehicle systems.

Preface

This report was written as part of our Bachelors graduation project in Electrical Engineering at TU Delft. The project was proposed by Prof. Hany Ayad Bastawrous, whose guidance and expertise helped shape the direction of our research.

Our work focused on using the Humantenna effect to enable passive, non-invasive detection of grip on a steering wheel. The project combined elements of electronics, signal amplification, and human-device interaction, and required us to move from theoretical understanding to practical implementation and testing.

Working as a group allowed us to approach the problem from different perspectives and to share responsibilities across design, experimentation, and documentation. This collaboration helped us to develop both our technical knowledge and our teamwork skills.

The project challenged us in unexpected ways. It required creativity, adaptability, and perseverance, particularly when facing technical setbacks and interpreting complex signal behaviour. These challenges ultimately deepened our understanding and made the outcome all the more rewarding.

We would like to thank Prof. Bastawrous for proposing this project and for the consistent support throughout its development. We are also grateful to everyone who supported us along the way, both technically and personally. We would also like to express our gratitude to Egbert Bol for his years of educational support, which have enabled us to undertake this project as the finalization of our bachelor studies.

This project was a valuable learning experience and an important step in our academic journey.

Mathieu Demeestere
Peter Nagy
Sanne Romijn
Delft, June 2025

Contents

1 Introduction

Road traffic accidents remain a major global issue, causing approximately 1.19 million deaths and 20 to 50 million injuries annually [1]. Drowsy driving is a critical contributor, implicated in an estimated 20% of road accidents in the Netherlands [2]. This figure is likely underestimated, as drowsiness often goes unrecorded, misattributed to other violations such as running red lights or failing to yield the right of way [2]. A survey across 19 European countries revealed that 17% of drivers had fallen asleep at the wheel in the past two years; of these, 7% were involved in accidents, 13.2% required hospital care, and 2.6% resulted in fatalities [3].

Beyond the loss of life, drowsy driving also imposes substantial economic costs. In 2022, road crashes in the Netherlands cost an estimated 33 billion, which is about 3.4% of GDP covering medical services, insurance, legal fees, and lost productivity [4]. Given its estimated 20% share of all crashes, drowsiness likely accounts for a significant portion of this loss.

Drowsiness is a physiological state marked by an overwhelming urge to fall asleep, often caused by sleep deprivation, circadian rhythm disruptions, or sedating medications [5, 6]. It impairs reaction time, situational awareness, and decision-making [7]. Unlike intoxication, its onset is gradual and often goes unnoticed by the driver.

Current driver monitoring systems generally fall into three categories: vehicle-based, behavioural, and physiological [8]. Although vehicle-based and behavioural systems have seen some commercial adoption, they face limitations such as speed dependency and sensitivity to lighting conditions [9, 10, 11, 12]. Physiological systems, while more promising in terms of early detection and accuracy, typically require direct physical contact with the driver (e.g., EEG helmets, ECG electrodes), limiting their usability and acceptance in real-world driving contexts [13, 14].

To bridge this gap, this research explores a passive and non-invasive sensing approach based on the Humantenna effect: a phenomenon where the human body acts as an antenna, passively picking up ambient 50 Hz electromagnetic fields present in most environments [15, 16]. By embedding a simple wire-based sensor into the steering wheel, the system aims to detect grip strength and hand placement, which are subtle but measurable indicators of driver alertness [14].

The primary focus is to determine the feasibility of using this passive grip sensor to distinguish between touch and no-touch states and to quantify variations in grip strength. The system aims to provide continuous, real-time monitoring without requiring drivers to wear any additional hardware, thereby improving user acceptance and practicality.

The intended end-users are original equipment manufacturers (OEMs) within the automotive industry, who can integrate the sensor into vehicles at scale. This solution aims to complement existing monitoring technologies, offering a straightforward and scalable method to enhance driver safety and support

regulatory compliance [17].

This introduction sets the context and goals for the project, while detailed assumptions, functional and non-functional requirements, and design constraints are further specified in the following Programme of Requirements section in Chapter 2. Chapter 3 explains the Humantenna effect in depth and presents experimental validation in a controlled setup. Chapter 4 examines how different coupling methods influence signal quality and grip detection. Chapter 5 explores how grip strength can be quantified using the sensed signals. Chapter 6 discusses the design and evaluation of several amplifier circuits suited to this application. Chapter 7 details the prototype implementation and presents both simulated and real-world results. The report concludes with a discussion in Chapter 8 and a summary of key findings in Chapter 9.

2

Program of requirements

At its core, the product is a low-cost, passive grip sensor designed to detect driver awareness and drowsiness. The initial target market is original equipment manufacturers (OEMs) in the automotive industry, as this allows access to a large customer base and enables straightforward integration of the sensor directly into existing vehicle systems.

2.1. Assumptions

- The ambient electromagnetic environment is stable and contains consistent 50 Hz signals.
- The setup is in a controlled environment, minimizing external electromagnetic interferences.
- The user will not move excessively during measurement to minimize signal disruptions.

2.2. Mandatory requirements

2.2.1. Non-functional requirements

- The system must require no special or expensive equipment.
- The system must be non-invasive and require no wearable devices.
- The system must be passive, emitting no signals or radiation during operation.
- The hardware must be compatible with the input specifications of the signal processing system.

2.2.2. Functional requirements

- The system must continuously monitor the grip strength and position of the driver's hands on the steering wheel using the humantenna effect sensors embedded in the steering wheel.
- The hardware shall detect distinguishable grip strength variations corresponding to different applied forces.

2.3. Trade-off requirements

- The cost of the sensor and amplifier components should be minimized without significantly compromising signal quality.
- The hardware design should aim to minimize complexity to reduce manufacturing costs and improve reliability, even if this limits some advanced features.
- Sensor placement and setup should be as simple as possible, even if this leads to a slight decrease in measurement precision.

3

Concept

This chapter defines the Humantenna effect and presents experimental validation demonstrating that it occurs reliably within the context of our prototype system. In particular, we show that electrically coupling a human body to a measurement device, significantly increases the amplitude of ambient 50 Hz signals, confirming the feasibility of using this effect for passive, non-invasive sensing.

3.1. The Humantenna effect

The Humantenna effect describes the phenomenon whereby the human body acts as a passive antenna, coupling with ambient low-frequency electromagnetic fields, primarily the 50 Hz signals emitted by AC power infrastructure. These ambient fields induce a small voltage in the body, which can be measured when the person makes contact with a wire connected to a high-impedance amplifier [15].

The induced signal typically lies in the millivolt range [18] but can reach up to several volts peak-to-peak depending on environmental conditions. In our environment, we observed peak-to-peak amplitudes around 3 V, although this value can vary significantly from day to day. Notably, this effect requires no active transmission or wearable electronics and relies solely on the constant presence of the 50 Hz signal found in most indoor and vehicular environments. Because of its passive nature, the Humantenna effect is ideal for applications requiring minimal invasiveness and low hardware complexity.

3.2. Experimental confirmation in a controlled setup

To confirm the presence of the Humantenna effect in our system, we developed a test setup consisting of a conductive wire embedded in a prototype steering wheel and a connection to a high-impedance amplifier. The environment was controlled to minimize electromagnetic interference and to ensure the presence of a stable ambient 50 Hz signal.

Figure 3.1 shows a direct comparison between the signal amplitude when the sensor is untouched versus when a human hand is in contact with the conductive wire. The result demonstrates a substantial increase in the amplitude of the 50 Hz signal upon touch.

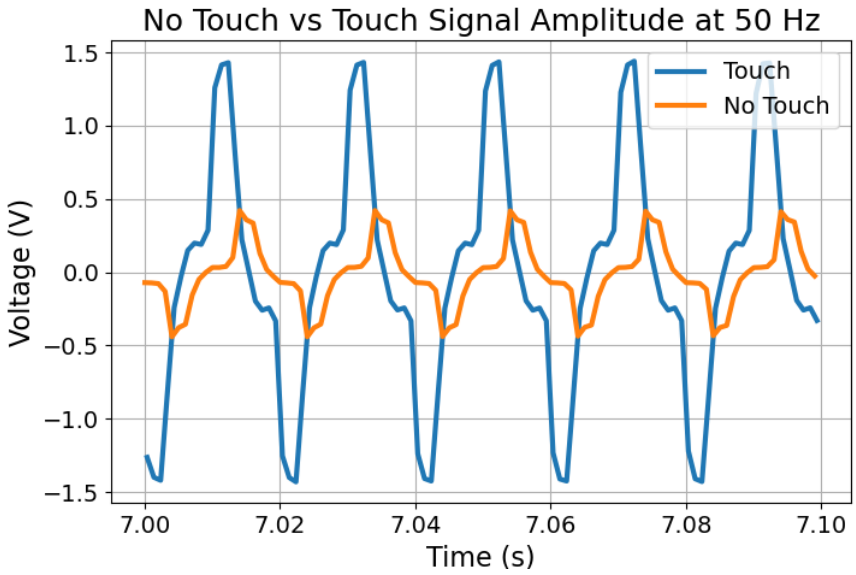

Figure 3.1: Measured 50 Hz signal amplitude: no-touch vs. touch

The high contrast between these two conditions confirms that the human body couples with the surrounding electromagnetic field and amplifies the induced voltage. This proves that the Humantenna effect is active and measurable in our setup using minimal hardware.

3.3. Implications for grip sensing

While this experiment focuses on confirming the presence of the Humantenna effect, it also establishes the foundation for using the effect to sense grip force. The dramatic signal change upon touch shows that contact conditions influence signal amplitude. In subsequent experiments, we explore whether variations in grip strength can be measured as distinct voltage changes. This lays the groundwork for developing a passive driver monitoring system based on touch-based interaction with the steering wheel.

4

Coupling

This chapter considers the coupling between the human palm and the device to measure grip strength. In this chapter, a simple model for the coupling will be derived.

According to the requirements in Chapter 2, the sensor also needs to be simple to integrate and non-invasive with respect to the driver.

4.1. Galvanic vs capacitive coupling

The first question to answer is whether to couple the driver to the sensor galvanically (direct sensor to skin contact) or capacitively (dielectric between the sensor and the skin).

In Table 4.1, three different couplings are tested with a test setup of the mentioned lengths of wire taped to a plastic cylindrical object. From these tests, it is clear that if the only goal is to detect presence, galvanic coupling is the correct approach. It has the highest detected signal of any of the sensors when touch is applied, and it does not depend on the length of the wire. The goal of this project is to detect drowsiness and this can be better derived from grip strength changes than solely touch detection. Since the capacitive coupling has a difference in signal when changing grip strength, that coupling was chosen.

The capacitive coupling is dependent on the length of the wire. It can be seen that with a longer wire, the ratio Weak Touch / No Touch is larger, and as such, it is easier to detect presence. However, the ratio Strong Grip / Weak Touch is lower, showing that shorter wire segments can be used for coupling, but possibly more amplification of the signal will be needed.

Table 4.1: Measured Voltage under Different Conditions and Coupling

Condition	Galvanic	Capacitive Short (8 cm)	Capacitive Long (36 cm)
No Touch [Vp]	0.25	0.15	0.20
Weak Touch [Vp]	2.30	0.24	0.75
Strong Grip [Vp]	2.30	0.49	1.40
Weak Touch / No Touch	9.20	1.60	3.75
Strong Grip / Weak Touch	1.00	2.04	1.87

4.2. Capacitive coupling in relation to grip strength

The Humantenna effect is based on how the human body picks up electric fields from the surrounding environment, particularly those generated by 50 Hz power lines (see section 3.1). To understand and work with this effect, a simple model is needed that captures how the body interacts with these fields at such low frequencies. Electric fields at 50 Hz change slowly. Thus, magnetic or radio-like effects can safely be ignored and the focus is on how the system behaves like a network of capacitors. In this setup,

it's not actual current flowing through wires that matters, but the tiny displacement currents caused by changing electric fields. In Figure 4.1 the full model and its parts are depicted.

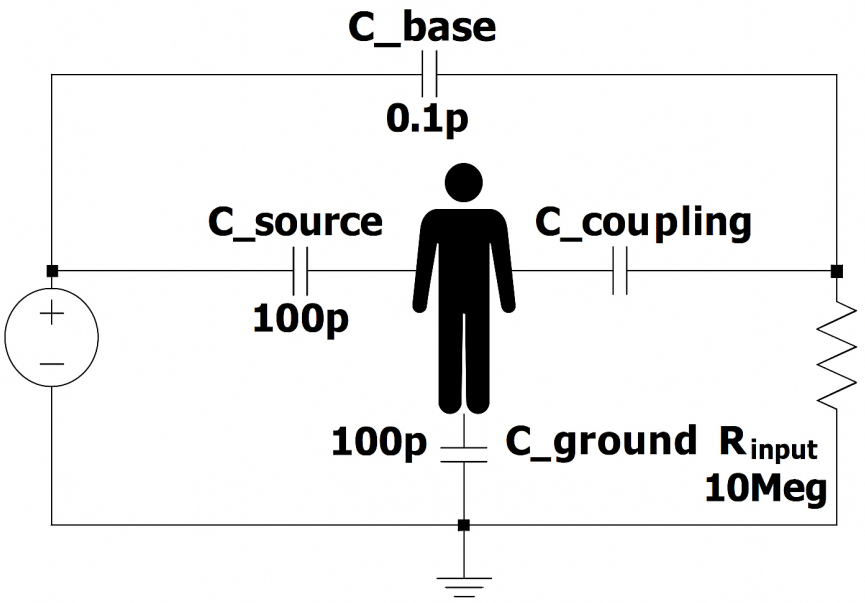

Figure 4.1: Full circuit representation of the model

The human body itself, while electrically complex, will be approximated as an equipotential conductor at these low frequencies, as its internal impedance becomes negligible relative to the high impedance of the capacitive coupling to external structures [19]. Thus, the body serves primarily as a conductor for transferring an electric-field-induced displacement current from the environment to a sensing wire.

The coupling between the human body and nearby power lines can be modelled as a capacitance, C_{source}, typically on the order of 100 pF [20]. This capacitance arises from the electrostatic interaction between the human body and the ambient electric field generated by power lines. Because the position and posture of the person relative to the power lines do not change significantly during the experiments, C_{source} can be considered constant for the given environment.

The body is then considered to be coupled to the ground with 100 pF capacitance C_{ground} [21]. These two capacitances, by applying Thevenin's theorem can be combined as 200 pF, and halving the source voltage.

The R_{input} is the input impedance of the measurement device. For the measurements, this was considered as $10\,\text{M}\Omega$ due to the oscilloscope probe's internal impedance.

The capacitance C_{base} is formed by the input of the measurement device and the power lines. This capacitance can be approximated by using the measurements of the insulated wire in the No Touch scenario showed in table 4.1. considering a voltage divider.

$$\frac{R_{\text{input}}}{R_{\text{input}} + Z_{C\text{base}}} \cdot V_{\text{source}} = V_{\text{No Touch}} \tag{4.1}$$

At 50 Hz, it is assumed that $X_{C\text{base}}$ will be so high that it will be dominant over R_{input}, thus solving for $X_{C\text{base}}$:

$$X_{C,\text{base}} = R_{\text{in}} \cdot \left(\frac{V_{\text{source}}}{V_{\text{No Touch}}} \right) = R10\,\text{M}\Omega \cdot \left(\frac{325\,\text{V}}{0.15\,\text{V}} \right) = 21.7\,\text{G}\Omega \tag{4.2}$$

$$C_{\text{base}} = \frac{1}{2\pi \cdot 50\,\text{Hz} \cdot 21.7\,\text{G}\Omega} \approx 0.1\,\text{pF} \tag{4.3}$$

4.2.1. Grip-dependent capacitance C_{coupling}

The second capacitance represents the coupling between the body, specifically the hand or palm, and the insulated wire, depicting in Figure 4.2. Unlike C_{source}, this capacitance is sensitive to how the user physically interacts with the wire. Factors such as:

- Grip force
- Tissue composition in the hand
- Contact area
- Insulation thickness and permittivity

All influence the effective capacitance C_{coupling}. When the hand lightly touches the insulation, the air gaps and reduced contact area result in a lower capacitance. As grip tightens, the contact area increases and the average separation distance decreases, increasing C_{coupling}, while the different tissues are moved around in the palm, changing the capacitance of the palm. This effect introduces a change in coupling: the signal strength at the wire changes depending on how firmly it is held.

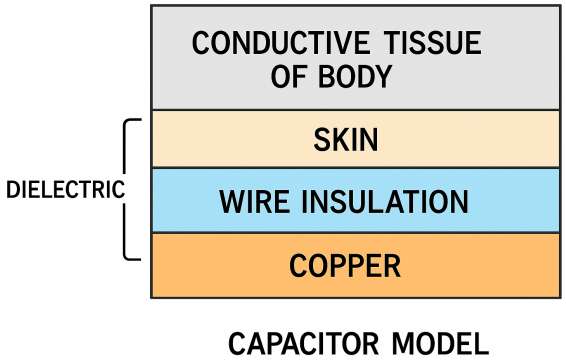

Figure 4.2: Capacitor model of palm and sensor.

4.2.2. Capacitor combination

Combining these two capacitors in series and connecting them to the measurement device will form a voltage divider together with the input impedance of the measurement device. This voltage is measured and compared with the grip strength. From Equation 4.4 it is visible that the lowest capacitance will always dominate the combined value.

$$C_{\text{eq}} = \frac{C_{\text{source}} \cdot C_{\text{coupling}}}{C_{\text{source}} + C_{\text{coupling}}} \approx C_{\text{coupling}} \tag{4.4}$$

4.2.3. The coupling capacitor

Taking into account the previous assumptions, the value for C_{coupling} can be approximated from the circuit depicted in Figure 4.3:

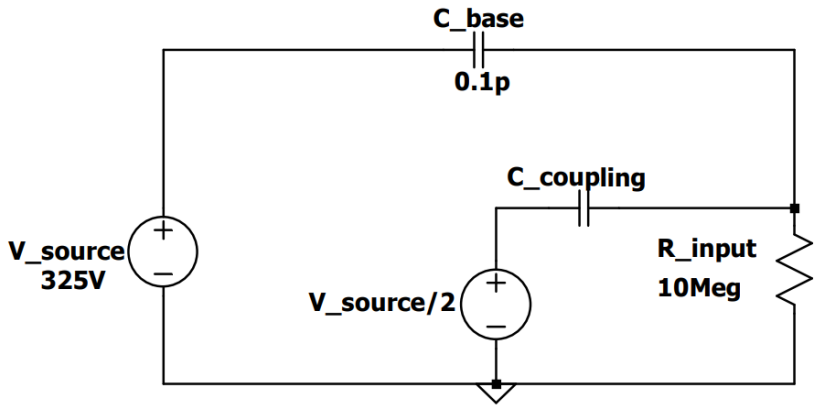

Figure 4.3: Simplified model with Thevenin equivalent

With superposition principle applied and R_{input} being a relatively low impedance, the equations for the calculation of C_{base} follows as:

$$X_{C\text{coupling}} = R_{\text{in}} \cdot \left(\frac{V_{\text{source}/2}}{V_{\text{Strong\_Grip}} - V_{\text{No\_Touch}}} \right) = 10\,\text{M}\Omega \cdot \left(\frac{325\,\text{V}}{0.49 - 0.15\,\text{V}} \right) = 4.8\,\text{G}\Omega \tag{4.5}$$

$$C_{\text{coupling}} = \frac{1}{2\pi \cdot 50\,\text{Hz} \cdot 4.8\,\text{G}\Omega} \approx 0.66\,\text{pF} \tag{4.6}$$

Table 4.2: Different capacitance values for the coupling

	Capacitive Short (8 cm)	Capacitive Long (36 cm)
No Touch [pF]	0.14	0.19
Weak Touch [pF]	0.17	1.08
Hard Grip [pF]	0.66	2.35

Through modelling and experimental validation, it was shown that the dominant variable capacitor in the system is the coupling between the user's palm and the insulated wire. This coupling capacitance, increases with grip force due to greater contact area (length of wire) and reduced dielectric spacing. The measured signal amplitude is compared with grip strength, and quantitative estimates show that varies from 0.14 pF (No Touch) to more than 2 pF (Hard Grip), depending on the length of the wire and the contact of the hand. This model gives a good indication of capacitance values, and thus voltage levels, to consider when conducting further measurements.

5

Quantifying grip strength

This chapter discusses the measurements performed to quantify how the Humantenna effect interacts with the coupling based on grip strength.

5.1. Why quantify

To accurately estimate the force applied during gripping, it is first necessary to understand how the sensor signal varies with grip strength and identify the relevant variables that influence the sensor-driver interaction. As described in Chapter 4, the measured voltage of the sensor is not solely dependent on grip force. It is also affected by external and individual-specific factors, including the strength of ambient 50 Hz electromagnetic fields, the body type of the person involved, and the composition of the hand. Therefore, to extract the part of the signal specifically related to grip force, a simultaneous measurement must be conducted using a separate sensor that directly reflects the force of the grip applied to the coupling. This dual-sensor approach allows for the comparison between the capacitive signal and actual grip force to be established, while also enabling an investigation into how body type and gender influence the interaction.

5.2. Test setup

In this test, to quantify grip strength, a grip strength item was designed using a Force Sensitive Resistor (FSR). While FSRs do not offer the greatest resolution or repeatability, they do offer a similar use case to the grip strength sensor, which is researched in this project. As such, the applied force to the sensors can be related, but with a large error margin.

The test item is a cylindrical object, shown in Figure 5.1, which the user can hold, and grip. It contains the FSR and the coupling for the Humantenna sensor. The force applied to the item is applied to the coupling for the hummantenna sensor, a 15 cm long insulated wire taped to the surface of the grip strength sensor, and transfers through the FSR located in the middle of the grip strength sensor, allowing it to directly measure the force applied. The compliant structure of the part allows the sensor to be placed in the item, but such that it can still move to transfer force and that the item only takes a predictable amount of force away from the grip.

Figure 5.1: Grip Strength Test Item

To test the device a single person conducted ten measurements within a short time period in the same location to keep the test environment constant. The measurements are plotted in Figure 5.2, where it is observable that there is a significant variation in the readouts. This is expected to be due to the repeatability constraints of the FSR.

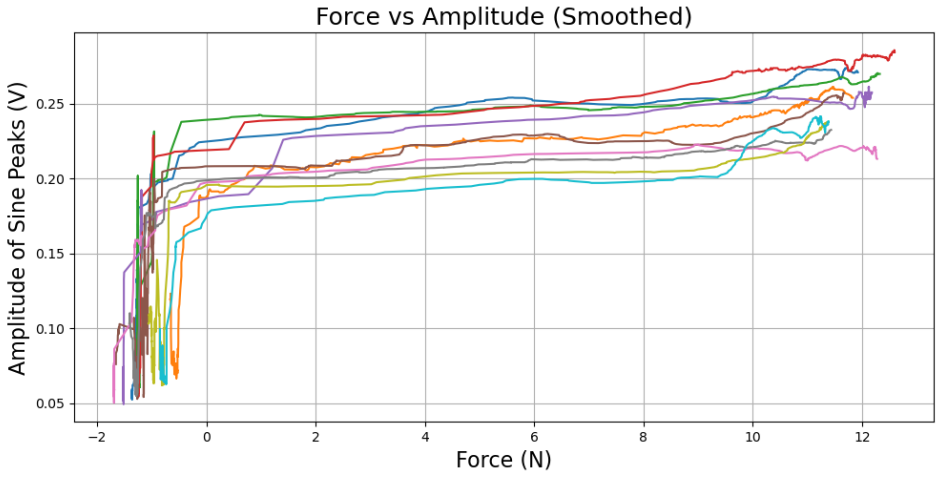

Figure 5.2: Test measurements of the same person ten times

Using this test item, multiple people were asked to first lightly hold, but do not touch, and then gradually grip the test item firmer for 15 seconds. Both the coupling's and the force sensor's output signals were noted. The voltage peaks of the 50 Hz signal were detected, then data was put into a Minimum Mean Squared Error, linear regression algorithm, from which a model was derived that allows to compare the grip strength and the Humantenna signal.

5.3. Results

The measurements with the grip strength item are plotted in Figure 5.3. The plot includes 11 recordings at the same location in the same controlled setting for 11 individuals, within the time period of one week.

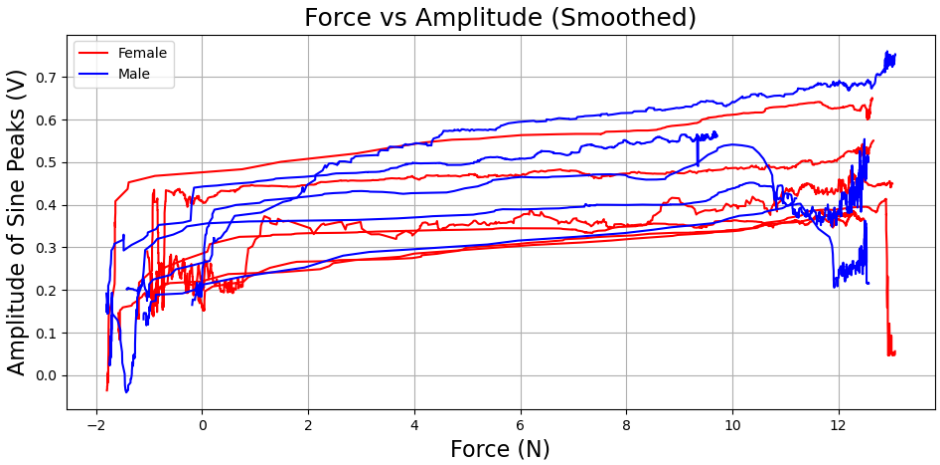

Figure 5.3: Controlled environment measurements of 11 individuals.

The horizontal axis in the plot represents the applied force as measured by the FSR. The vertical axis shows the amplitude of the 50 Hz component extracted from the voltage signal corresponding to 50 Hz radiation coupled through the body. Although the FSR used in this experiment showed limited precision and noticeable variance, a clear correlation is observed between the grip force and the amplitude of the induced 50 Hz signal.

Both male and female participants were included in the test, with red and blue lines representing individual measurements from female and male subjects, respectively. No significant differences in signal behaviour was observed between genders. When compared to Figure 5.2 it is also observable that there is more variance between measurements in test subjects than the variance caused by the grip strength test item.

Overall, the results support the conclusion that the amplitude of the induced signal increases with grip force, demonstrating a measurable and consistent relationship between physical contact force and the strength of the Humantenna effect. Quantitatively, signal amplitudes ranged from approximately 0.2 V at rest to over 0.7 V at maximum grip. For most subjects, especially beyond three Newtons of applied force, a roughly linear relationship is observed. The average slope across participants was approximately 0.03 to 0.05 V/N, though this varied due to sensor noise and hand placement.

6

Amplifier circuit design

This chapter evaluates and compares three amplifier configurations for enhancing bio-electrical signals in human-device interaction, specifically for detecting grip on a steering wheel using the Humantenna effect. Because the signals involved are low in amplitude, the application demands circuits with high sensitivity, stability, and linearity.
The amplifier topologies considered are:

1. The Tandem NPN/PNP Pair
2. The Sziklai Pair
3. A Non-Inverting Operational Amplifier (OpAmp) Configuration

Each circuit offers distinct characteristics in terms of gain, frequency response, linearity, and implementation complexity. While the tandem and Sziklai pairs are known for their high gain, the Op-Amp configuration provides accurate signal conditioning, active filtering, and is well-suited for integration with ADCs in microcontroller-based systems.

To assess their suitability for amplitude tracking, the designs are evaluated using a Harris Profile with criteria tailored to this context: amplitude linearity, gain stability, DC offset impact, saturation risk, signal loading, and bandwidth.

Through both simulation and experimental analysis, this chapter identifies the most effective amplifier configuration for reliable signal acquisition in bio-interactive sensing applications.

6.1. Various amplifier configurations

In previous experiments involving grip detection via the Humantenna effect, discrete transistor-based amplifiers such as the Tandem NPN/PNP pair and the Sziklai pair were implemented to amplify the weak bio-electrical signals produced by human contact [18, 14]. This section builds on that work by re-evaluating those two configurations and introducing a third approach: a non-inverting operational amplifier (OpAmp) circuit. All three designs are analysed and compared in terms of their signal amplification behaviour, with emphasis on their suitability for accurate, stable signal acquisition in bio-interactive sensing systems.

6.1.1. Tandem NPN/PNP pair

This configuration consists of a cascaded NPN and PNP transistor as shown in 6.1a [14], forming a simple but highly sensitive amplifier. Due to the complementary nature of the transistors, this circuit exhibits very high gain and is capable of amplifying the small input signals produced by the human body when in contact with the steering wheel.

However, this high gain comes at the cost of linearity. The Tandem pair shows strong non-linear behavior, with output signals often switching between the positive and negative supply rails. In simulation

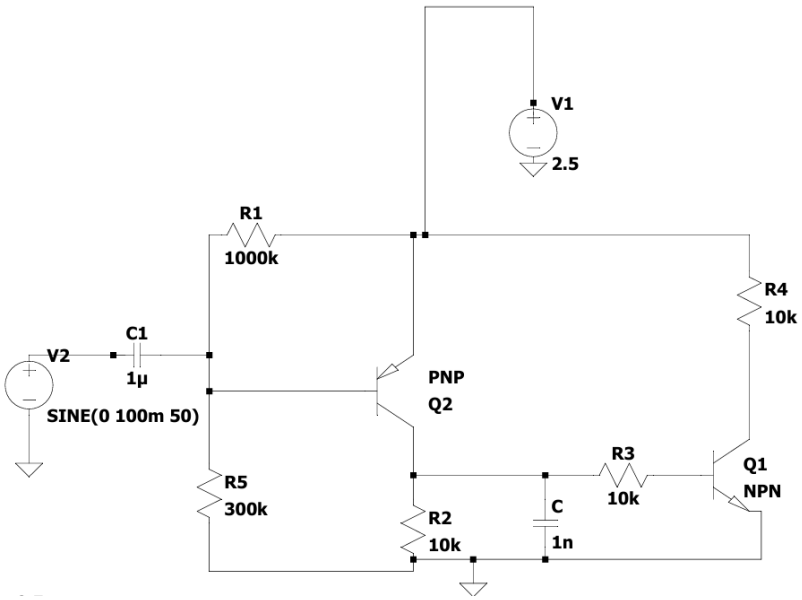

(a) Tandem NPN/PNP Pair configuration

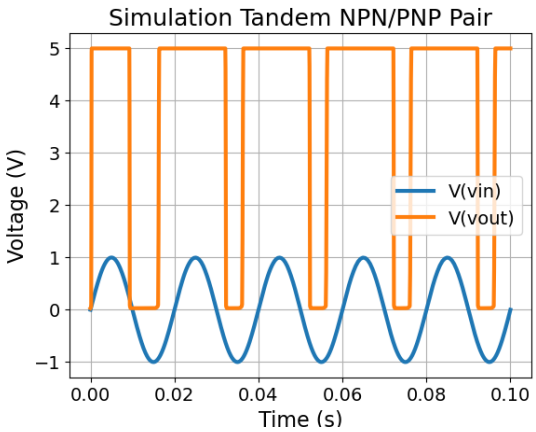

(b) Simulation Tandem NPN/PNP Pair

Figure 6.1: Tandem PNP/NPN Pair

and real-world measurements, this was observed as a form of saturation or "rail-to-rail" switching as can be seen in 6.1b, particularly for input signals near 1V peak-to-peak at 50 Hz. As a result, the output is less suitable for applications requiring accurate amplitude tracking.

Overall, the overall performance is hindered by its non-linearity and risk of clipping, especially in uncontrolled environments or with variable input amplitudes.

6.1.2. Sziklai pair

The Sziklai pair uses a similar arrangement of NPN and PNP transistors, but in a different configuration [18]. Unlike the Darlington pair, which multiplies current gain, the Sziklai pair offers high gain with improved thermal stability and lower base-emitter voltage drops. This makes it slightly more robust across varying environmental conditions.

Despite these advantages, the Sziklai pair also suffers from non-linear response and a limited linear output range. It does not include active filtering, meaning that additional circuitry would be required to limit the frequency range of the amplified signal. This makes it less optimal for integration into

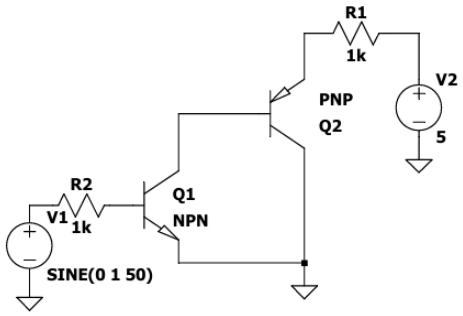

(a) Sziklai circuit configuration

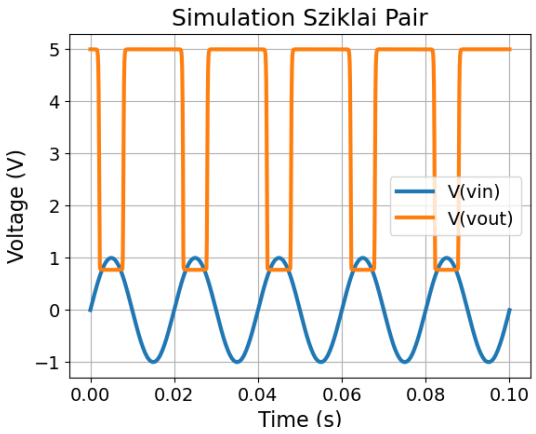

(b) Simulation Sziklai circuit

Figure 6.2: Tandem PNP/NPN Pair

systems requiring precise filtering and signal shaping.

Both the Tandem and Sziklai configurations are relatively simple and built from inexpensive discrete components, but their limitations in linearity, susceptibility to saturation, and inconsistent gain make them less suitable for applications demanding accurate signal fidelity, such as interfacing with analog-to-digital converters in microcontroller-based systems.

6.1.3. Operational amplifier

The non-inverting OpAmp amplifier was designed to condition the signal for digitization by a microcontrollers analog-to-digital converter (ADC). This approach combines high precision, flexibility, and simplicity, making it ideal for applications requiring accurate amplitude measurements.

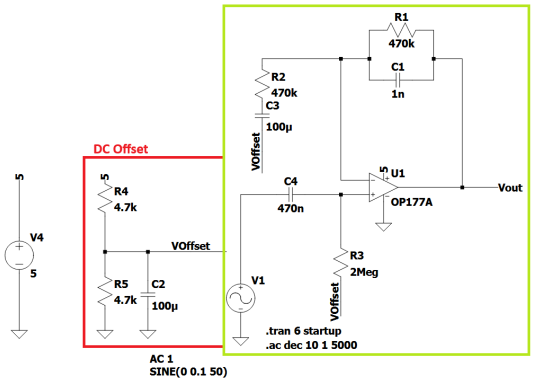

(a) Active filter OpAmp configuration

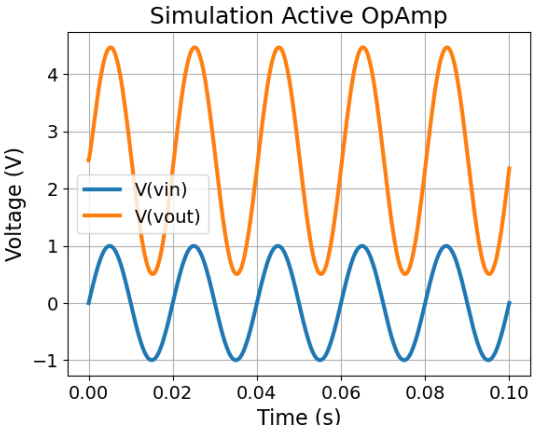

(b) Simulation Active filter OpAmp

Figure 6.3: Active filter OpAmp

Signal conditioning and offset

The OpAmp circuit serves two primary functions: amplification and active filtering. Additionally, a DC offset is applied to the signal to ensure it fits within the input range of the ADC. Since the ADC operates from 0 to 5 V, the signal is centred around 2.5 V, allowing both positive and negative components of

the input waveform to be captured without clipping.

Active filter design

An active band-pass filter is implemented using a single OpAmp per channel, which helps to keep the overall cost and complexity low. The filter blocks very low frequencies (providing DC blocking) and high-frequency noise, allowing the relevant signal band to pass through. These bounds are chosen to match the signal characteristics from the Humantenna effect while minimizing interference.

The filter and gain are determined by a minimal component set: two resistors and one capacitor in the OpAmps feedback network. Using Slicap[1], the full transfer function of the circuit was determined and is shown in Equation 6.1.

$$\frac{V_{out}}{V_{in}} = \frac{C_1C_3R_1R_2s^2 + s\,(C_1R_1 + C_3R_1 + C_3R_2) + 1}{C_1C_3R_1R_2s^2 + s\,(C_1R_1 + C_3R_2) + 1} \tag{6.1}$$

A detailed analysis of this transfer function can be found in Appendix B. However, for practical design purposes, the filter can be approximated by simpler formulas. The gain is set by the resistor ratio, as shown in Equation 6.2, and the cut-off frequencies are approximated by their respective RC combinations in Equation 6.3 and Equation 6.4.

$$Gain = 1 + \frac{R_2}{R_1} = 1 + \frac{470\,K\Omega}{470\,K\Omega} = 2 \tag{6.2}$$

This gain was selected based on the amplitude of the input signal measured during the controlled setup, which was about 1 V peak-to-peak at 50 Hz. The gain was chosen to ensure the amplified signal fits well within the microcontrollers ADC input range (0–5 V), maximizing resolution while preventing clipping near the supply rails. This careful calibration preserves linearity and maximizes measurement accuracy.

The cut-off frequencies of the filter depend on the capacitor and resistor values, controlling the shape and bandwidth of the signal passed through.

$$f_h = \frac{1}{2\pi RC} = \frac{1}{2\pi \cdot 470 \cdot 10^3 \cdot 1 \cdot 10^{-9}} \approx 340 \text{ Hz} \tag{6.3}$$

$$f_l = \frac{1}{2\pi RC} = \frac{1}{2\pi \cdot 470 \cdot 10^3 \cdot 100 \cdot 10^{-6}} \approx 0.0034 \text{ Hz} \tag{6.4}$$

The high-frequency cut-off is set slightly above the expected upper signal content to ensure minimal attenuation of the desired signals while effectively reducing high-frequency noise, harmonics, and mirror signals. The low-frequency cut-off is set extremely low to provide DC blocking, eliminating offset or drift, while preserving the integrity of signals in the relevant frequency range as shown in 6.4.

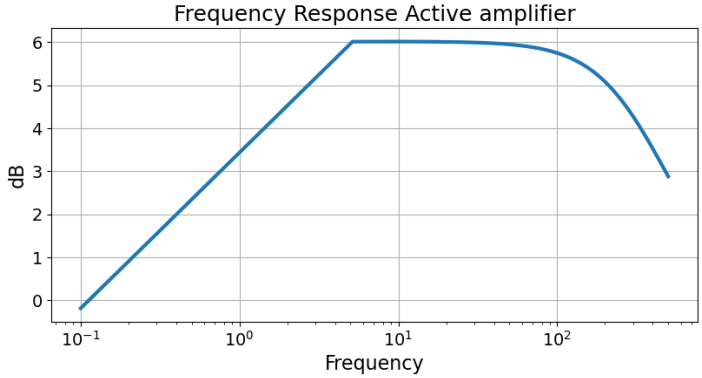

Figure 6.4: Frequency response of OpAmp

[1]Slicap is a SPICE-like circuit analysis tool integrated into LTspice.

While frequency response is important, simulations also included startup behaviour. This due to big DC blocking capacitors being used. To make sure those capacitors don't effect the performance, a startup simulation was performed. Figure 6.5 shows this simulation, and shows that the system reaches steady state after 5 seconds. This is fast enough that it does not affect the performance of the design.

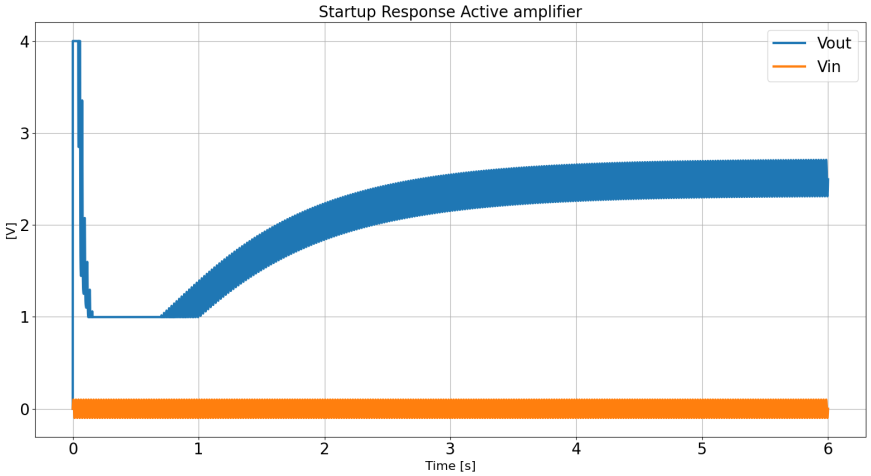

Figure 6.5: Op amp Circuit startup simulation

Performance and practical benefits

Compared to discrete transistor configurations, the OpAmp offers several critical advantages:

- Excellent linearity, ensuring faithful reproduction of the input signals amplitude
- Stable gain, unaffected by temperature or component variation
- Low input impedance, minimizing loading effects on the signal source
- Reduced risk of clipping, as the DC offset ensures the signal stays within the ADCs voltage range

Because only one OpAmp is used per channel and the supporting components are minimal, this configuration remains cost-efficient and compact while delivering high performance. In controlled testing, the amplifier provided clean, reliable signals without distortion, even with varying input amplitudes.

Conclusion

Among the three configurations evaluated, the Non-Inverting Op-Amp offers the best performance for amplitude measurement. It combines high linearity, stable gain, low offset, and minimal signal loading, while also integrating active filtering and DC offset for seamless ADC compatibility.

In comparison, the Tandem and Sziklai transistor pairs provide high gain but suffer from non-linearity and saturation. Although simple and low-cost, they require additional filtering stages and offer less consistent performance.

7

Prototype and results

Building on the amplifier configurations discussed in Chapter 6 and the sensor theory and experiments from Chapter 4, this chapter presents a working prototype for grip strength detection. The prototype brings together the key findings from the previous chapters, starting with the design of the steering wheel sensor, followed by the amplifier circuitry that enables reliable performance across a range of use cases.

7.1. Sensor prototype

During this project many different sensors configurations were built and tested. These iterations led to the development of an optimal sensor shape and configuration.

Chapter 2 highlights the need for a non-invasive and easily integrable sensor. Based on this requirement, and due to the capacitive nature of the sensor, it was decided to embed the sensor beneath the surface of the steering wheel. To achieve this, a sleeve was developed with the sensor integrated into its structure, allowing it to be easily mounted onto any standard steering wheel. This is shown in Figure 7.1b.

Chapter 4 also shows the effect of different lengths of wire on the Humantenna effect. From this experiment it was determined that longer wire and thus greater contact area are better for detection of the Humantenna effect. As such it was decided to make a snaking pattern over the outside of the steering wheel, as shown on the prototype in Figure 7.1b, where the contact area with the hand is largest.

Finally, the steering wheel was divided into six separate sensing sections (see Figure 7.1a). This design offered two key benefits:

- Reduced ambient signal pickup when not in use
- Basic hand placement detection, based on which sensors are in contact with the user's hands

During testing, participants were asked to maintain continuous contact with the sensors to ensure consistent readings and reduce the need for advanced signal processing.

7.2. Amplifier hardware

While the simulations from Chapter 6 provide valuable information, a prototype was needed to validate the design in practice. This section outlines the hardware development process across several iterations.

7.2.1. Breadboard

Initial experiments were done on a breadboard to evaluate signal characteristics and determine the required gain to achieve good signal strength. While this setup provided flexibility during early testing,

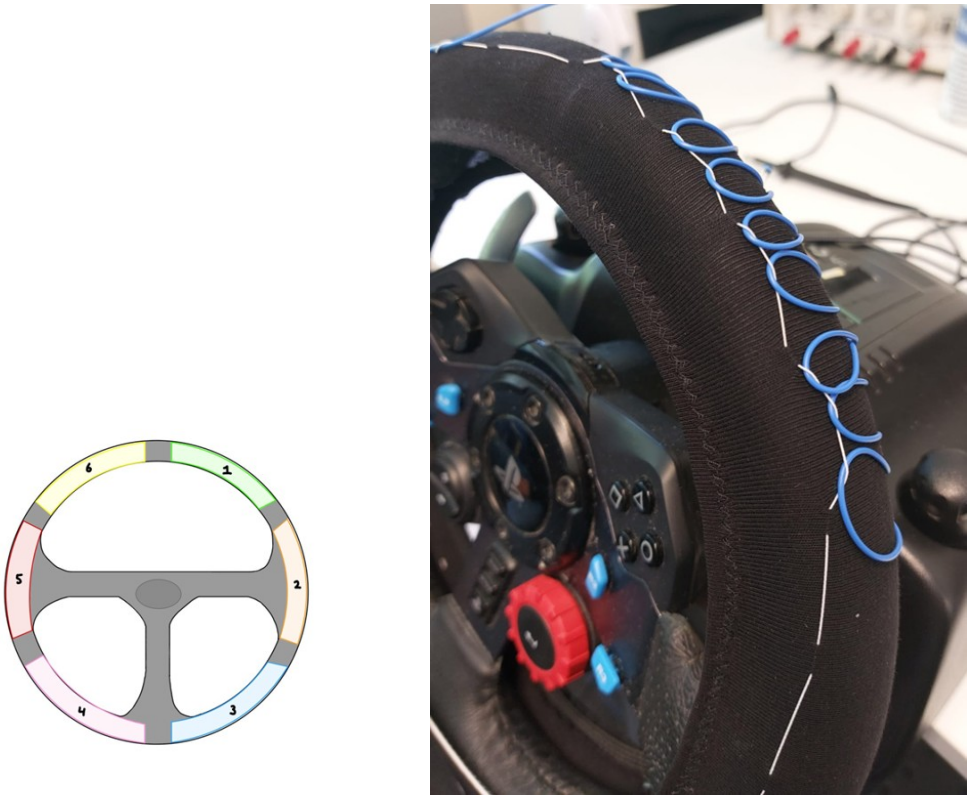

(a) Graphical view of the 6 sections (b) Picture of the 2 section prototype

Figure 7.1: Prototype

it suffered from unreliable connections, which led to inconsistent measurements.

7.2.2. Protoboard

To address the limitations of the breadboard, a more stable protoboard was developed. This version aimed to provide more consistent signal acquisition and used an external analog-to-digital converter (ADC). The internal ADC of the ESP32 had problems, including limited voltage range (0–3.3 V) and poor stability. This made it so that in many situations, the OpAmp would already start clipping at very low gain, but not be able to receive a signal in other situations due to that low gain.

The protoboard utilized the MCP3208, a discrete ADC capable of accepting input voltages up to 5 V and converting them to 12 bits, and communicating those to the ESP32 via SPI. This not only resolved the voltage limitation but also provided eight channels, enabling data acquisition from all six sensors using a single chip.

7.2.3. PCB

The final version of the prototype was realized in the form of a compact PCB using surface-mount devices (SMD). This allowed for a reduction in size while enhancing performance.

The PCB design integrates the MCP3208 ADC and two OPA4338 [1]quad op amps. The OPA4388 was chosen for its ultra low bias current, and its rail to rail output, preserving the low power signal and reducing the chance of clipping respectively. All eight channels of the ADC are utilized, with each connected to a dedicated channel of the op amps. This setup enables simultaneous sampling of all sensors, providing reliable hardware for applications such as hand placement detection, which is currently under development by the software team.

[1]section C.1

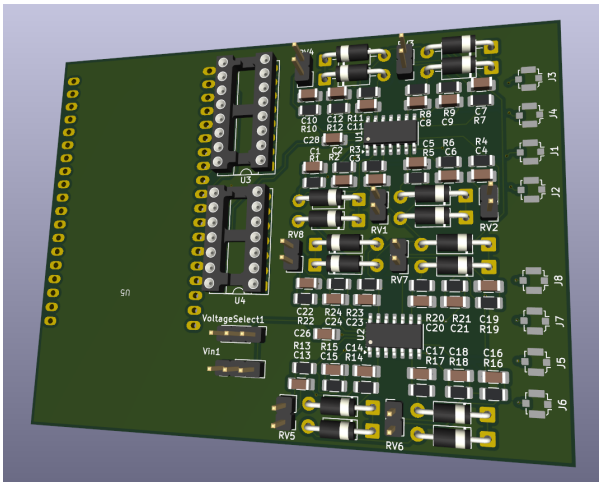

Figure 7.2: 3D render of the final PCB

7.3. results

Although the prototype meets all requirements in an indoor environment, it is not yet suitable for outdoor use. The size of the device also remains larger than ideal for the final product. These limits show a path for further miniaturization and diversification in future revisions.

It did show that measuring multiple simultanious channels of 50Hz interference is not only possible, but easy to do. This circuit together with the grip measurments from Chapter 5 allows for reliable grip estimation, which can be used for drowsiness detection.

A flaw of the current prototype is that it uses relatively expensive components, including the ESP32, OPA4338, and MCP3208 ADC. While these parts were chosen for their reliability and ease of integration during development, they may not be cost-effective for a final product. With further testing, cheaper alternatives could be identified without compromising performance.

8

Discussion

The experimental results validate the feasibility of using the Humantenna effect for detecting grip strength as an indirect indicator of driver drowsiness. The relationship between grip strength and induced voltage amplitude was consistently observed across multiple subjects, though with some variation due to individual test subjects. This variability highlights the need for further personalization or adaptive calibration algorithms to enhance detection robustness in real-world applications.

The choice of capacitive coupling over galvanic coupling allowed for better differentiation of grip strength levels, a valuable parameter in detecting drowsiness-related changes in hand behaviour. The amplifier circuit design, especially the use of a non-inverting operational amplifier, proved to be a reliable solution in terms of gain stability, linearity, and low signal distortion, outperforming simpler transistor-based configurations.

As future work, we propose implementing a voltage-controlled amplifier with an integrated control circuit to mitigate the effects of ambient electromagnetic field variations. Additionally, to improve the quantification of the relationship between grip strength and signal coupling, a more robust and precise test device is needed. Ensuring the device is consistently positioned relative to nearby power lines would reduce measurement variability, and simultaneously monitoring the ambient field during testing could enhance data accuracy.

Expanding the study to include a larger and more diverse group of test subjects would further improve statistical validity. Collecting demographic and biometric data, such as the height and weight of each participant, may help identify relevant correlations or normalisation factors.

In summary, the results are promising but indicate that further research is needed to move from a laboratory prototype to an automotive-grade product.

9

Conclusion

This project successfully demonstrated a passive, non-intrusive system for detecting driver alertness using the Humantenna effect. By leveraging the natural electromagnetic coupling between the human body and a sensor-embedded steering wheel, the system can track grip strength and hand contact with minimal hardware complexity.

A detailed analysis of coupling models, experimental signal characterization, and amplifier circuit evaluation led to the development of a robust prototype. Among various amplifier designs, the non-inverting OpAmp configuration offered the best performance for this use case, enabling real-time monitoring of grip strength.

While the system performs well in controlled environments, further research is required to improve performance in varied electromagnetic conditions and reduce component costs for commercial viability. Nonetheless, the findings lay a strong foundation for scalable integration into automotive driver monitoring systems and contribute to the growing field of passive human-machine interaction.

It is expected that the detected signal out in the field would be weak and varied in amplitude. Therefore, a variable gain amplifier that can adjust to the ambient strength of the 50 Hz electromagnetic radiation should be designed. The recommendation for future designs would be to experiment with multiplexing before the input of the amplifier, therefore only one amplifier will be needed. Further research could also look into rectifying the signal and using a peak detector circuit, greatly reducing the computational load after analogue to digital conversion.

Bibliography

[1] World Health Organization, Road traffic injuries, Accessed: 2025-05-02, 2023. [Online]. Available: https://www.who.int/news-room/fact-sheets/detail/road-traffic-injuries.

[2] SWOV - Instituut voor Wetenschappelijk Onderzoek Verkeersveiligheid, Vermoeidheid, Accessed: 2025-05-02, 2019. [Online]. Available: https://swov.nl/sites/default/files/bestanden/downloads/FS%20Vermoeidheid.pdf.

[3] M. Gonçalves, R. Amici, R. Lucas, T. Åkerstedt, F. Cirignotta, J. Horne, et al., "Sleepiness at the wheel across europe: A survey of 19 countries," Journal of Sleep Research, vol. 24, no. 3, 2015, Accessed: 2025-05-02. DOI: 10.1111/jsr.12267. [Online]. Available: https://onlinelibrary.wiley.com/doi/abs/10.1111/jsr.12267.

[4] SWOV - Instituut voor Wetenschappelijk Onderzoek Verkeersveiligheid, Road crash costs, SWOV fact sheet, The Hague. Accessed: 2025-05-02, Jun. 2024. [Online]. Available: https://swov.nl/en/fact/road-crash-costs-1-what-are-costs-road-crashes.

[5] J. F. Pagel, "Excessive daytime sleepiness," American Family Physician, vol. 79, no. 5, 2009, Accessed: 2025-05-02. [Online]. Available: https://www.aafp.org/pubs/afp/issues/2009/0301/p391.pdf.

[6] National Center for Biotechnology Information (NCBI), Medgen: Narcolepsy [internet], Accessed: 2025-05-02, 2025. [Online]. Available: https://www.ncbi.nlm.nih.gov/medgen/4390.

[7] H. Pan, D. B. Logan, et al., "Exploring the effect of driver drowsiness on takeover performance during automated driving: An updated literature review," Accident Analysis & Prevention, 2024, Accessed: 2025-05-02. DOI: 10.1016/j.aap.2024.107345. [Online]. Available: https://www.sciencedirect.com/science/article/pii/S0001457525001095.

[8] E. Perkins et al., "Challenges of driver drowsiness prediction: The remaining steps to implementation," IEEE Transactions on Intelligent Transportation Systems, vol. 22, no. 7, pp. 4235–4245, 2021. DOI: 10.1109/TITS.2020.3014567.

[9] Volvo Cars, Volvo s60 support driver alert control, Accessed: 2025-04-29, 2024. [Online]. Available: https://www.volvocars.com/mt/support/car/s60/article/f57bafffba0c0468c0a8015174f226

[10] Mercedes-Benz, Technology milestones, Accessed: 2025-04-29, 2024. [Online]. Available: https://www.mercedes-benz.com/en/innovation/milestones/technology/.

[11] Tesla, Model 3 owners manual, Accessed: 2025-04-29, 2024. [Online]. Available: https://www.tesla.com/ownersmanual/model3/en_eu/GUID-65BF21B8-50C5-4FA5-86A4-DA363DCD0484.html.

[12] Mercedes-Benz USA, Attention assist with microsleep detection eqs sedan manual, Accessed: 2025-04-29, 2022. [Online]. Available: https://www.mbusa.com/en/owners/manuals/eqs-sedan-2022-03-v297-mbux/attention-assist/function-of-attention-assist-with-microsleep-detection.

[13] Siddharth and M. M. Trivedi, "On assessing driver awareness of situational criticalities: Multimodal bio-sensing and vision-based analysis, evaluations, and insights," Brain Sciences, vol. 10, no. 1, p. 15, 2020. DOI: 10.3390/brainsci10010015.

[14] G. S. Maximous and H. A. Bastawrous, "Driver drowsiness detection based on humantenna effect for automotive safety systems," in 2020 IEEE 9th Global Conference on Consumer Electronics (GCCE), IEEE, 2020, pp. 1–2. DOI: 10.1109/GCCE50665.2020.9291815.

[15] G. Cohn et al., "Your noise is my command: Sensing gestures using the body as an antenna," in Proceedings of the SIGCHI Conference on Human Factors in Computing Systems, ACM, 2011, pp. 791–800. DOI: 10.1145/1978942.1979058.

[16] G. Cohn, D. Morris, S. Patel, and D. Tan, "Humantenna: Using the body as an antenna for real-time whole-body interaction," in Proceedings of the SIGCHI Conference on Human Factors in Computing Systems, ser. CHI '12, Austin, Texas, USA: ACM, 2012, pp. 1901–1910, ISBN: 978-1-4503-1015-4. DOI: 10.1145/2207676.2208330. [Online]. Available: %7Bhttp://doi.acm.org/10.1145/2207676.2208330%7D.

[17] J. Souman. "Safe co-drivership with avs requires advanced human-vehicle interaction and driver monitoring systems." Accessed: 2025-05-01, TNO. (Oct. 2024), [Online]. Available: https://www.tno.nl/en/newsroom/insights/2024/10/safe-co-drivership-avs/.

[18] H. Elfekey and S. O. Hany Bastawrous, "A touch sensing technique using the effects of extremely low frequency fields on the human body," Sensors, vol. 16, no. 12, p. 2049, 2016. DOI: 10.3390/s16122049.

[19] C. Peratta and A. Peratta, Modelling the Human Body Exposure to ELF Electric Fields (Topics in Engineering 47). Billerica, UK: WIT Press, 2010, ISBN: 978-1-84564-418-5.

[20] A. Slceanu, O. Neacsu, V. David, and E. Lunc, "Measurements upon human body capacitance: Theory and experimental setup," in IMEKO International Conference TC4 Symposium on Measurement of Electromechanical Quantities, Typical human body capacitance measured around 100pF, 2007.

[21] C. Aliau-Bonet and R. Pallas-Areny, "A novel method to estimate body capacitance to ground at mid frequencies," IEEE Transactions on Instrumentation and Measurement, vol. 62, no. 9, pp. 2392–2399, Sep. 2013. DOI: 10.1109/TIM.2013.2257747.

[22] Opax388 precision, zero-drift, zero-crossover, true rail-to-rail, input/output operational amplifiers, OPA388, Texas Instruments, Jul. 2020.

Appendices

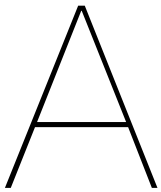

Code

A.1. Linear Regression Code

```
import matplotlib.pyplot as plt

#Input calibration values
Force = [0.128, 0.256, 0.259, 0.518, 0.750, 1]
R = [20 * 10**3, 10 * 10**3, 9.1*10**3, 5 * 10**3, 2.7 * 10**3, 2.1 * 10**3]

#Check the graph
plt.loglog(Force, R)
plt.show()

#Convert Resistance to Vout
Vout = []
for i in R:
    Vout.append(3.2 * ((2.2*10**3)/((2.2*10**3) + (i))))

plt.loglog(Force,Vout)
plt.show()

#Use Scipy for linear Regression
from scipy import stats

y = Force
x = Vout


slope, intercept, r, p, std_err = stats.linregress(x, y)

print(f"Force = {slope} * Vout + {intercept}")

def myfunc(x):
  return slope * x + intercept

mymodel = list(map(myfunc, x))

plt.scatter(x, y)
plt.plot(x, mymodel)
```

```
plt.show()

# Output: Force = 0.6420370502794951 * Vout + -0.11073969207645945
```

A.2. Grip Graphmaker

```
import numpy as np
import pandas as pd
import matplotlib.pyplot as plt
from scipy.signal import find_peaks
import os

def plotcsv(filename):

    # --- Load CSV using full file path ---
    df = pd.read_csv(filename)  # Update this path

    # Extract columns
    time = df['timestamp'].values
    sine_signal = df['osc_ch2'].values  * 10
    voltage_signal = df['osc_ch1'].values  * 10

    # Step 1: Detect peaks in sine signal
    # Since frequency is 50 Hz and sample rate 1000 Hz,
    # minimum distance between peaks ~ 1000/50 = 20 samples
    peaks, _ = find_peaks(sine_signal, distance=20)

    peak_times = time[peaks]
    peak_amplitudes = sine_signal[peaks]

    # Step 2: Convert voltage to force using your formula
    # force_signal = 4.201e6 * voltage_signal ** -1.1
    force_signal = voltage_signal

    # Step 3: Get force values at the peak points
    force_at_peaks = force_signal[peaks]

    # --- Moving average smoothing function ---
    def moving_average(x, w):
        return np.convolve(x, np.ones(w), 'valid') / w

    # Sort data by force so smoothing makes sense
    sorted_indices = np.argsort(force_at_peaks)
    force_sorted = force_at_peaks[sorted_indices]
    amps_sorted = peak_amplitudes[sorted_indices]

    # Smooth the amplitudes with window size w (try w=10)
    w = 10
    amps_smooth = moving_average(amps_sorted, w)
    force_smooth = force_sorted[w//2: -w//2 + 1]  # align x with smooth y

    force_smooth = ( 0.64204* (force_smooth) - 0.111 ) * 9.81

    #indices = []
    #for i in range(len(force_smooth)):
```

```
    #     if 0 < force_smooth[i] < 10:
    #         pass
    #     else:
    #         indices.append(i)
    #
    #force_smooth = np.delete(force_smooth,indices)
    #amps_smooth = np.delete(amps_smooth,indices)

    # Step 4: Plot

    #plt.plot(force_at_peaks, peak_amplitudes, 'o', alpha=0.3, label='Raw Peaks')
    plt.plot(force_smooth, amps_smooth, '-', linewidth=2, label=filename)



if __name__ == "__main__":

    plt.figure(figsize=(10, 6))
    plt.xlabel('Force (N)')
    plt.ylabel('Amplitude of Sine Peaks')
    plt.title('Force vs Amplitude of Sine Peaks (Smoothed)')
    plt.grid(True)
    plt.tight_layout()

    dir  = "GripSensorTests"
    for i in os.listdir(dir):
        plotcsv(f"{dir}/{i}")

    plt.legend()

    plt.show()
```

A.3. GripMeasurment code

```
import threading
import time
import csv
import signal
import numpy as np
import dwfpy as dwf
import datetime
import serial

''''
IMPORTANT NOTE -
YOU NEED TO INSTALL DIGILENT WAVEFORMS AS WELL AS THE DWFPY AND PYSERIAL PACKAGE
'''

# === Parameters ===
Record_time = 15
SAMPLE_RATE = 1000  # Hz
BUFFER_SIZE = 10000    # Samples
READ_INTERVAL = 1*(BUFFER_SIZE/SAMPLE_RATE)  # Seconds (50 ms)
CSV_FILE = "GripSensorTests/recM2.csv"
```

```
# === Thread control flag ===
running = True

# === Shared queue to pass data from thread to logger ===
osc_queue = []
esp_queue = []

# === Oscilloscope Thread Function ===
def record_oscilloscope():
    with dwf.Device() as device:
        print(f"Connected to: {device.name} ({device.serial_number})")
        scope = device.analog_input

        for ch in [0, 1]:
            scope[ch].setup(range=5)
            scope[1].setup(range=2)

        scope.sample_rate = SAMPLE_RATE
        scope.buffer_size = BUFFER_SIZE
        scope.scan_shift(sample_rate=SAMPLE_RATE,
                         buffer_size=BUFFER_SIZE,
                         configure=True,
                         start=True)

        # Initialize time tracking
        dt = 1 / SAMPLE_RATE
        sample_index = 0
        start_time = time.perf_counter()

        while running:
            time.sleep(READ_INTERVAL)
            scope.read_status(read_data=True)
            ch1 = np.array(scope[0].get_data())
            ch2 = np.array(scope[1].get_data())

            # Compute timestamps from sample index
            ts_start = start_time + sample_index * dt
            osc_queue.append((ts_start, ch1.tolist(), ch2.tolist()))

            sample_index += len(ch1)


def record_esp32_serial(port="COM6", baud=921600):
    try:
        ser = serial.Serial(port, baud, timeout=0.5)
        print(f"Connected to ESP32 on {port} @ {baud} baud.")
    except serial.SerialException as e:
        print(f"[ERROR] Could not open serial port: {e}")
        return

    try:
        while running:
            try:
                line = ser.readline().decode(errors='ignore').strip()
                if line:
                    try:
```

```
                        parts = [int(x.strip()) for x in line.split(',')]
                        if len(parts) == 2:
                            esp_time = parts[0] / 1_000_000  # µs to sec
                            val = parts[1]
                            host_time = time.perf_counter()
                            esp_queue.append((host_time, [esp_time, val]))
                        else:
                            print(f"[ESP PARSE WARNING] Invalid line: {line}")
                    except Exception as e:
                        print(f"[ESP PARSE ERROR] Line: {line} {e}")
            except Exception as read_err:
                print(f"[ESP32 Read Error] {read_err}")
                break
    finally:
        ser.close()
        print("ESP32 serial closed.")


# === Signal handler for Ctrl+C ===
# Define stop_all so it works for both signal and timer
def stop_all(sig=None, frame=None):
    global running
    print("Stopping recording...")
    running = False

# Register Ctrl+C handler
signal.signal(signal.SIGINT, stop_all)

# Start auto-stop timer
stop_timer = threading.Timer(Record_time, stop_all)
stop_timer.start()

signal.signal(signal.SIGINT, stop_all)

# === Data Saver (Main Thread) ===
def gather_and_save():
    all_rows = []
    osc_sample_rate = SAMPLE_RATE  # same as used in record_oscilloscope

    print("Logging to CSV... Press Ctrl+C to stop.")

    empty_loops = 0
    max_empty_loops = 40  # ~2 seconds idle

    while True:
        wrote_data = False

        # === Handle oscilloscope batches ===
        while osc_queue:
            ts, ch1, ch2 = osc_queue.pop(0)
            dt = 1 / SAMPLE_RATE
            for i in range(len(ch1)):
                t_sample = ts + i * dt
                all_rows.append([t_sample, ch1[i], ch2[i], None, None])
            wrote_data = True
```

```
        # === Handle ESP32 real-time samples ===
        while esp_queue:
            host_ts, val = esp_queue.pop(0)
            esp_time, sensor_val = val
            # You can choose to use `host_ts` or `esp_time`
            all_rows.append([host_ts, None, None, esp_time, sensor_val])

            wrote_data = True

        if not wrote_data:
            empty_loops += 1
            if not running and empty_loops > max_empty_loops:
                print("Queues idle and stopped. Exiting logger.")
                break
        else:
            empty_loops = 0

        time.sleep(0.005)

    # === Sort by timestamp ===
    all_rows.sort(key=lambda row: row[0])

    # === Write to CSV ===
    with open(CSV_FILE, "w", newline='') as f:
        writer = csv.writer(f)
        writer.writerow(["timestamp",
                         "osc_ch1",
                         "osc_ch2",
                         "esp_timestamp",
                         "esp_value"])
        writer.writerows(all_rows)

    print("Recording complete.")

osc_thread = threading.Thread(target=record_oscilloscope)
esp_thread = threading.Thread(target=record_esp32_serial)

# make them daemon threads so they wont hang the process if something goes wrong
osc_thread.daemon = True
esp_thread.daemon = True

osc_thread.start()
esp_thread.start()

# wait for the autostop timer to fire, which calls stop_all()
stop_timer.join()                   # blocks until Record_time elapses

# now both threads will naturally exit their loops (running==False)
print("Waiting for acquisition threads to finish")
osc_thread.join(timeout=1.0)        # give them up to 1s to wrap up
esp_thread.join(timeout=1.0)

# now safely gather whatevers left in the queues and write the CSV
gather_and_save()
```

```
print("All threads joined. Program ended.")

print("All threads joined. Program ended.")
```

A.4. Slicap Op Amp Analysis

```
import SLiCAP as sl
import sympy as sp

sl.initProject('InitialAmplifier', notebook=True)
cir = sl.makeCircuit("InitialAmplifier.kicad_sch")

sl.img2html("InitialAmplifier.svg", width=300)

MNA = sl.doMatrix(cir)
sl.matrices2html(MNA)

gain = sl.doLaplace(cir,
                    transfer = "gain",
                    source="V1",
                    detector="V_Vout",
                    lgref = 'circuit')
sl.eqn2html('V_out/V_in', gain.laplace)

poles = sl.doPoles(cir,
                    transfer = "gain",
                    source="V1",
                    detector="V_Vout",
                    lgref = 'circuit')
sl.eqn2html('p',poles.poles)

zeros = sl.doZeros(cir,
                    transfer = "gain",
                    source="V1",
                    detector="V_Vout")
sl.eqn2html("Z", zeros.zeros)

numGain = sl.doLaplace(cir,
                        pardefs="circuit",
                        numeric=True,
                        source="V1",
                        detector="V_Vout")

sp.simplify(gain.laplace)
sl.eqn2html('V_out/V_in', gain.laplace)

#Only works if R1 and R2 arent symbolic
figMag = sl.plotSweep('RCmag',
                        'Magnitude characteristic',
                        numGain,
                        1,
                        '10k',
                        100,
                        yUnits = '-',
                        show = True)
```

B

Analysis of Active Band-Pass Amplifier

The following chapter derives the formulas for the op amp circuit based on the Slicap analysis of the circuit in Figure B.1

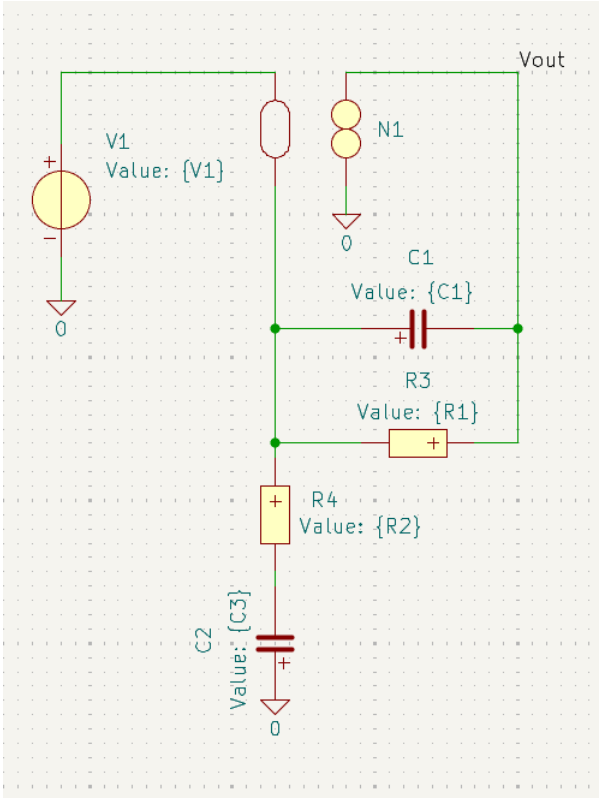

Figure B.1: Slicap Simulation circuit

Transfer Function and General Characteristics

The general form of the transfer function for the active band-pass amplifier under analysis is given by:

$$\frac{V_{\text{out}}}{V_{\text{in}}} = \frac{C_1 C_3 R_1 R_2 s^2 + s\left(C_1 R_1 + C_3 R_1 + C_3 R_2\right) + 1}{C_1 C_3 R_1 R_2 s^2 + s\left(C_1 R_1 + C_3 R_2\right) + 1} \tag{B.1}$$

This is a second-order band-pass filter, which can be analyzed in the standard second-order form:

$$H(s) = \frac{a_2 s^2 + a_1 s + 1}{b_2 s^2 + b_1 s + 1} \tag{B.2}$$

where:

$$\begin{aligned} a_2 &= C_1 C_3 R_1 R_2 \\ a_1 &= C_1 R_1 + C_3 R_1 + C_3 R_2 \\ b_2 &= C_1 C_3 R_1 R_2 \\ b_1 &= C_1 R_1 + C_3 R_2 \end{aligned}$$

Derivation of Natural Frequency

The natural frequency ω_0 is derived by comparing the denominator to the standard second-order system:

$$H(s) = \frac{\cdots}{\frac{1}{\omega_0^2} s^2 + \frac{1}{Q\omega_0} s + 1}$$

From this form, the coefficient of s^2 in the denominator gives:

$$\frac{1}{\omega_0^2} = C_1 C_3 R_1 R_2 \quad \Rightarrow \quad \omega_0 = \frac{1}{\sqrt{C_1 C_3 R_1 R_2}} \tag{B.3}$$

Derivation of Quality Factor

To find the quality factor Q, we use the coefficient of the s term in the denominator:

$$\frac{1}{Q\omega_0} = C_1 R_1 + C_3 R_2$$

Rewriting in terms of Q:

$$Q = \frac{1}{\omega_0 (C_1 R_1 + C_3 R_2)}$$

Substituting the expression for ω_0 from Equation B.3:

$$\begin{aligned} Q &= \frac{1}{\left(\frac{1}{\sqrt{C_1 C_3 R_1 R_2}}\right)(C_1 R_1 + C_3 R_2)} \\ &= \frac{\sqrt{C_1 C_3 R_1 R_2}}{C_1 R_1 + C_3 R_2} \end{aligned} \tag{B.4}$$

Cutoff Frequencies

The 3-dB cutoff frequencies ω_L and ω_H correspond to the frequencies at which the gain drops to $\frac{1}{\sqrt{2}}$ of the maximum. Start from the denominator of the standard second-order transfer function:

$$|H(j\omega)| = \frac{\omega/\omega_0}{\sqrt{\left(1 - (\omega/\omega_0)^2\right)^2 + \left(\frac{\omega}{Q\omega_0}\right)^2}}$$

At the cutoff frequencies, $|H(j\omega)| = \frac{1}{\sqrt{2}} \times |H(j\omega_0)|$. Solving this yields:

$$\frac{\omega_{H,L}}{\omega_0} = \sqrt{1 + \frac{1}{4Q^2}} \pm \frac{1}{2Q}$$

$$\Rightarrow \quad \omega_{H,L} = \omega_0 \left(\sqrt{1 + \frac{1}{4Q^2}} \pm \frac{1}{2Q} \right) \tag{B.5}$$

Center Frequency Gain

The gain at the center frequency ω_0 is determined by evaluating the magnitude of the transfer function at $\omega = \omega_0$. Simplifying the result gives:

$$A_{\text{center}} = \left| \frac{V_{\text{out}}}{V_{\text{in}}} \right|_{\omega=\omega_0} = 1 + \frac{C_3 R_1}{C_1 R_1 + C_3 R_2} \tag{B.6}$$

Putting in the numbers

Given component values:

$$R_1 = R_2 = 470\,\text{k}\Omega = 470 \times 10^3\,\Omega$$
$$C_1 = 1\,\text{nF} = 1 \times 10^{-9}\,\text{F}$$
$$C_3 = 100\,\mu\text{F} = 100 \times 10^{-6}\,\text{F}$$

Center Frequency

$$\omega_0 = \frac{1}{\sqrt{(1 \times 10^{-9})(100 \times 10^{-6})(470 \times 10^3)^2}} \approx 6.72\,\text{rad/s}$$

$$f_0 = \frac{\omega_0}{2\pi} \approx 1.07\,\text{Hz}$$

Quality Factor

$$Q = \frac{\sqrt{(1 \times 10^{-9})(100 \times 10^{-6})(470 \times 10^3)^2}}{(1 \times 10^{-9})(470 \times 10^3) + (100 \times 10^{-6})(470 \times 10^3)} \approx 0.00316$$

Cutoff Frequencies

$$\omega_H \approx 6.72 \times \left(\sqrt{1 + \frac{1}{4Q^2}} + \frac{1}{2Q} \right) \approx 2127.5\,\text{rad/s} \quad \Rightarrow \quad f_H \approx 339\,\text{Hz}$$

$$\omega_L \approx 6.72 \times \left(\sqrt{1 + \frac{1}{4Q^2}} - \frac{1}{2Q} \right) \approx 0.269\,\text{rad/s} \quad \Rightarrow \quad f_L \approx 0.043\,\text{Hz}$$

Center Frequency Gain

$$A_{\text{center}} = 1 + \frac{47}{0.00047 + 47} \approx 2.0$$

Summary

- Center frequency: $f_0 \approx 1.07\,\text{Hz}$
- Low cutoff frequency: $f_L \approx 0.043\,\text{Hz}$
- High cutoff frequency: $f_H \approx 339\,\text{Hz}$
- Gain at center frequency: $A_{\text{center}} \approx 2.0$

C

Datasheets

C.1. OPAx388[22]

TEXAS INSTRUMENTS
OPA388, OPA2388, OPA4388
SBOS777D – NOVEMBER 2016 – REVISED JULY 2020

OPAx388 Precision, Zero-Drift, Zero-Crossover, True Rail-to-Rail, Input/Output Operational Amplifiers

1 Features

- Ultra-low offset voltage: ±0.25 µV
- Zero drift: ±0.005 µV/°C
- Zero crossover: 140-dB CMRR true RRIO
- Low noise: 7.0 nV/√Hz at 1 kHz
- No 1/f noise: 140 nV_{PP} (0.1 Hz to 10 Hz)
- Fast settling: 2 µs (1 V to 0.01%)
- Gain bandwidth: 10 MHz
- Single supply: 2.5 V to 5.5 V
- Dual supply: ±1.25 V to ±2.75 V
- True rail-to-rail input and output
- EMI/RFI filtered inputs
- Industry-standard packages:
  - Single in SOIC-8, SOT-23-5, and VSSOP-8
  - Dual in SOIC-8 and VSSOP-8
  - Quad in SOIC-14 and TSSOP-14

2 Applications

- Merchant network and server PSU
- Notebook PC power adapter design
- Weigh scale
- Lab and field instrumentation
- Battery test
- Electronic thermometer
- Temperature transmitter

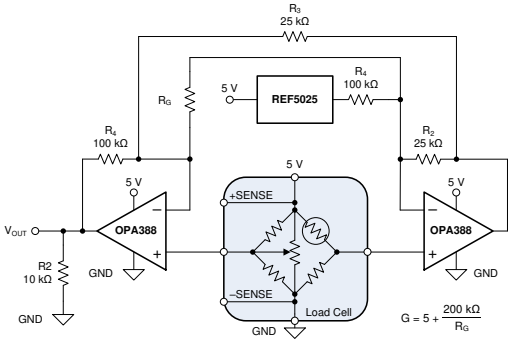

The OPA388 in a High-CMRR, Instrumentation Amplifier Application

3 Description

The OPAx388 (OPA388, OPA2388, and OPA4388) series of precision operational amplifiers are ultra-low noise, fast-settling, zero-drift, zero-crossover devices that provide rail-to-rail input and output operation. These features and excellent ac performance, combined with only 0.25 µV of offset and 0.005 µV/°C of drift over temperature, makes the OPAx388 a great choice for driving high-precision, analog-to-digital converters (ADCs) or buffering the output of high-resolution, digital-to-analog converters (DACs). This design results in excellent performance when driving analog-to-digital converters (ADCs) without degradation of linearity. The OPA388 (single version) is available in the VSSOP-8, SOT23-5, and SOIC-8 packages. The OPA2388 (dual version) is offered in the VSSOP-8 and SO-8 packages. The OPA4388 (quad version) is offered in the TSSOP-14 and SO-14 packages. All versions are specified over the industrial temperature range of –40°C to +125°C.

Device Information

PART NUMBER	PACKAGE(1)	BODY SIZE (NOM)
OPA388	SOIC (8)	4.90 mm × 3.90 mm
	SOT-23 (5)	2.90 mm × 1.60 mm
	VSSOP (8)	3.00 mm × 3.00 mm
OPA2388	SOIC (8)	4.90 mm × 3.90 mm
	VSSOP (8)	3.00 mm × 3.00 mm
OPA4388	SOIC (14)	8.65 mm x 3.90 mm
	TSSOP (14)	5.00 mm x 4.40 mm

(1) For all available packages, see the package option addendum at the end of the data sheet.

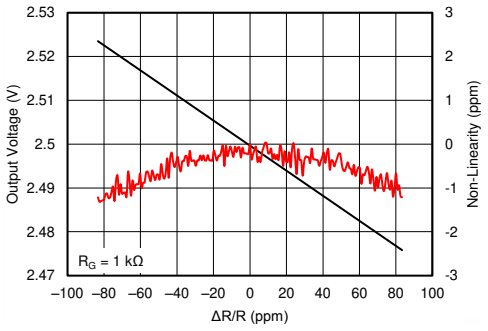

The OPA388 Allows Precision, Low-Error Measurements

Table of Contents

4 Revision History

NOTE: Page numbers for previous revisions may differ from page numbers in the current version.

Changes from Revision C (May 2019) to Revision D (July 2020)	Page
• Changed OPA2388 SOIC-8 (D) package from advanced information (preview) to production data (active)	1
• Changed typical application schematic to show correct locations for reference designators	1
• Changed Figure 8-5 to show correct locations for reference designators	25

Changes from Revision B (January 2019) to Revision C (May 2019)	Page
• Changed OPA4388 from advanced information (preview) to production data (active)	1
• Added VOS specifications for OPA4388	7
• Added dVOS/dT specifications for OPA4388	7
• Added PSRR specifications for OPA4388	7
• Added IB specifications for OPA4388	7
• Added IOS specifications for OPA4388	7
• Added CMRR specifications for OPA4388	7
• Added AOL specifications for OPA4388	7

Changes from Revision A (July 2018) to Revision B (January 2019)	Page
• Changed OPA388 DBV (SOT-23) package from preview to production data	1
• Deleted redundant temperature specification in EC table	7
• Added Figure 6, *Offset Voltage vs Supply Voltage: OPA4388*	10
• Added Figure 7, *Offset Voltage Long Term Drift*	10
• Changed Figure 50, *OPA388 Layout Example*; updated for accuracy	26

Changes from Revision * (December 2016) to Revision A (July 2018) **Page**

- Changed device status from Production Data to Production Data/Mixed Status....1
- Added top navigator link for TI reference design....1
- Added preview notes to 5-pin SOT-23 (OPA388), 8-pin SOIC (OPA2388), 14-pin SOIC, and 14-pin TSSOP (OPA4388) packages in *Device Information* table....1
- Added package preview notes to *Pin Configuration and Functions* section....4
- AOL test condition changed to 0.15 V from 0.1 V....7
- AOL test condition changed to 0.15 V from 0.1 V....7
- AOL test condition changed to 0.25 V from 0.2 V....7
- AOL test condition changed to 0.3 V from 0.25 V....7

5 Pin Configuration and Functions

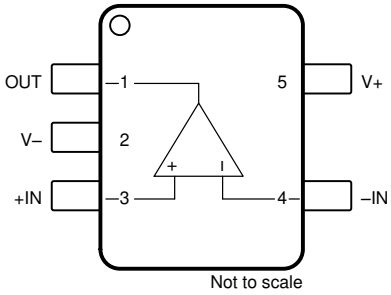

Figure 5-1. OPA388 DBV Package, 5-Pin SOT-23, Top View

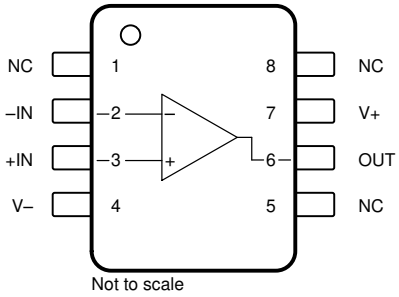

Figure 5-2. OPA388 D and DGK Packages, 8-Pin SOIC and VSSOP, Top View

Pin Functions: OPA388

PIN			I/O	DESCRIPTION
NAME	OPA388			
	D (SOIC), DGK (VSSOP)	DBV (SOT-23)		
–IN	2	4	I	Inverting input
+IN	3	3	I	Noninverting input
NC	1, 5, 8	—	—	No internal connection (can be left floating)
OUT	6	1	O	Output
V–	4	2	—	Negative (lowest) power supply
V+	7	5	—	Positive (highest) power supply

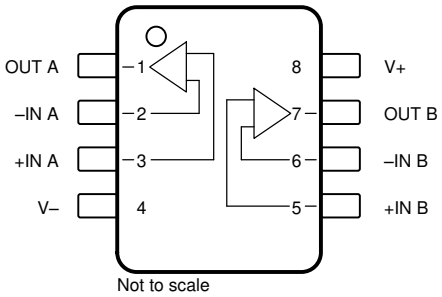

Figure 5-3. OPA2388 8-Pin SOIC (D) Package and 8-Pin VSSOP (DGK) Package, Top View

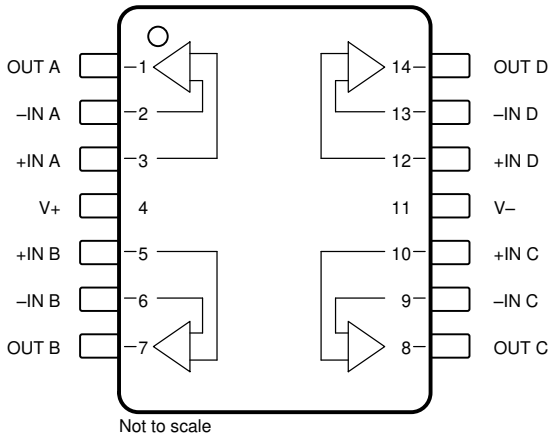

Figure 5-4. OPA4388 14-Pin SOIC (D) and TSSOP-14 (PW) Packages, Top View

Pin Functions: OPA2388 and OPA4388

PIN			I/O	DESCRIPTION
NAME	OPA2388 D (SOIC), DGK (VSSOP)	OPA4388 D (SOIC), PW (TSSOP)		
–IN A	2	2	I	Inverting input, channel A
–IN B	6	6	I	Inverting input, channel B
–IN C	—	9	I	Inverting input, channel C
–IN D	—	13	I	Inverting input, channel D
+IN A	3	3	I	Noninverting input, channel A
+IN B	5	5	I	Noninverting input, channel B
+IN C	—	10	I	Noninverting input, channel C
+IN D	—	12	I	Noninverting input, channel D
OUT A	1	1	O	Output, channel A
OUT B	7	7	O	Output, channel B
OUT C	—	8	O	Output, channel C
OUT D	—	14	O	Output, channel D
V–	4	11	—	Negative (lowest) power supply
V+	8	4	—	Positive (highest) power supply

6 Specifications

6.1 Absolute Maximum Ratings

over operating free-air temperature range (unless otherwise noted)(1)

			MIN	MAX	UNIT
Supply voltage	V_S = (V+) – (V–)	Single-supply		6	V
		Dual-supply		±3	
Signal input pins	Voltage	Common-mode	(V–) – 0.5	(V+) + 0.5	V
		Differential		(V+) – (V–) + 0.2	
	Current			±10	mA
Output short circuit(2)			Continuous	Continuous	
Temperature	Operating, T_A		–55	150	°C
	Junction, T_J			150	
	Storage, T_{stg}		–65	150	

(1) Stresses beyond those listed under *Absolute Maximum Ratings* may cause permanent damage to the device. These are stress ratings only, which do not imply functional operation of the device at these or any other conditions beyond those indicated under *Recommended Operating Conditions*. Exposure to absolute-maximum-rated conditions for extended periods may affect device reliability.
(2) Short-circuit to ground, one amplifier per package.

6.2 ESD Ratings

			VALUE	UNIT
$V_{(ESD)}$	Electrostatic discharge	Human-body model (HBM), per ANSI/ESDA/JEDEC JS-001(1)	±4000	V
		Charged-device model (CDM), per JEDEC specification JESD22-C101(2)	±1000	

(1) JEDEC document JEP155 states that 500-V HBM allows safe manufacturing with a standard ESD control process.
(2) JEDEC document JEP157 states that 250-V CDM allows safe manufacturing with a standard ESD control process.

6.3 Recommended Operating Conditions

over operating free-air temperature range (unless otherwise noted)

		MIN	NOM	MAX	UNIT
Supply voltage, V_S = (V+) – (V–)	Single-supply	2.5		5.5	V
	Dual-supply	±1.25		±2.75	
Specified temperature		–40		125	°C

6.4 Thermal Information: OPA388

THERMAL METRIC(1)		OPA388			UNIT
		D (SOIC)	DBV (SOT-23)	DGK (VSSOP)	
		8 PINS	5 PINS	5 PINS	
$R_{\theta JA}$	Junction-to-ambient thermal resistance	116	145.7	177	°C/W
$R_{\theta JC(top)}$	Junction-to-case (top) thermal resistance	60	94.8	69	°C/W
$R_{\theta JB}$	Junction-to-board thermal resistance	56	43.4	100	°C/W
Ψ_{JT}	Junction-to-top characterization parameter	12.8	24.7	9.9	°C/W
Ψ_{JB}	Junction-to-board characterization parameter	55.9	43.1	98.3	°C/W
$R_{\theta JC(bot)}$	Junction-to-case (bottom) thermal resistance	N/A	N/A	n/a	°C/W

(1) For more information about traditional and new thermal metrics, see the *Semiconductor and IC Package Thermal Metrics* application report.

6.5 Thermal Information: OPA2388

THERMAL METRIC[1]		OPA2388		UNIT
		D (SOIC)	DGK (VSSOP)	
		8 PINS	8 PINS	
$R_{\theta JA}$	Junction-to-ambient thermal resistance	120.0	165	°C/W
$R_{\theta JC(top)}$	Junction-to-case (top) thermal resistance	52.3	53	°C/W
$R_{\theta JB}$	Junction-to-board thermal resistance	65.6	87	°C/W
Ψ_{JT}	Junction-to-top characterization parameter	9.6	4.9	°C/W
Ψ_{JB}	Junction-to-board characterization parameter	64.4	85	°C/W
$R_{\theta JC(bot)}$	Junction-to-case (bottom) thermal resistance	N/A	N/A	°C/W

(1) For more information about traditional and new thermal metrics, see the *Semiconductor and IC Package Thermal Metrics* application report.

6.6 Thermal Information: OPA4388

THERMAL METRIC[1]		OPA4388		UNIT
		D (SOIC)	PW (TSSOP)	
		14 PINS	14 PINS	
$R_{\theta JA}$	Junction-to-ambient thermal resistance	86.4	109.6	°C/W
$R_{\theta JC(top)}$	Junction-to-case (top) thermal resistance	46.3	27.4	°C/W
$R_{\theta JB}$	Junction-to-board thermal resistance	41.0	56.1	°C/W
Ψ_{JT}	Junction-to-top characterization parameter	11.3	1.5	°C/W
Ψ_{JB}	Junction-to-board characterization parameter	40.7	54.9	°C/W
$R_{\theta JC(bot)}$	Junction-to-case (bottom) thermal resistance	N/A	N/A	°C/W

(1) For more information about traditional and new thermal metrics, see the *Semiconductor and IC Package Thermal Metrics* application report.

6.7 Electrical Characteristics: VS = ±1.25 V to ±2.75 V (VS = 2.5 to 5.5 V)

at T_A = 25°C, V_{CM} = V_{OUT} = V_S / 2, and R_{LOAD} = 10 kΩ connected to V_S / 2 (unless otherwise noted)

PARAMETER		TEST CONDITIONS		MIN	TYP	MAX	UNIT
OFFSET VOLTAGE							
V_{OS}	Input offset voltage		OPA388, OPA2388		±0.25	±5	µV
		V_S = 5.5 V	OPA4388		±2.25	±8	
		T_A = –40°C to +125°C	OPA388, OPA2388			±7.5	
		T_A = –40°C to +125°C, V_S = 5.5 V	OPA4388			±10.5	
dV_{OS}/dT	Input offset voltage drift	T_A = –40°C to +125°C	OPA388, OPA2388		±0.005	±0.05	µV/°C
		T_A = –40°C to +125°C, V_S = 5.5 V	OPA4388		±0.005	±0.05	
PSRR	Power-supply rejection ratio	T_A = –40°C to +125°C	OPA388, OPA2388		±0.1	±1	µV/V
			OPA4388		±1.25	±3.5	

6.7 Electrical Characteristics: VS = ±1.25 V to ±2.75 V (VS = 2.5 to 5.5 V) (continued)

at T_A = 25°C, V_{CM} = V_{OUT} = V_S / 2, and R_{LOAD} = 10 kΩ connected to V_S / 2 (unless otherwise noted)

PARAMETER		TEST CONDITIONS		MIN	TYP	MAX	UNIT
INPUT BIAS CURRENT							
I_B	Input bias current	R_{IN} = 100 kΩ, OPA388, OPA2388			±30	±350	pA
			T_A = 0°C to +85°C			±400	
			T_A = –40°C to +125°C			±700	
		R_{IN} = 100 kΩ, OPA4388			±30	±500	
			T_A = 0°C to +85°C			±600	
			T_A = –40°C to +125°C			±800	
I_{OS}	Input offset current	R_{IN} = 100 kΩ, OPA388, OPA2388				±700	
			T_A = 0°C to +85°C			±800	
			T_A = –40°C to +125°C			±800	
		R_{IN} = 100 kΩ, OPA4388				±1000	
			T_A = 0°C to +85°C			±1100	
			T_A = –40°C to +125°C			±1100	
NOISE							
E_N	Input voltage noise	f = 0.1 Hz to 10 Hz			0.14		μV_{PP}
e_N	Input voltage noise density	f = 10 Hz			7		nV/√Hz
		f = 100 Hz			7		
		f = 1 kHz			7		
		f = 10 kHz			7		
I_N	Input current noise density	f = 1 kHz			100		fA/√Hz
INPUT VOLTAGE							
V_{CM}	Common-mode voltage range			(V–) – 0.1		(V+) + 0.1	V
CMRR	Common-mode rejection ratio	(V–) – 0.1 V < V_{CM} < (V+) + 0.1 V	V_S = ±1.25 V OPA388, OPA2388	124	138		dB
			V_S = ±1.25 V OPA4388	102	110		
			V_S = ±2.75 V	124	140		
		(V–) < V_{CM} < (V+) + 0.1 V, T_A = –40°C to +125°C	V_S = ±1.25 V OPA388, OPA2388	114	134		
			V_S = ±1.25 V OPA4388	102	107		
		(V–) – 0.05 V < V_{CM} < (V+) + 0.1 V, T_A = –40°C to +125°C	V_S = ±2.75 V	124	140		
INPUT IMPEDANCE							
z_{id}	Differential input impedance				100 || 2		MΩ || pF
z_{ic}	Common-mode input impedance				60 || 4.5		TΩ || pF

6.7 Electrical Characteristics: VS = ±1.25 V to ±2.75 V (VS = 2.5 to 5.5 V) (continued)

at T_A = 25°C, V_{CM} = V_{OUT} = V_S / 2, and R_{LOAD} = 10 kΩ connected to V_S / 2 (unless otherwise noted)

PARAMETER		TEST CONDITIONS		MIN	TYP	MAX	UNIT
OPEN-LOOP GAIN							
A_{OL}	Open-loop voltage gain	(V–) + 0.15 V < V_O < (V+) – 0.15 V, R_{LOAD} = 10 kΩ		126	148		dB
		(V–) + 0.15 V < V_O < (V+) – 0.15 V, R_{LOAD} = 10 kΩ, T_A = –40°C to +125°C	OPA388, OPA2388	120	126		
		(V–) + 0.15 V < V_O < (V+) – 0.15 V, R_{LOAD} = 10 kΩ, V_S = 5.5 V T_A = –40°C to +125°C	OPA4388	120	126		
		(V–) + 0.25 V < V_O < (V+) – 0.25 V, R_{LOAD} = 2 kΩ		126	148		
		(V–) + 0.30 V < V_O < (V+) – 0.30 V, R_{LOAD} = 2 kΩ	OPA388, OPA2388	120	148		
		(V–) + 0.30 V < V_O < (V+) – 0.30 V, R_{LOAD} = 2 kΩ, V_S = 5.5 V T_A = –40°C to +125°C	OPA4388	120	126		
FREQUENCY RESPONSE							
GBW	Unity-gain bandwidth				10		MHz
SR	Slew rate	G = 1, 4-V step			5		V/µs
THD+N	Total harmonic distortion + noise	G = 1, f = 1 kHz, V_O = 1 V_{RMS}			0.0005%		
t_S	Settling time	To 0.1%	V_S = ±2.5 V, G = 1, 1-V step		0.75		µs
		To 0.01%	V_S = ±2.5 V, G = 1, 1-V step		2		µs
t_{OR}	Overload recovery time	V_{IN} × G = V_S			10		µs
OUTPUT							
V_O	Voltage output swing from rail	Positive rail	No load		1	15	mV
			R_{LOAD} = 10 kΩ		5	20	
			R_{LOAD} = 2 kΩ		20	50	
		Negative rail	No load		5	15	
			R_{LOAD} = 10 kΩ		10	20	
			R_{LOAD} = 2 kΩ		40	60	
		T_A = –40°C to +125°C, both rails, R_{LOAD} = 10 kΩ			10	25	
I_{SC}	Short-circuit current	V_S = 5.5 V			±60		mA
		V_S = 2.5 V			±30		mA
C_{LOAD}	Capacitive load drive	See Figure 6-26					
Z_O	Open-loop output impedance	f = 1 MHz, I_O = 0 A, see Figure 6-25			100		Ω
POWER SUPPLY							
I_Q	Quiescent current per amplifier	V_S = ±1.25 V (V_S = 2.5 V)	I_O = 0 A		1.7	2.4	mA
			T_A = –40°C to +125°C, I_O = 0 A		1.7	2.4	
		V_S = ±2.75 V (V_S = 5.5 V)	I_O = 0 A		1.9	2.6	
			T_A = –40°C to +125°C, I_O = 0 A		1.9	2.6	

6.8 Typical Characteristics

at T_A = 25°C, V_S = ±2.5 V, V_{CM} = V_S / 2, R_{LOAD} = 10 kΩ connected to V_S / 2, and C_L = 100 pF (unless otherwise noted)

Table 6-1. Table of Graphs

DESCRIPTION	FIGURE
Offset Voltage Production Distribution	Figure 6-1
Offset Voltage Drift Distribution From –40°C to +125°C	Figure 6-2
Offset Voltage vs Temperature	Figure 6-3
Offset Voltage vs Common-Mode Voltage	Figure 6-4
Offset Voltage vs Power Supply: OPA388 and OPA2388	Figure 6-5
Offset Voltage vs Power Supply: OPA4388	Figure 6-6
Offset Voltage Long Term Drift	Figure 6-7
Open-Loop Gain and Phase vs Frequency	Figure 6-8
Closed-Loop Gain and Phase vs Frequency	Figure 6-9
Input Bias Current vs Common-Mode Voltage	Figure 6-10
Input Bias Current vs Temperature	Figure 6-11
Output Voltage Swing vs Output Current (Maximum Supply)	Figure 6-12
CMRR and PSRR vs Frequency	Figure 6-13
CMRR vs Temperature	Figure 6-14
PSRR vs Temperature	Figure 6-15
0.1-Hz to 10-Hz Noise	Figure 6-16
Input Voltage Noise Spectral Density vs Frequency	Figure 6-17
THD+N Ratio vs Frequency	Figure 6-18
THD+N vs Output Amplitude	Figure 6-19
Spectral Content	Figure 6-20, Figure 6-21
Quiescent Current vs Supply Voltage	Figure 6-22
Quiescent Current vs Temperature	Figure 6-23
Open-Loop Gain vs Temperature	Figure 6-24
Open-Loop Output Impedance vs Frequency	Figure 6-25
Small-Signal Overshoot vs Capacitive Load (10-mV Step)	Figure 6-26
No Phase Reversal	Figure 6-27
Positive Overload Recovery	Figure 6-28
Negative Overload Recovery	Figure 6-29
Small-Signal Step Response (10-mV Step)	Figure 6-30, Figure 6-31
Large-Signal Step Response (4-V Step)	Figure 6-32 , Figure 6-33
Settling Time	Figure 6-34, Figure 6-35
Short-Circuit Current vs Temperature	Figure 6-36
Maximum Output Voltage vs Frequency	Figure 6-37
EMIRR vs Frequency	Figure 6-38

6.8 Typical Characteristics (continued)

at T_A = 25°C, V_S = ±2.5 V, V_{CM} = V_S / 2, R_{LOAD} = 10 kΩ connected to V_S / 2, and C_L = 100 pF (unless otherwise noted)

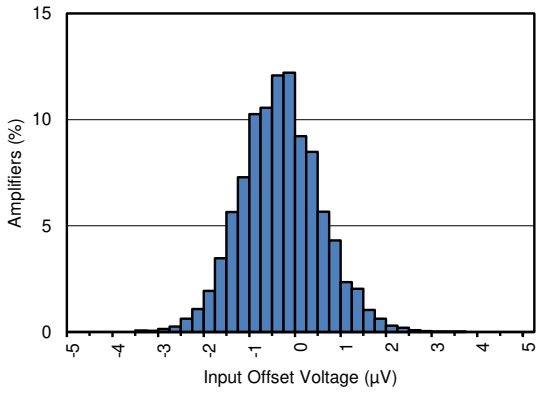

Figure 6-1. Offset Voltage Production Distribution

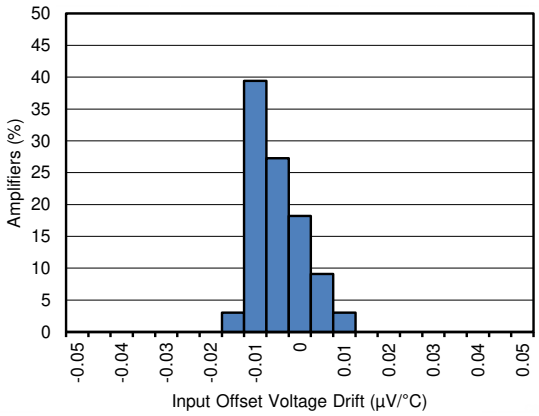

Figure 6-2. Offset Voltage Drift Distribution From –40°C to +125°C

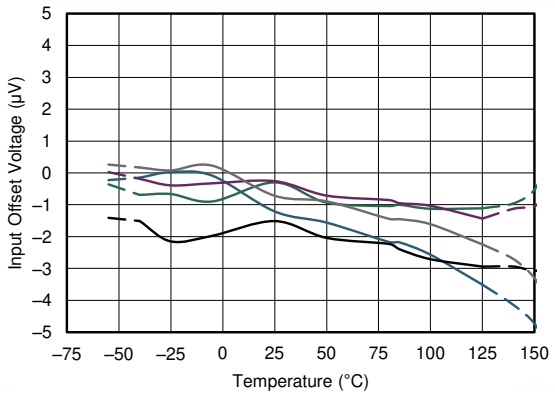

Figure 6-3. Offset Voltage vs Temperature

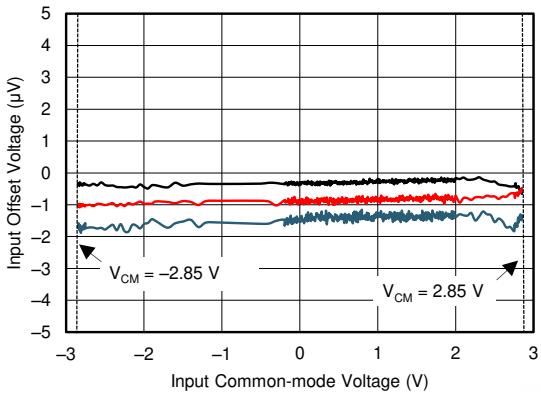

Figure 6-4. Offset Voltage vs Common-Mode Voltage

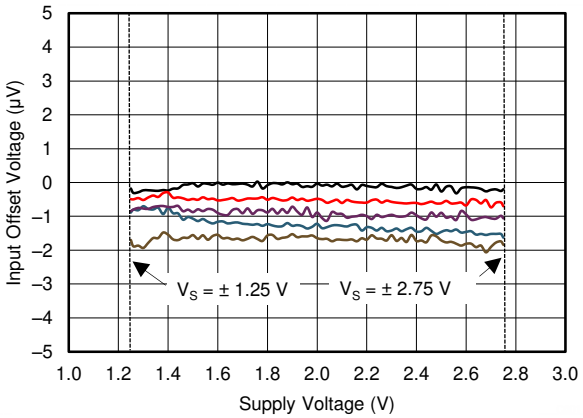

Figure 6-5. Offset Voltage vs Supply Voltage: OPA388 and OPA2388

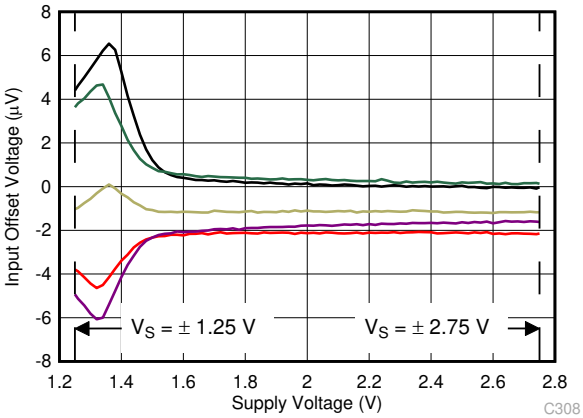

Figure 6-6. Offset Voltage vs Supply Voltage: OPA4388

6.8 Typical Characteristics (continued)

at T_A = 25°C, V_S = ±2.5 V, V_{CM} = V_S / 2, R_{LOAD} = 10 kΩ connected to V_S / 2, and C_L = 100 pF (unless otherwise noted)

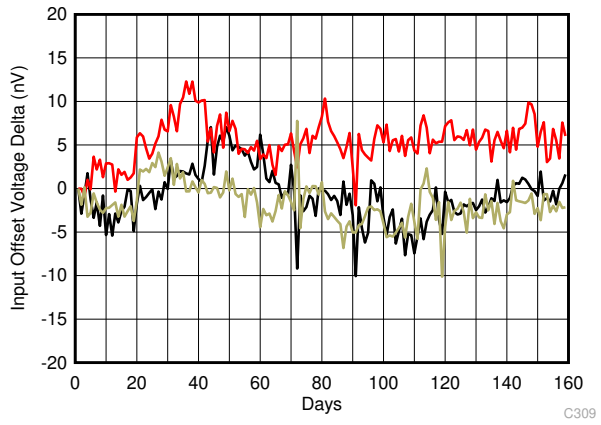

Figure 6-7. Offset Voltage Long Term Drift

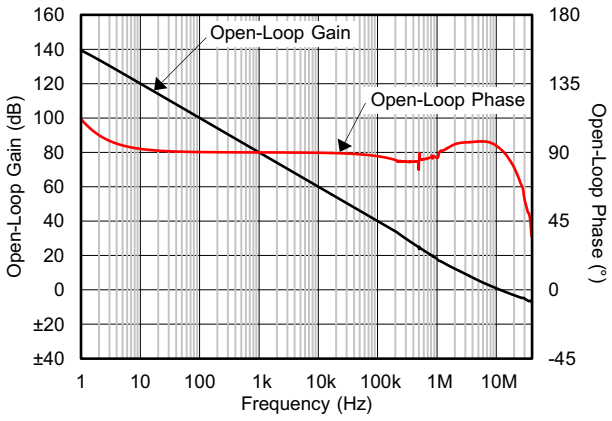

Figure 6-8. Open-Loop Gain and Phase vs Frequency

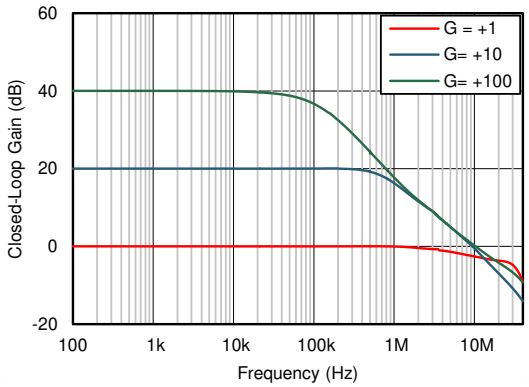

Figure 6-9. Closed-Loop Gain and Phase vs Frequency

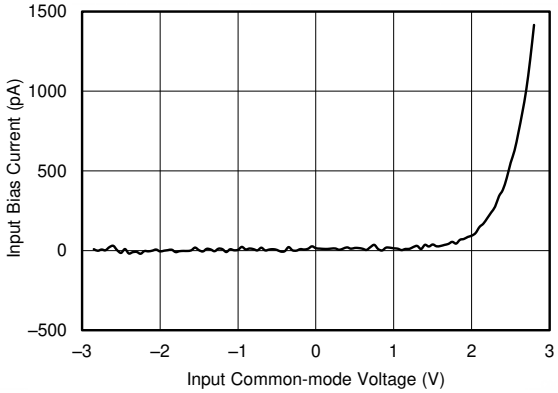

Figure 6-10. Input Bias Current vs Common-Mode Voltage

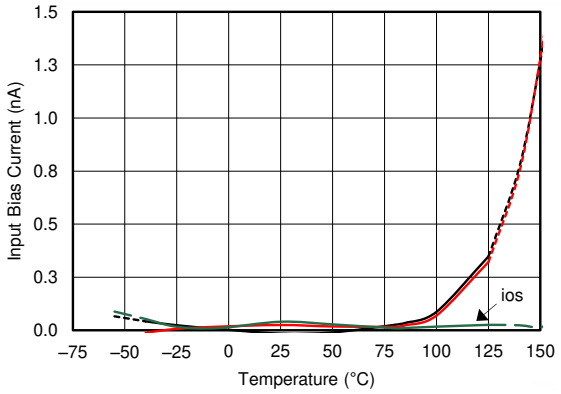

Figure 6-11. Input Bias Current vs Temperature

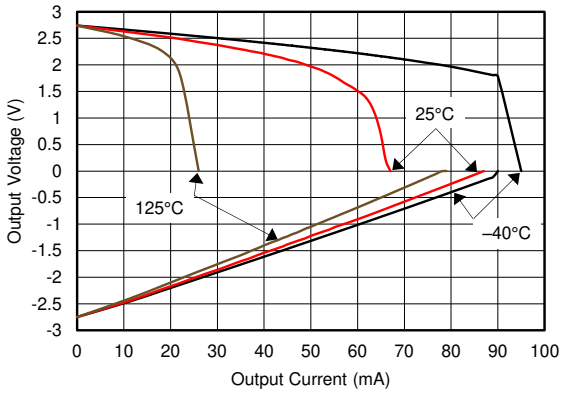

Figure 6-12. Output Voltage Swing vs Output Current (Maximum Supply)

6.8 Typical Characteristics (continued)

at T_A = 25°C, V_S = ±2.5 V, V_{CM} = V_S / 2, R_{LOAD} = 10 kΩ connected to V_S / 2, and C_L = 100 pF (unless otherwise noted)

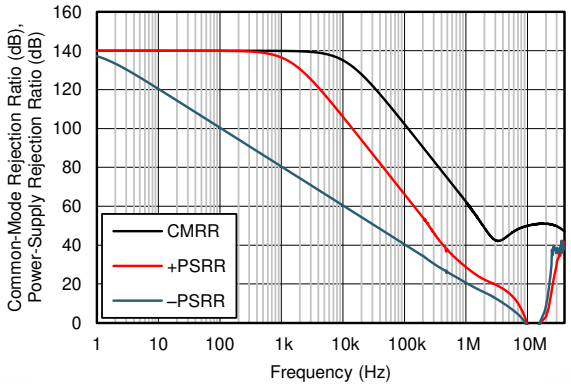

Figure 6-13. CMRR and PSRR vs Frequency

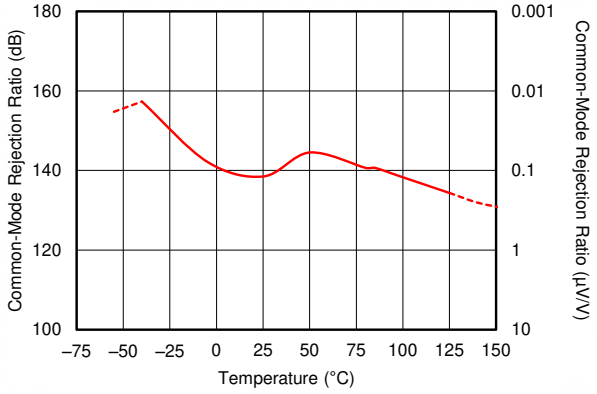

Figure 6-14. CMRR vs Temperature

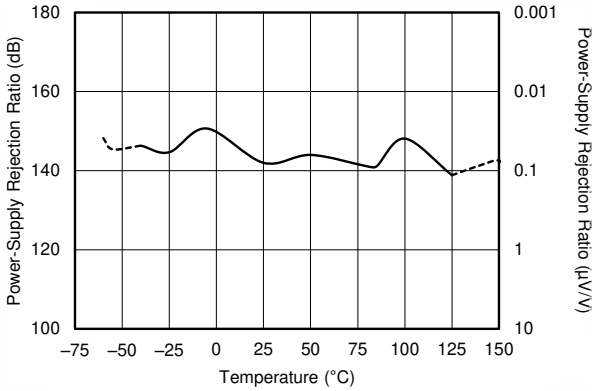

Figure 6-15. PSRR vs Temperature

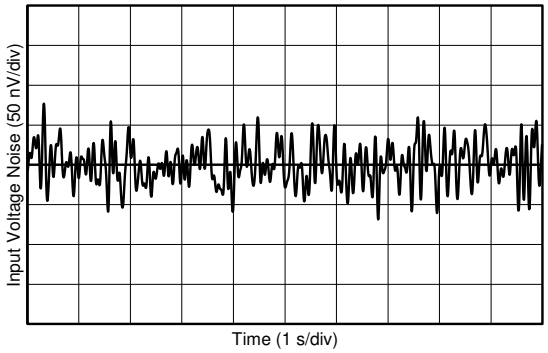

Figure 6-16. 0.1-Hz to 10-Hz Noise

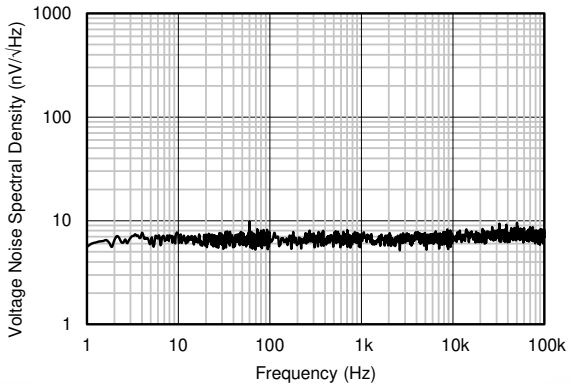

Figure 6-17. Input Voltage Noise Spectral Density vs Frequency

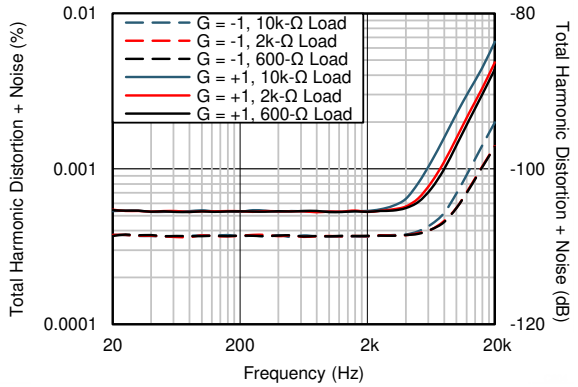

Figure 6-18. THD+N Ratio vs Frequency

6.8 Typical Characteristics (continued)

at T_A = 25°C, V_S = ±2.5 V, V_{CM} = V_S / 2, R_{LOAD} = 10 kΩ connected to V_S / 2, and C_L = 100 pF (unless otherwise noted)

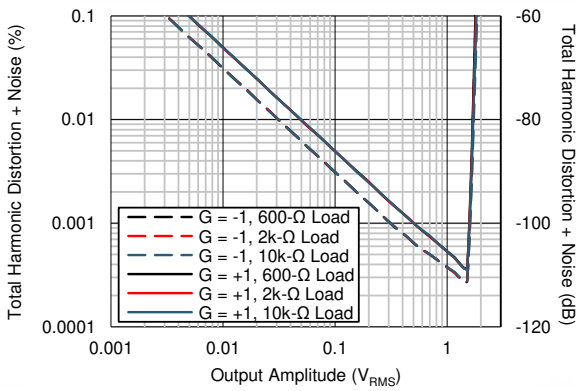

Figure 6-19. THD+N vs Output Amplitude

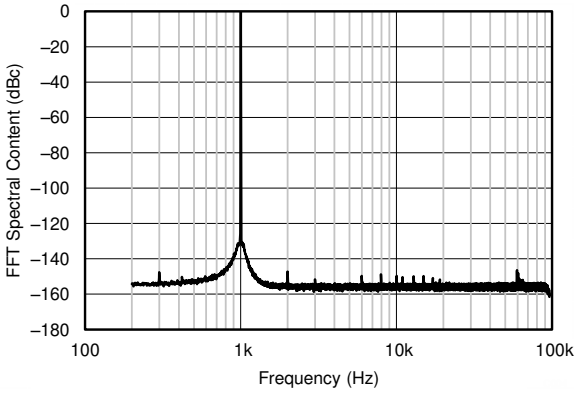

G = +1, f = 1 kHz, V_O = 4.5 V_{PP}, R_L = 10 kΩ, BW = 90 kHz

Figure 6-20. Spectral Content (With 10-kΩ Load)

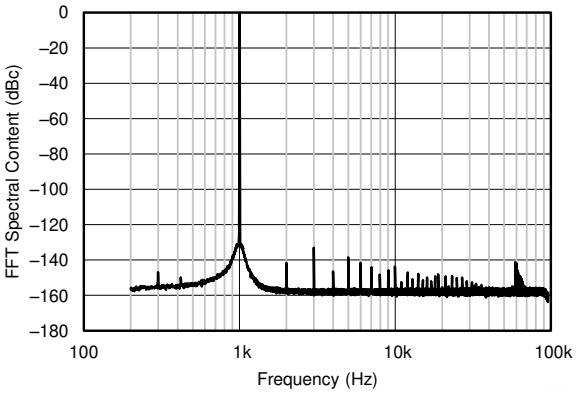

G = +1, f = 1 kHz, V_O = 4.5 V_{PP}, R_L = 2 kΩ, BW = 90 kHz

Figure 6-21. Spectral Content (With 2-kΩ Load)

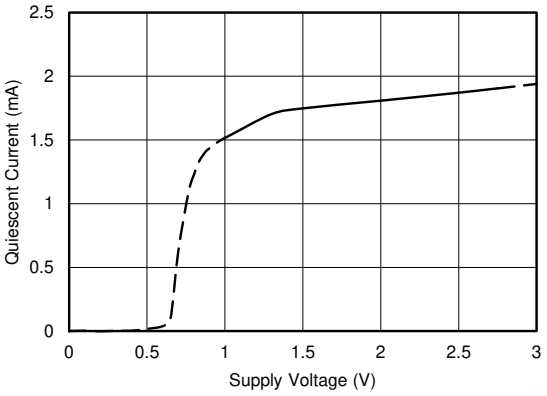

Figure 6-22. Quiescent Current vs Supply Voltage

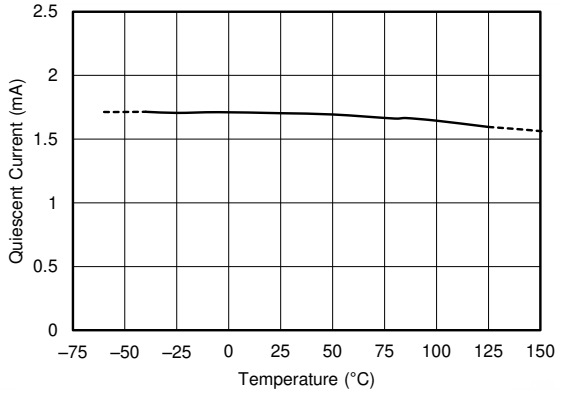

Figure 6-23. Quiescent Current vs Temperature

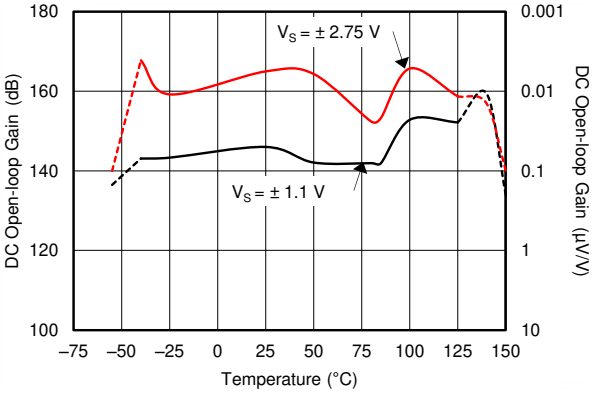

Figure 6-24. Open-Loop Gain vs Temperature

6.8 Typical Characteristics (continued)

at T_A = 25°C, V_S = ±2.5 V, V_{CM} = V_S / 2, R_{LOAD} = 10 kΩ connected to V_S / 2, and C_L = 100 pF (unless otherwise noted)

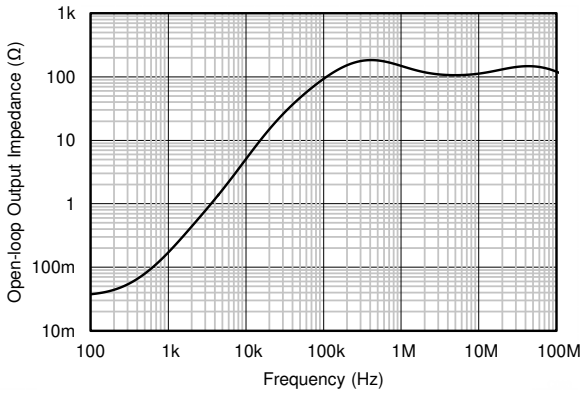

Figure 6-25. Open-Loop Output Impedance vs Frequency

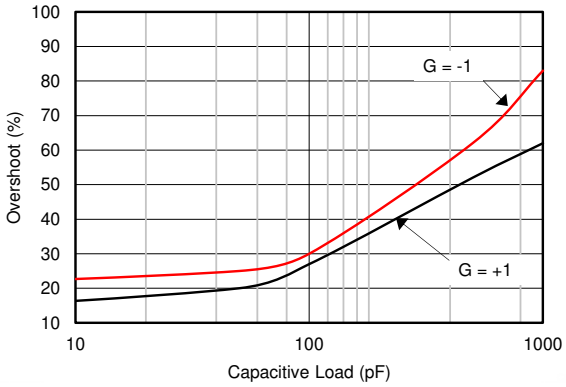

Figure 6-26. Small-Signal Overshoot vs Capacitive Load (10-mV Step)

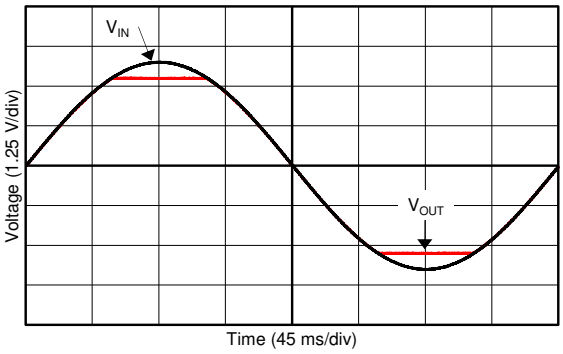

Figure 6-27. No Phase Reversal

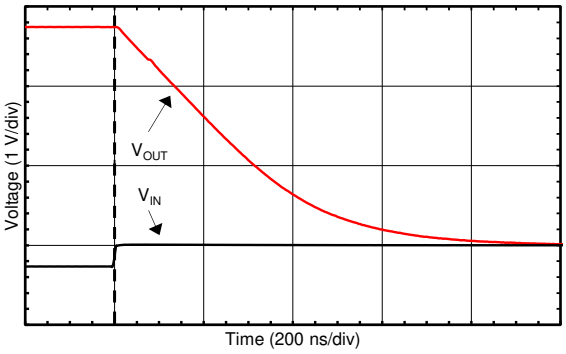

Figure 6-28. Positive Overload Recovery

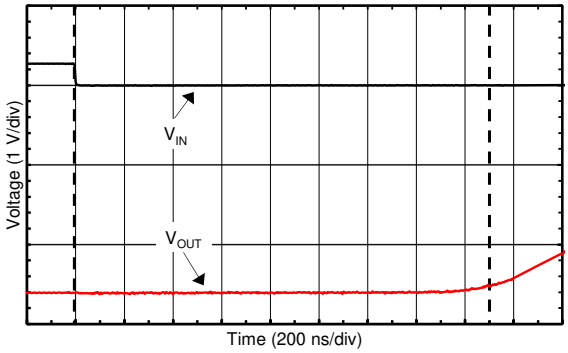

Figure 6-29. Negative Overload Recovery

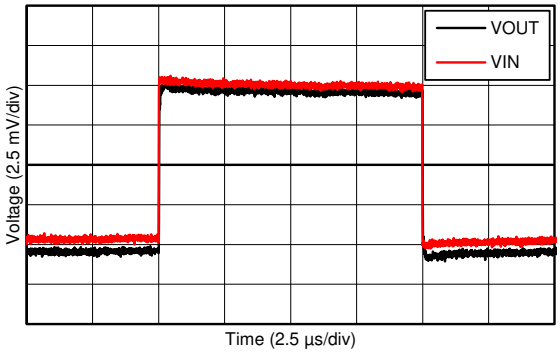

G = +1

Figure 6-30. Small-Signal Step Response (10-mV Step)

6.8 Typical Characteristics (continued)

at T_A = 25°C, V_S = ±2.5 V, V_{CM} = V_S / 2, R_{LOAD} = 10 kΩ connected to V_S / 2, and C_L = 100 pF (unless otherwise noted)

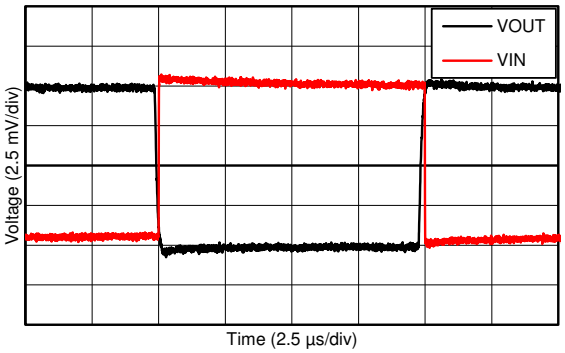

G = –1

Figure 6-31. Small-Signal Step Response (10-mV Step)

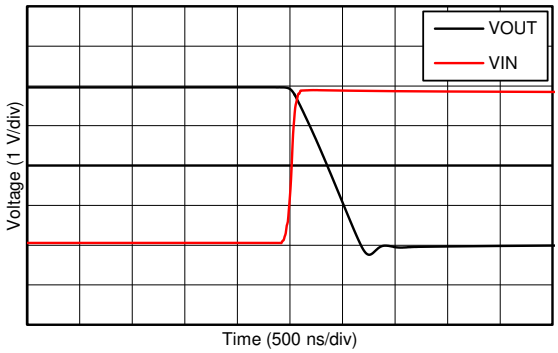

Falling output

Figure 6-32. Large-Signal Step Response (4-V Step)

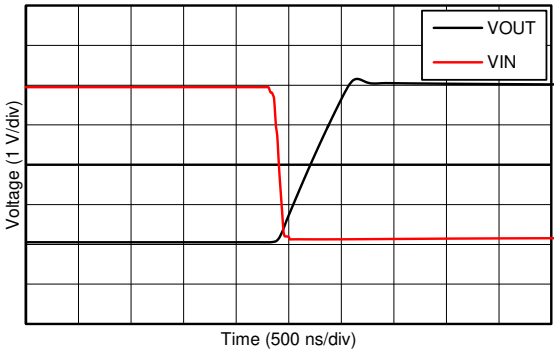

Rising output

Figure 6-33. Large-Signal Step Response (4-V Step)

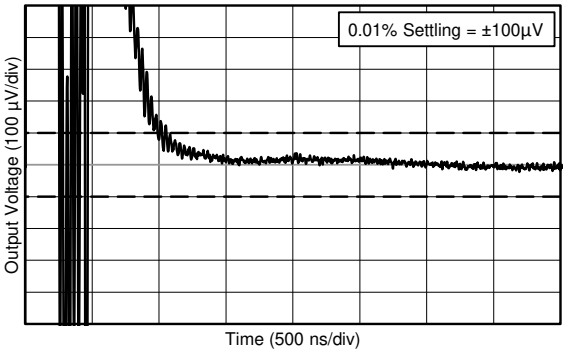

0.01% settling = ±100 µV

Figure 6-34. Settling Time (1-V Positive Step)

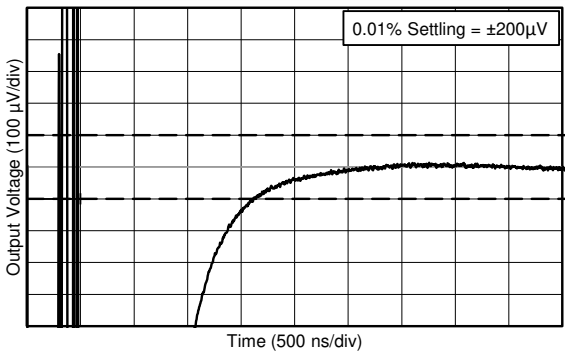

0.01% settling = ±200 µV

Figure 6-35. Settling Time (1-V Negative Step)

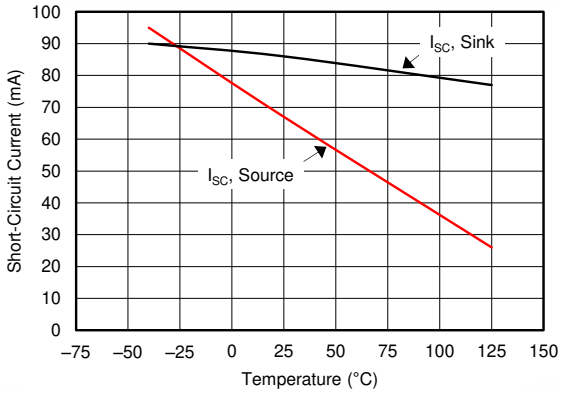

Figure 6-36. Short-Circuit Current vs Temperature

6.8 Typical Characteristics (continued)

at T_A = 25°C, V_S = ±2.5 V, V_{CM} = V_S / 2, R_{LOAD} = 10 kΩ connected to V_S / 2, and C_L = 100 pF (unless otherwise noted)

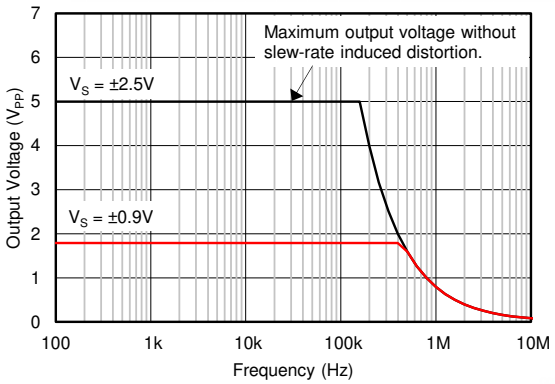

Figure 6-37. Maximum Output Voltage vs Frequency

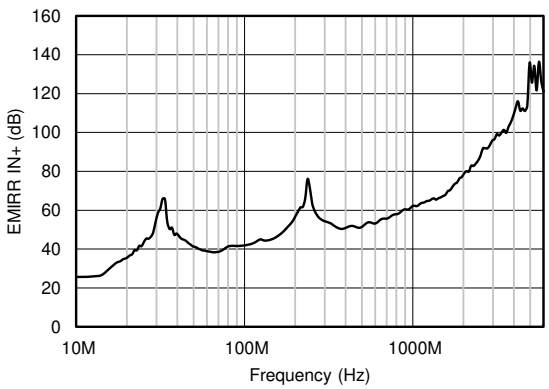

P_{RF} = –10 dBm

Figure 6-38. EMIRR vs Frequency

7 Detailed Description

7.1 Overview

The OPAx388 family of zero-drift amplifiers is engineered with the unique combination of a proprietary precision auto-calibration technique paired with a low-noise, low-ripple, input charge pump. These amplifiers offer ultra-low input offset voltage and drift and achieve excellent input and output dynamic linearity. The OPAx388 operate from 2.5 V to 5.5 V, is unity-gain stable, and are designed for a wide range of general-purpose and precision applications. The integrated, low-noise charge pump allows true rail-to-rail input common-mode operation without distortion associated with complementary rail-to-rail input topologies (input crossover distortion). The OPAx388 strengths also include 10-MHz bandwidth, 7-nV/$\sqrt{\text{Hz}}$ noise spectral density, and no 1/f noise, making the OPAx388 optimal for interfacing with sensor modules and buffering high-fidelity, digital-to-analog converters (DACs).

7.2 Functional Block Diagram

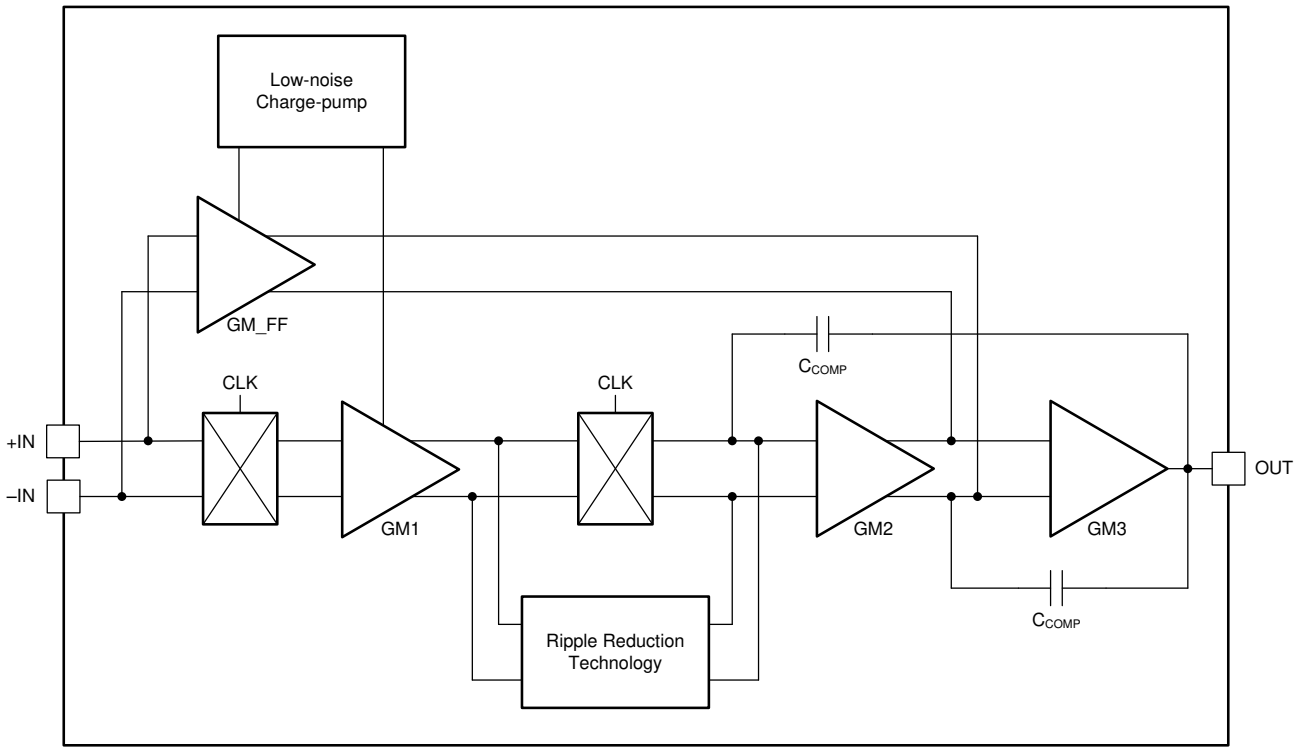

7.3 Feature Description

7.3.1 Operating Voltage

The OPAx388 family of operational amplifiers can be used with single or dual supplies from an operating range of V_S = 2.5 V (±1.25 V) up to 5.5 V (±2.75 V). Supply voltages greater than 7 V can permanently damage the device (see the *Absolute Maximum Ratings* table). Key parameters that vary over the supply voltage or temperature range are shown in the *Typical Characteristics* section.

7.3.2 Input Voltage and Zero-Crossover Functionality

The OPAx388 input common-mode voltage range extends 0.1 V beyond the supply rails. This amplifier family is designed to cover the full range without the troublesome transition region found in some other rail-to-rail amplifiers. Operating a complementary rail-to-rail input amplifier with signals traversing the transition region results in unwanted non-linear behavior and polluted spectral content. Figure 7-1 and Figure 7-2 contrast the performance of a traditional complementary rail-to-rail input stage amplifier with the performance of the zero-crossover OPA388. Significant harmonic content and distortion is generated during the differential pair transition (such a transition does not exist in the OPA388). Crossover distortion is eliminated through the use of a single differential pair coupled with an internal low-noise charge pump. The OPAx388 maintains noise, bandwidth, and offset performance throughout the input common-mode range, thus reducing printed circuit board (PCB) and bill of materials (BOM) complexity through the reduction of power-supply rails.

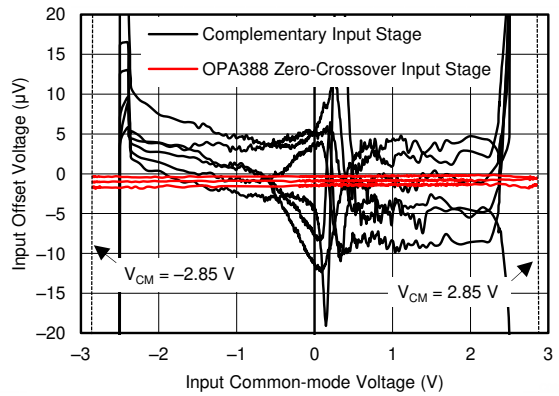

Figure 7-1. Input Crossover Distortion Nonlinearity

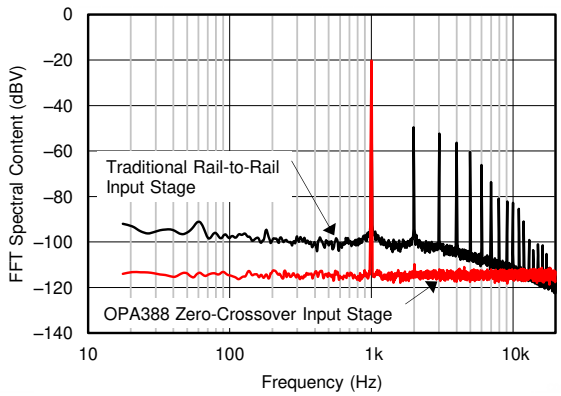

Figure 7-2. Input Crossover Distortion Spectral Content

Typically, input bias current is approximately ±30 pA. Input voltages exceeding the power supplies, however, can cause excessive current to flow into or out of the input pins. Momentary voltages greater than the power supply can be tolerated if the input current is limited to 10 mA. This limitation is easily accomplished with an input resistor, as shown in Figure 7-3.

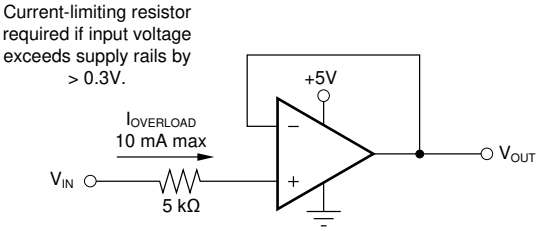

Figure 7-3. Input Current Protection

7.3.3 Input Differential Voltage

The typical input bias current of the OPAx388 during normal operation is approximately 30 pA. In overdriven conditions, the bias current can increase significantly. The most common cause of an overdriven condition occurs when the operational amplifier is outside of the linear range of operation. When the output of the operational amplifier is driven to one of the supply rails, the feedback loop requirements cannot be satisfied and a differential input voltage develops across the input pins. This differential input voltage results in activation of parasitic diodes inside the front-end input chopping switches that combine with 10-kΩ electromagnetic interference (EMI) filter resistors to create the equivalent circuit shown in Figure 7-4. Notice that the input bias current remains within specification in the linear region.

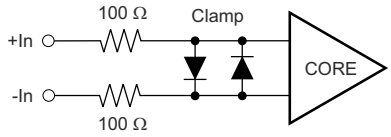

Figure 7-4. Equivalent Input Circuit

7.3.4 Internal Offset Correction

The OPA388 family of operational amplifiers uses an auto-calibration technique with a time-continuous, 200-kHz operational amplifier in the signal path. This amplifier is zero-corrected every 5 µs using a proprietary technique. At power-up, the amplifier requires approximately 1 ms to achieve the specified V_{OS} accuracy. This design has no aliasing or flicker noise.

7.3.5 EMI Susceptibility and Input Filtering

Operational amplifiers vary in susceptibility to EMI. If conducted EMI enters the operational amplifier, the dc offset at the amplifier output can shift from its nominal value when EMI is present. This shift is a result of signal rectification associated with the internal semiconductor junctions. Although all operational amplifier pin functions can be affected by EMI, the input pins are likely to be the most susceptible. The OPAx388 operational amplifier family incorporates an internal input low-pass filter that reduces the amplifier response to EMI. Both common-mode and differential-mode filtering are provided by the input filter. The filter is designed for a cutoff frequency of approximately 20 MHz (–3 dB), with a rolloff of 20 dB per decade.

7.4 Device Functional Modes

The OPA388 has a single functional mode and is operational when the power-supply voltage is greater than 2.5 V (±1.25 V). The maximum specified power-supply voltage for the OPAx388 is 5.5 V (±2.75 V).

8 Application and Implementation

Note

Information in the following applications sections is not part of the TI component specification, and TI does not warrant its accuracy or completeness. TI's customers are responsible for determining suitability of components for their purposes. Customers should validate and test their design implementation to confirm system functionality.

8.1 Application Information

The OPAx388 is a unity-gain stable, precision operational amplifier family free from unexpected output and phase reversal. The use of proprietary zero-drift circuitry gives the benefit of low input offset voltage over time and temperature, as well as lowering the 1/f noise component. As a result of the high PSRR, these devices work well in applications that run directly from battery power without regulation. The OPAx388 family is optimized for full rail-to-rail input, allowing for low-voltage, single-supply operation or split-supply use. These miniature, high-precision, low-noise amplifiers offer high-impedance inputs that have a common-mode range 100 mV beyond the supplies without input crossover distortion and a rail-to-rail output that swings within 5 mV of the supplies under normal test conditions. The OPAx388 series of precision amplifiers is designed for upstream analog signal chain applications in low or high gains, as well as downstream signal chain functions such as DAC buffering.

8.2 Typical Applications

8.2.1 Bidirectional Current-Sensing

This single-supply, low-side, bidirectional current-sensing solution detects load currents from –1 A to +1 A. The single-ended output spans from 110 mV to 3.19 V. This design uses the OPAx388 because of its low offset voltage and rail-to-rail input and output. One of the amplifiers is configured as a difference amplifier and the other amplifier provides the reference voltage.

Figure 8-1 shows the solution.

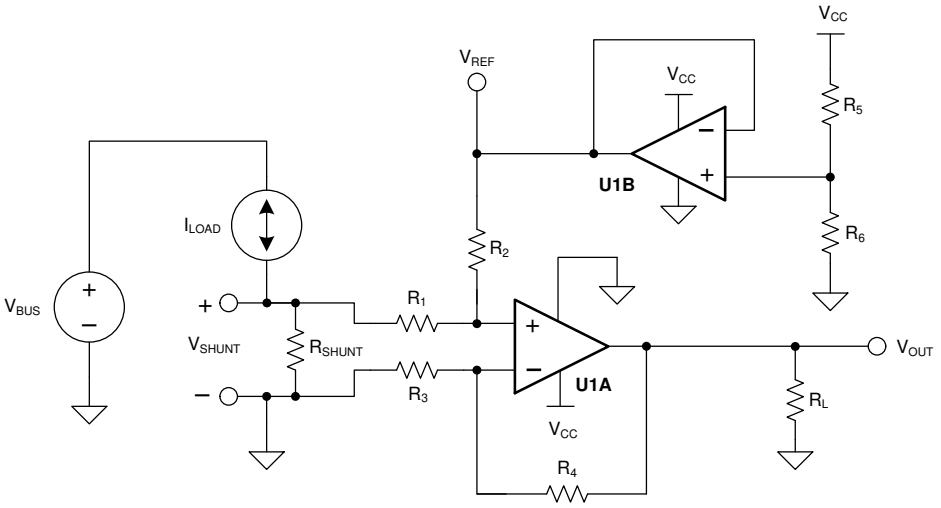

Figure 8-1. Bidirectional Current-Sensing Schematic

8.2.1.1 Design Requirements

This solution has the following requirements:

- Supply voltage: 3.3 V
- Input: –1 A to 1 A
- Output: 1.65 V ±1.54 V (110 mV to 3.19 V)

8.2.1.2 Detailed Design Procedure

The load current, I_{LOAD}, flows through the shunt resistor (R_{SHUNT}) to develop the shunt voltage, V_{SHUNT}. The shunt voltage is then amplified by the difference amplifier consisting of U1A and R_1 through R_4. The gain of the difference amplifier is set by the ratio of R_4 to R_3. To minimize errors, set $R_2 = R_4$ and $R_1 = R_3$. The reference voltage, V_{REF}, is supplied by buffering a resistor divider using U1B. The transfer function is given by Equation 1.

$$V_{OUT} = V_{SHUNT} \times Gain_{Diff\_Amp} + V_{REF} \quad (1)$$

where

- $V_{SHUNT} = I_{LOAD} \times R_{SHUNT}$
- $Gain_{Diff\_Amp} = \frac{R_4}{R_3}$
- $V_{REF} = V_{CC} \times \left(\frac{R_6}{R_5 + R_6} \right)$

There are two types of errors in this design: offset and gain. Gain errors are introduced by the tolerance of the shunt resistor and the ratios of R_4 to R_3 and, similarly, R_2 to R_1. Offset errors are introduced by the voltage divider (R_5 and R_6) and how closely the ratio of R_4 / R_3 matches R_2 / R_1. The latter value affects the CMRR of the difference amplifier, ultimately translating to an offset error.

The value of V_{SHUNT} is the ground potential for the system load because V_{SHUNT} is a low-side measurement. Therefore, a maximum value must be placed on V_{SHUNT}. In this design, the maximum value for V_{SHUNT} is set to 100 mV. Equation 2 calculates the maximum value of the shunt resistor given a maximum shunt voltage of 100 mV and maximum load current of 1 A.

$$R_{SHUNT(Max)} = \frac{V_{SHUNT(Max)}}{I_{LOAD(Max)}} = \frac{100\ mV}{1\ A} = 100\ m\Omega \quad (2)$$

The tolerance of R_{SHUNT} is directly proportional to cost. For this design, a shunt resistor with a tolerance of 0.5% was selected. If greater accuracy is required, select a 0.1% resistor or better.

The load current is bidirectional; therefore, the shunt voltage range is –100 mV to 100 mV. This voltage is divided down by R_1 and R_2 before reaching the operational amplifier, U1A. Make sure that the voltage present at the noninverting node of U1A is within the common-mode range of the device. Therefore, use an operational amplifier, such as the OPA388, that has a common-mode range that extends below the negative supply voltage. Finally, to minimize offset error, note that the OPA388 has a typical offset voltage of merely ±0.25 µV (±5 µV maximum).

Given a symmetric load current of –1 A to 1 A, the voltage divider resistors (R_5 and R_6) must be equal. To be consistent with the shunt resistor, a tolerance of 0.5% was selected. To minimize power consumption, 10-kΩ resistors were used.

To set the gain of the difference amplifier, the common-mode range and output swing of the OPA388 must be considered. Equation 3 and Equation 4 depict the typical common-mode range and maximum output swing, respectively, of the OPA388 given a 3.3-V supply.

$$-100\ \text{mV} < V_{CM} < 3.4\ \text{V} \tag{3}$$

$$100\ \text{mV} < V_{OUT} < 3.2\ \text{V} \tag{4}$$

The gain of the difference amplifier can now be calculated as shown in Equation 5.

$$\text{Gain}_{\text{Diff\_Amp}} = \frac{V_{OUT\_Max} - V_{OUT\_Min}}{R_{SHUNT} \times (I_{MAX} - I_{MIN})} = \frac{3.2\ \text{V} - 100\ \text{mV}}{100\ \text{m}\Omega \times [1\ \text{A} - (-1\text{A})]} = 15.5\ \frac{\text{V}}{\text{V}} \tag{5}$$

The resistor value selected for R_1 and R_3 was 1 kΩ. 15.4 kΩ was selected for R_2 and R_4 because this number is the nearest standard value. Therefore, the ideal gain of the difference amplifier is 15.4 V/V.

The gain error of the circuit primarily depends on R_1 through R_4. As a result of this dependence, 0.1% resistors were selected. This configuration reduces the likelihood that the design requires a two-point calibration. A simple one-point calibration, if desired, removes the offset errors introduced by the 0.5% resistors.

8.2.1.3 Application Curve

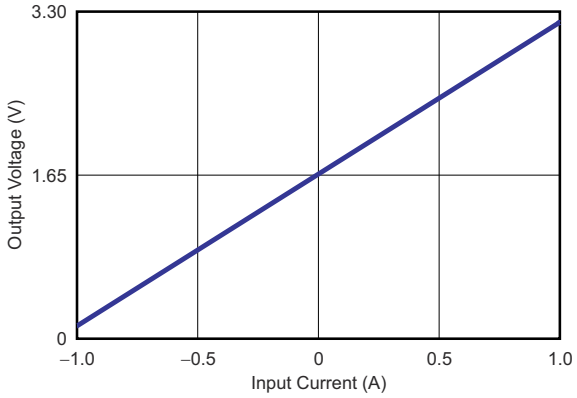

Figure 8-2. Bidirectional Current-Sensing Circuit Performance: Output Voltage vs Input Current

8.2.2 Single Operational Amplifier Bridge Amplifier

Figure 8-3 shows the basic configuration for a bridge amplifier.

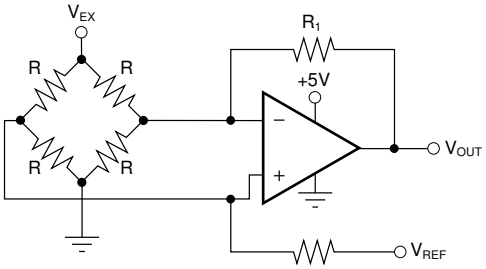

Figure 8-3. Single Operational Amplifier Bridge Amplifier Schematic

8.2.3 Precision, Low-Noise, DAC Buffer

The OPA388 can be used for a precision DAC buffer, as shown in Figure 8-4, in conjunction with the DAC8830.

The OPA388 provides an ultra-low drift, precision output buffer for the DAC. A wide range of DAC codes can be used in the linear region because the OPA388 employs zero-crossover technology. A precise reference is essential for maximum accuracy because the DAC8830 is a 16-bit converter.

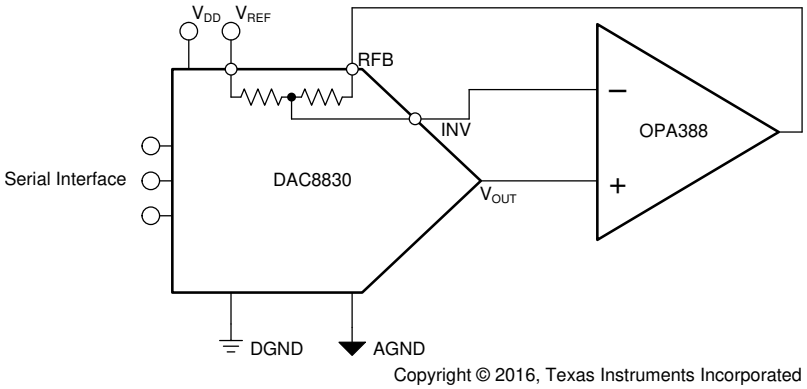

Figure 8-4. Precision DAC Buffer

8.2.4 Load Cell Measurement

Figure 8-5 shows the OPA388 in a high-CMRR dual-op amp instrumentation amplifier with a trim resistor and 6-wire load cell for precision measurement. Figure 8-6 illustrates the output voltage as a function of load cell resistance change, along with the nonlinearity of the system.

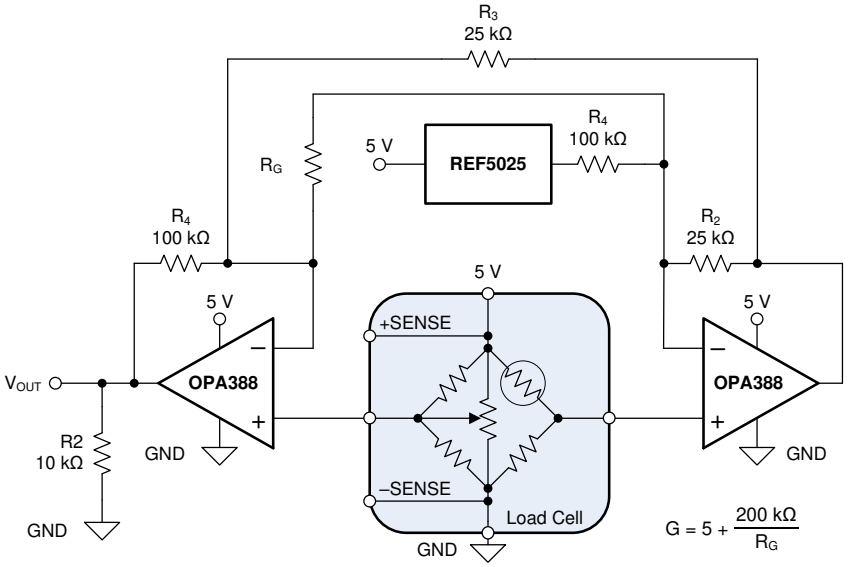

Figure 8-5. Load Cell Measurement Schematic

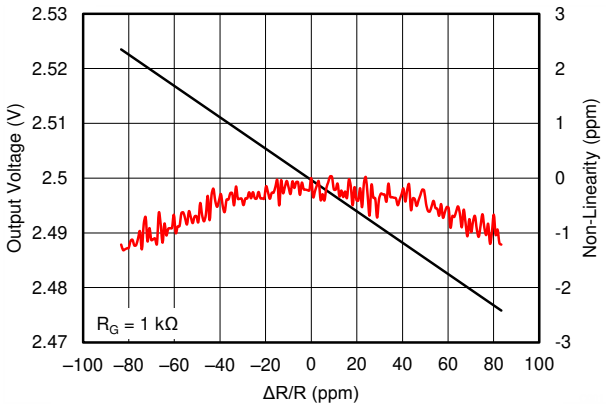

Figure 8-6. Load Cell Measurement Output

9 Power Supply Recommendations

The OPAx388 family of devices is specified for operation from 2.5 V to 5.5 V (±1.25 V to ±2.75 V). Parameters that can exhibit significant variance with regard to operating voltage are presented in the *Typical Characteristics* section.

10 Layout

10.1 Layout Guidelines

Paying attention to good layout practice is always recommended. Keep traces short and, when possible, use a printed-circuit board (PCB) ground plane with surface-mount components placed as close to the device pins as possible. Place a 0.1-µF capacitor closely across the supply pins. These guidelines must be applied throughout the analog circuit to improve performance and provide benefits such as reducing the electromagnetic interference (EMI) susceptibility.

For lowest offset voltage and precision performance, circuit layout and mechanical conditions must be optimized. Avoid temperature gradients that create thermoelectric (Seebeck) effects in the thermocouple junctions formed from connecting dissimilar conductors. These thermally-generated potentials can be made to cancel by assuring they are equal on both input terminals. Other layout and design considerations include:

- Use low thermoelectric-coefficient conditions (avoid dissimilar metals).
- Thermally isolate components from power supplies or other heat sources.
- Shield operational amplifier and input circuitry from air currents, such as cooling fans.

Following these guidelines reduces the likelihood of junctions being at different temperatures, which can cause thermoelectric voltage drift of 0.1 µV/°C or higher, depending on materials used.

10.2 Layout Example

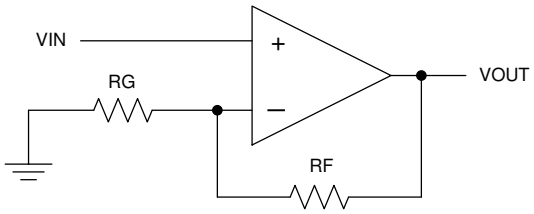

Figure 10-1. Schematic Representation

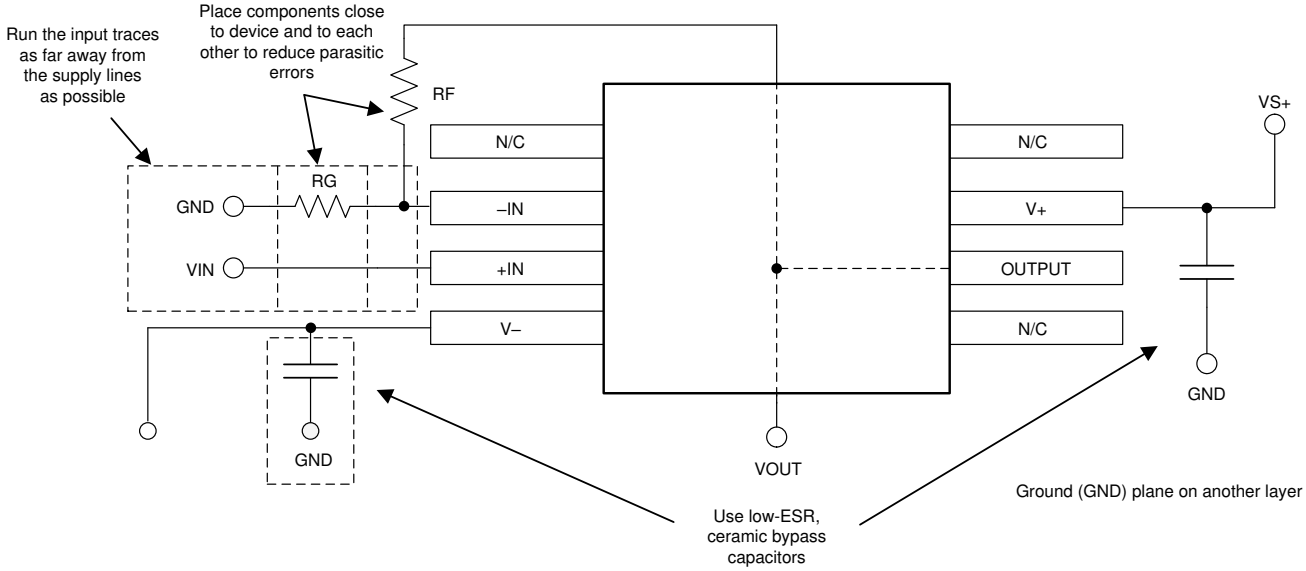

Figure 10-2. OPA388 Layout Example

11 Device and Documentation Support

11.1 Device Support

11.1.1 Development Support

11.1.1.1 TINA-TI™ Simulation Software (Free Download)

TINA-TI™ simulation software is a simple, powerful, and easy-to-use circuit simulation program based on a SPICE engine. TINA-TI simulation software is a free, fully-functional version of the TINA™ software, preloaded with a library of macromodels, in addition to a range of both passive and active models. TINA-TI simulation software provides all the conventional dc, transient, and frequency domain analysis of SPICE, as well as additional design capabilities.

Available as a free download from the Analog eLab Design Center, TINA-TI simulation software offers extensive post-processing capability that allows users to format results in a variety of ways. Virtual instruments offer the ability to select input waveforms and probe circuit nodes, voltages, and waveforms, creating a dynamic quick-start tool.

Note

These files require that either the TINA software or TINA-TI software be installed. Download the free TINA-TI simulation software from the TINA-TI™ software folder.

11.1.1.2 TI Precision Designs

The OPAx388 family is featured on TI Precision Designs, available online at www.ti.com/ww/en/analog/precision-designs/. TI Precision Designs are analog solutions created by TI's precision analog applications experts and offer the theory of operation, component selection, simulation, complete PCB schematic and layout, bill of materials, and measured performance of many useful circuits.

11.2 Documentation Support

11.2.1 Related Documentation

For related documentation see the following:

- Texas Instruments, *Circuit board layout techniques*
- Texas Instruments, *DAC883x 16-Bit, Ultra-Low Power, Voltage-Output Digital-to-Analog Converters* data sheet

11.3 Related Links

Table 11-1 lists quick access links. Categories include technical documents, support and community resources, tools and software, and quick access to sample or buy.

Table 11-1. Related Links

PARTS	PRODUCT FOLDER	SAMPLE & BUY	TECHNICAL DOCUMENTS	TOOLS & SOFTWARE	SUPPORT & COMMUNITY
OPA388	Click here	Click here	Click here	Click here	Click here
OPA2388	Click here	Click here	Click here	Click here	Click here
OPA4388	Click here	Click here	Click here	Click here	Click here

11.4 Receiving Notification of Documentation Updates

To receive notification of documentation updates, navigate to the device product folder on ti.com. Click on *Subscribe to updates* to register and receive a weekly digest of any product information that has changed. For change details, review the revision history included in any revised document.

11.5 Support Resources

TI E2E™ support forums are an engineer's go-to source for fast, verified answers and design help — straight from the experts. Search existing answers or ask your own question to get the quick design help you need.

Linked content is provided "AS IS" by the respective contributors. They do not constitute TI specifications and do not necessarily reflect TI's views; see TI's Terms of Use.

11.6 Trademarks

TINA-TI™ and TI E2E™ are trademarks of Texas Instruments.
TINA™ is a trademark of DesignSoft, Inc.
All trademarks are the property of their respective owners.

11.7 Electrostatic Discharge Caution

This integrated circuit can be damaged by ESD. Texas Instruments recommends that all integrated circuits be handled with appropriate precautions. Failure to observe proper handling and installation procedures can cause damage.

ESD damage can range from subtle performance degradation to complete device failure. Precision integrated circuits may be more susceptible to damage because very small parametric changes could cause the device not to meet its published specifications.

11.8 Glossary

TI Glossary — This glossary lists and explains terms, acronyms, and definitions.

12 Mechanical, Packaging, and Orderable Information

The following pages include mechanical packaging and orderable information. This information is the most current data available for the designated devices. This data is subject to change without notice and revision of this document. For browser-based versions of this data sheet, refer to the left-hand navigation.

PACKAGING INFORMATION

Orderable part number	Status (1)	Material type (2)	Package | Pins	Package qty | Carrier	RoHS (3)	Lead finish/ Ball material (4)	MSL rating/ Peak reflow (5)	Op temp (°C)	Part marking (6)
OPA2388ID	Active	Production	SOIC (D) | 8	75 | TUBE	Yes	SN	Level-2-260C-1 YEAR	-40 to 125	OP2388
OPA2388IDGKR	Active	Production	VSSOP (DGK) | 8	2500 | LARGE T&R	Yes	NIPDAUAG | SN	Level-2-260C-1 YEAR	-40 to 125	1D36
OPA2388IDGKT	Active	Production	VSSOP (DGK) | 8	250 | SMALL T&R	Yes	NIPDAUAG | SN	Level-2-260C-1 YEAR	-40 to 125	1D36
OPA2388IDR	Active	Production	SOIC (D) | 8	2500 | LARGE T&R	Yes	SN	Level-2-260C-1 YEAR	-40 to 125	OP2388
OPA388ID	Active	Production	SOIC (D) | 8	75 | TUBE	Yes	NIPDAU	Level-2-260C-1 YEAR	-40 to 125	OPA388
OPA388IDBVR	Active	Production	SOT-23 (DBV) | 5	3000 | LARGE T&R	Yes	NIPDAU	Level-2-260C-1 YEAR	-40 to 125	14KV
OPA388IDBVT	Active	Production	SOT-23 (DBV) | 5	250 | SMALL T&R	Yes	NIPDAU	Level-2-260C-1 YEAR	-40 to 125	14KV
OPA388IDGKR	Active	Production	VSSOP (DGK) | 8	2500 | LARGE T&R	Yes	NIPDAUAG	Level-2-260C-1 YEAR	-40 to 125	14LV
OPA388IDGKT	Active	Production	VSSOP (DGK) | 8	250 | SMALL T&R	Yes	NIPDAUAG	Level-2-260C-1 YEAR	-40 to 125	14LV
OPA388IDR	Active	Production	SOIC (D) | 8	2500 | LARGE T&R	Yes	NIPDAU	Level-2-260C-1 YEAR	-40 to 125	OPA388
OPA4388ID	Active	Production	SOIC (D) | 14	50 | TUBE	Yes	NIPDAU	Level-2-260C-1 YEAR	-40 to 125	OPA4388
OPA4388IDR	Active	Production	SOIC (D) | 14	2500 | LARGE T&R	Yes	NIPDAU	Level-2-260C-1 YEAR	-40 to 125	OPA4388
OPA4388IPW	Active	Production	TSSOP (PW) | 14	90 | TUBE	Yes	NIPDAU	Level-2-260C-1 YEAR	-40 to 125	OPA4388
OPA4388IPWR	Active	Production	TSSOP (PW) | 14	2000 | LARGE T&R	Yes	NIPDAU	Level-2-260C-1 YEAR	-40 to 125	OPA4388

(1) **Status:** For more details on status, see our product life cycle.

(2) **Material type:** When designated, preproduction parts are prototypes/experimental devices, and are not yet approved or released for full production. Testing and final process, including without limitation quality assurance, reliability performance testing, and/or process qualification, may not yet be complete, and this item is subject to further changes or possible discontinuation. If available for ordering, purchases will be subject to an additional waiver at checkout, and are intended for early internal evaluation purposes only. These items are sold without warranties of any kind.

(3) **RoHS values:** Yes, No, RoHS Exempt. See the TI RoHS Statement for additional information and value definition.

(4) **Lead finish/Ball material:** Parts may have multiple material finish options. Finish options are separated by a vertical ruled line. Lead finish/Ball material values may wrap to two lines if the finish value exceeds the maximum column width.

(5) **MSL rating/Peak reflow:** The moisture sensitivity level ratings and peak solder (reflow) temperatures. In the event that a part has multiple moisture sensitivity ratings, only the lowest level per JEDEC standards is shown. Refer to the shipping label for the actual reflow temperature that will be used to mount the part to the printed circuit board.

(6) **Part marking:** There may be an additional marking, which relates to the logo, the lot trace code information, or the environmental category of the part.

Multiple part markings will be inside parentheses. Only one part marking contained in parentheses and separated by a "~" will appear on a part. If a line is indented then it is a continuation of the previous line and the two combined represent the entire part marking for that device.

OTHER QUALIFIED VERSIONS OF OPA2388, OPA388 :

- Automotive : OPA2388-Q1, OPA388-Q1

NOTE: Qualified Version Definitions:

- Automotive - Q100 devices qualified for high-reliability automotive applications targeting zero defects

TAPE AND REEL INFORMATION

REEL DIMENSIONS

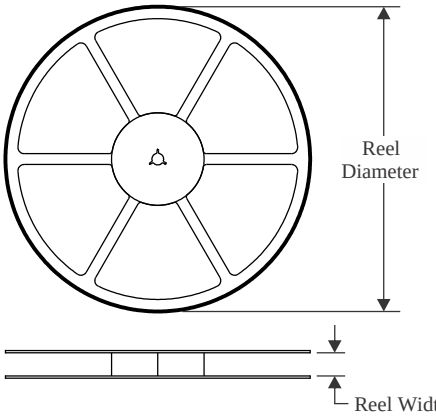

TAPE DIMENSIONS

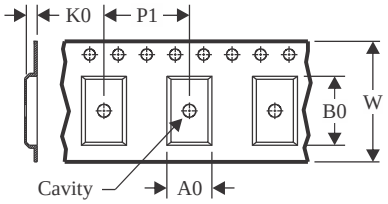

A0	Dimension designed to accommodate the component width
B0	Dimension designed to accommodate the component length
K0	Dimension designed to accommodate the component thickness
W	Overall width of the carrier tape
P1	Pitch between successive cavity centers

QUADRANT ASSIGNMENTS FOR PIN 1 ORIENTATION IN TAPE

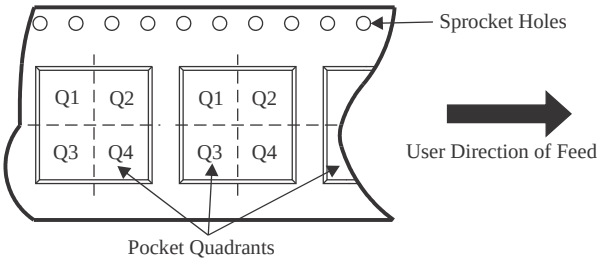

*All dimensions are nominal

Device	Package Type	Package Drawing	Pins	SPQ	Reel Diameter (mm)	Reel Width W1 (mm)	A0 (mm)	B0 (mm)	K0 (mm)	P1 (mm)	W (mm)	Pin1 Quadrant
OPA2388IDGKR	VSSOP	DGK	8	2500	330.0	12.4	5.25	3.35	1.25	8.0	12.0	Q1
OPA2388IDGKT	VSSOP	DGK	8	250	330.0	12.4	5.25	3.35	1.25	8.0	12.0	Q1
OPA2388IDR	SOIC	D	8	2500	330.0	12.8	6.4	5.2	2.1	8.0	12.0	Q1
OPA388IDBVR	SOT-23	DBV	5	3000	180.0	8.4	3.23	3.17	1.37	4.0	8.0	Q3
OPA388IDBVT	SOT-23	DBV	5	250	180.0	8.4	3.23	3.17	1.37	4.0	8.0	Q3
OPA388IDGKR	VSSOP	DGK	8	2500	330.0	12.4	5.3	3.4	1.4	8.0	12.0	Q1
OPA388IDGKT	VSSOP	DGK	8	250	330.0	12.4	5.3	3.4	1.4	8.0	12.0	Q1
OPA388IDR	SOIC	D	8	2500	330.0	12.4	6.4	5.2	2.1	8.0	12.0	Q1
OPA4388IDR	SOIC	D	14	2500	330.0	16.4	6.5	9.0	2.1	8.0	16.0	Q1
OPA4388IPWR	TSSOP	PW	14	2000	330.0	12.4	6.9	5.6	1.6	8.0	12.0	Q1

TAPE AND REEL BOX DIMENSIONS

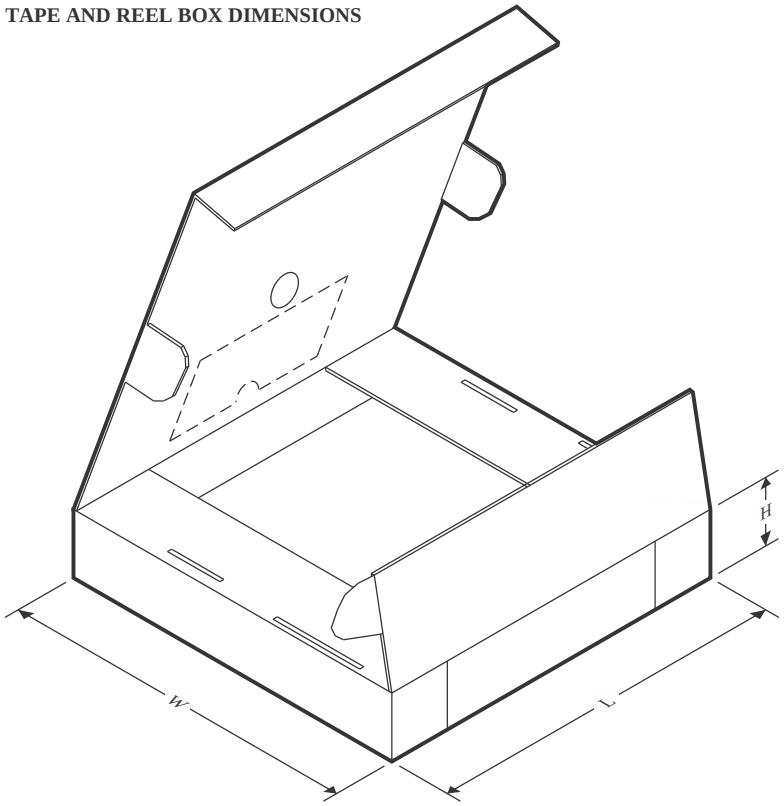

*All dimensions are nominal

Device	Package Type	Package Drawing	Pins	SPQ	Length (mm)	Width (mm)	Height (mm)
OPA2388IDGKR	VSSOP	DGK	8	2500	366.0	364.0	50.0
OPA2388IDGKT	VSSOP	DGK	8	250	366.0	364.0	50.0
OPA2388IDR	SOIC	D	8	2500	366.0	364.0	50.0
OPA388IDBVR	SOT-23	DBV	5	3000	213.0	191.0	35.0
OPA388IDBVT	SOT-23	DBV	5	250	213.0	191.0	35.0
OPA388IDGKR	VSSOP	DGK	8	2500	366.0	364.0	50.0
OPA388IDGKT	VSSOP	DGK	8	250	366.0	364.0	50.0
OPA388IDR	SOIC	D	8	2500	356.0	356.0	35.0
OPA4388IDR	SOIC	D	14	2500	356.0	356.0	35.0
OPA4388IPWR	TSSOP	PW	14	2000	356.0	356.0	35.0

TUBE

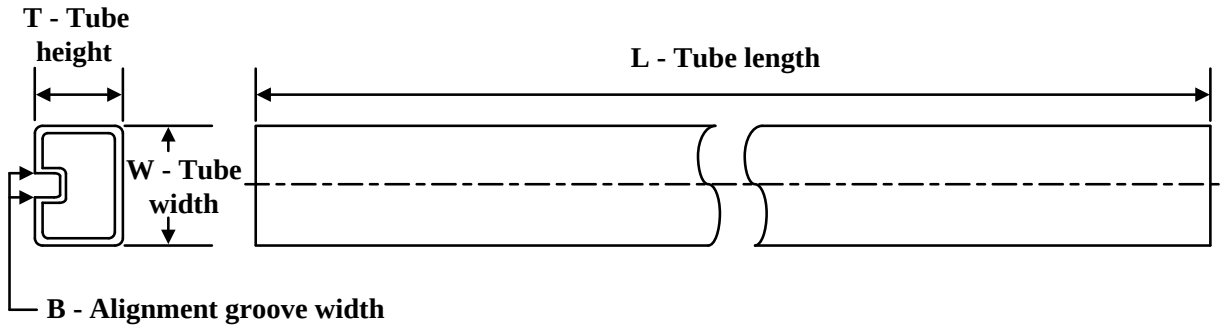

*All dimensions are nominal

Device	Package Name	Package Type	Pins	SPQ	L (mm)	W (mm)	T (µm)	B (mm)
OPA2388ID	D	SOIC	8	75	517	7.87	635	4.25
OPA388ID	D	SOIC	8	75	506.6	8	3940	4.32
OPA4388ID	D	SOIC	14	50	506.6	8	3940	4.32
OPA4388IPW	PW	TSSOP	14	90	530	10.2	3600	3.5

PACKAGE OUTLINE

DBV0005A

SOT-23 - 1.45 mm max height

SMALL OUTLINE TRANSISTOR

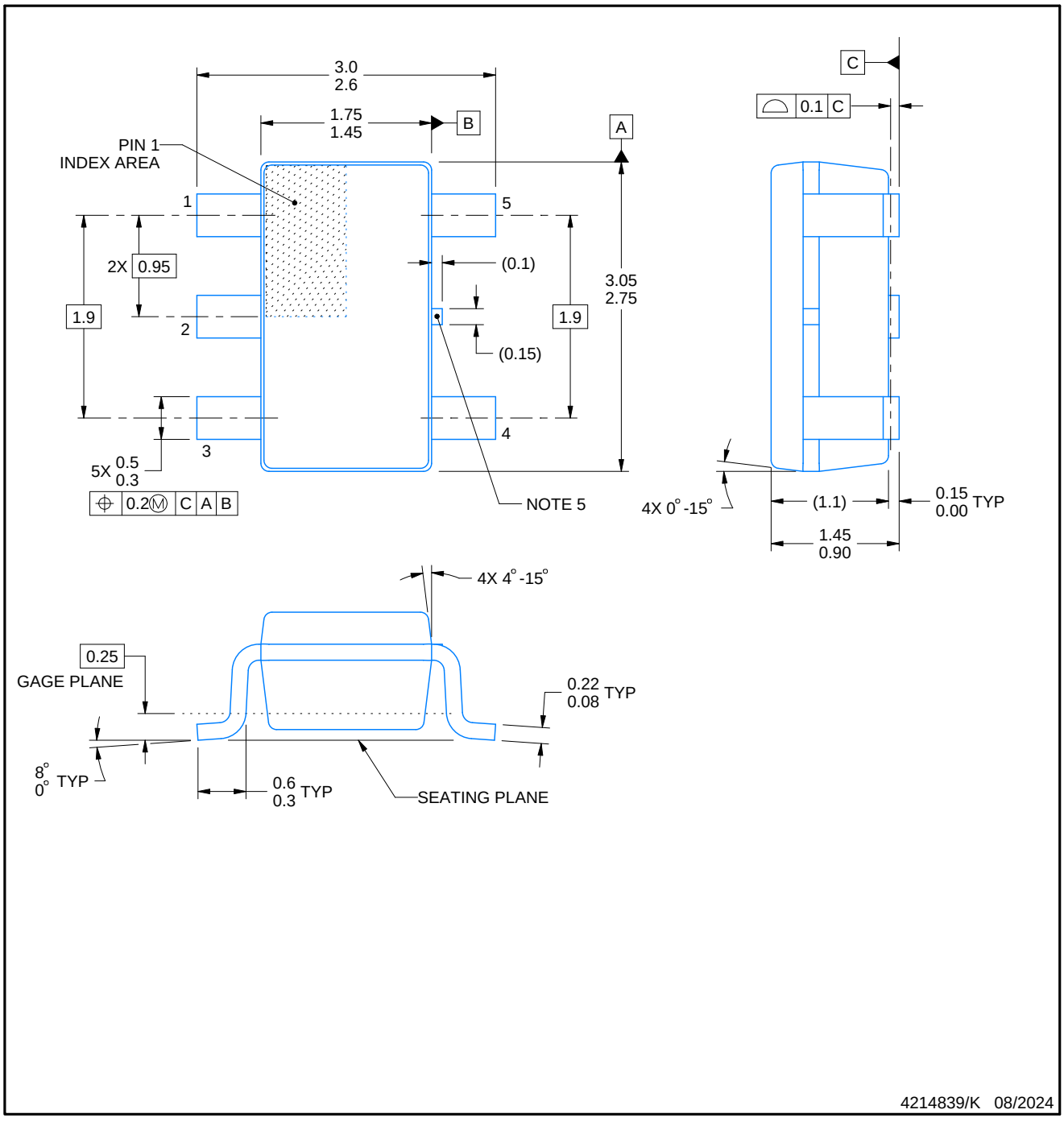

NOTES:

1. All linear dimensions are in millimeters. Any dimensions in parenthesis are for reference only. Dimensioning and tolerancing per ASME Y14.5M.
2. This drawing is subject to change without notice.
3. Refernce JEDEC MO-178.
4. Body dimensions do not include mold flash, protrusions, or gate burrs. Mold flash, protrusions, or gate burrs shall not exceed 0.25 mm per side.
5. Support pin may differ or may not be present.

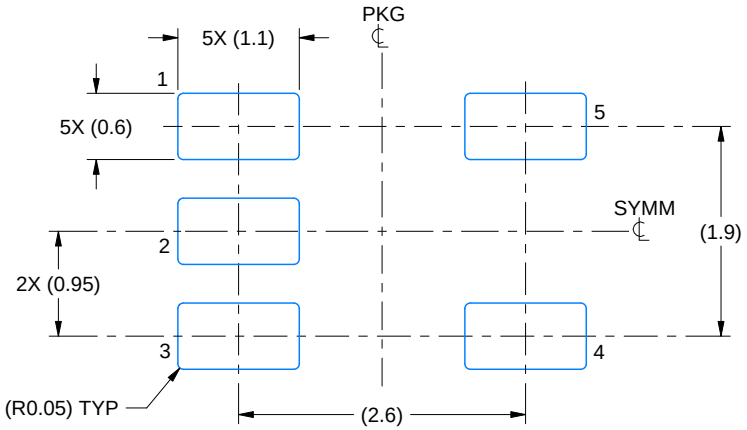

LAND PATTERN EXAMPLE
EXPOSED METAL SHOWN
SCALE:15X

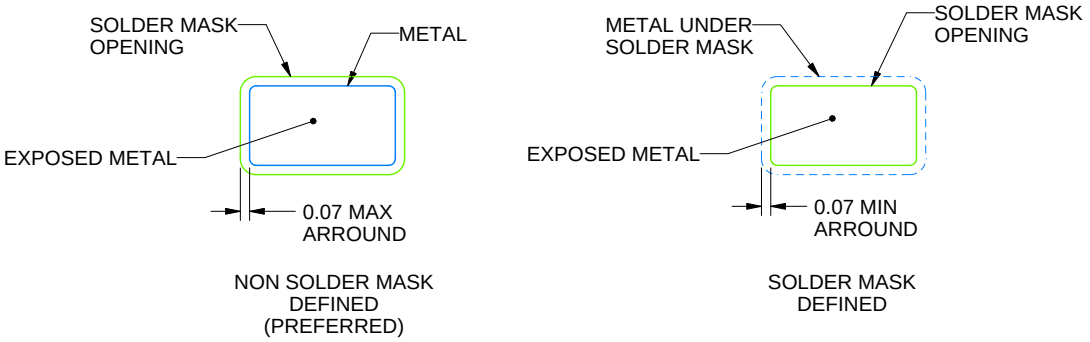

SOLDER MASK DETAILS

4214839/K 08/2024

NOTES: (continued)

6. Publication IPC-7351 may have alternate designs.
7. Solder mask tolerances between and around signal pads can vary based on board fabrication site.

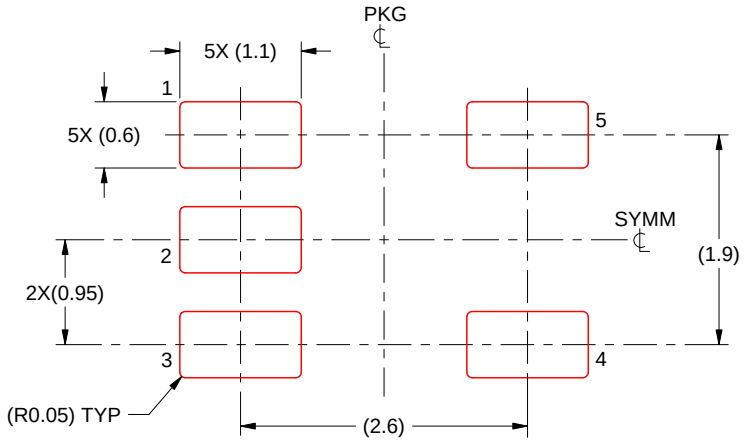

SOLDER PASTE EXAMPLE
BASED ON 0.125 mm THICK STENCIL
SCALE:15X

4214839/K 08/2024

NOTES: (continued)

8. Laser cutting apertures with trapezoidal walls and rounded corners may offer better paste release. IPC-7525 may have alternate design recommendations.
9. Board assembly site may have different recommendations for stencil design.

PACKAGE OUTLINE

DGK0008A

VSSOP - 1.1 mm max height

SMALL OUTLINE PACKAGE

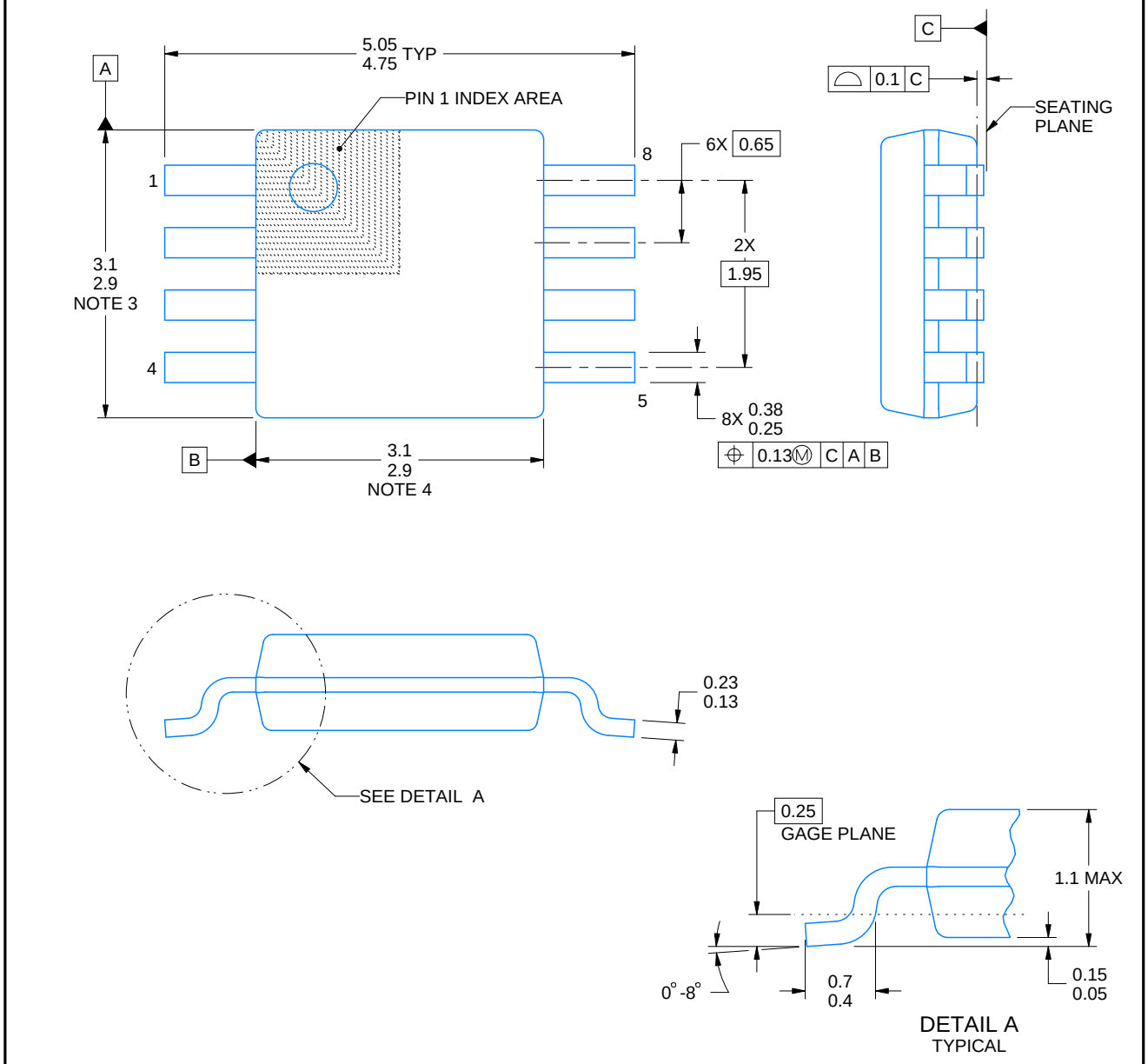

PowerPAD is a trademark of Texas Instruments.

NOTES:

1. All linear dimensions are in millimeters. Any dimensions in parenthesis are for reference only. Dimensioning and tolerancing per ASME Y14.5M.
2. This drawing is subject to change without notice.
3. This dimension does not include mold flash, protrusions, or gate burrs. Mold flash, protrusions, or gate burrs shall not exceed 0.15 mm per side.
4. This dimension does not include interlead flash. Interlead flash shall not exceed 0.25 mm per side.
5. Reference JEDEC registration MO-187.

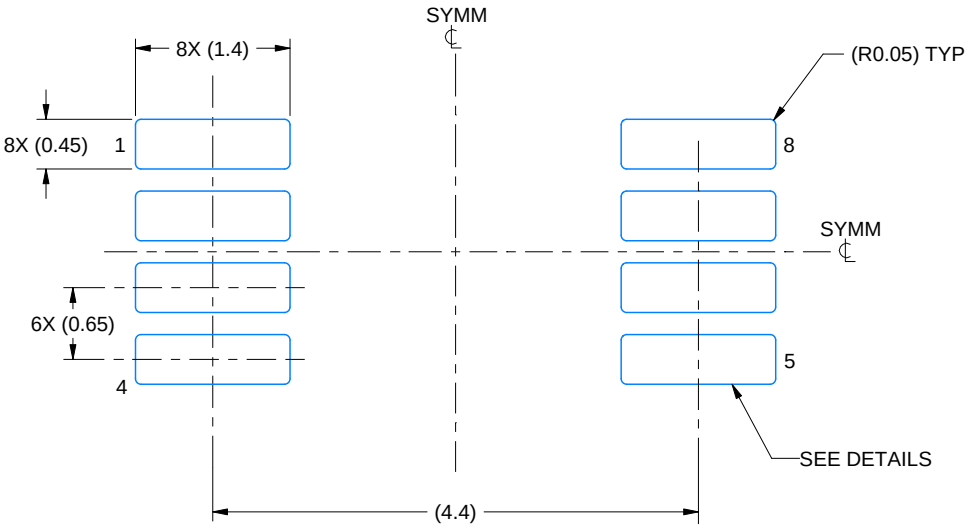

LAND PATTERN EXAMPLE
EXPOSED METAL SHOWN
SCALE: 15X

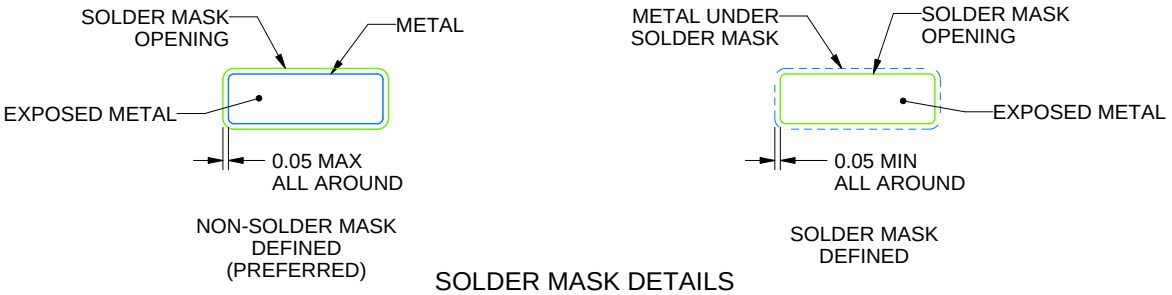

SOLDER MASK DETAILS

4214862/A 04/2023

NOTES: (continued)

6. Publication IPC-7351 may have alternate designs.
7. Solder mask tolerances between and around signal pads can vary based on board fabrication site.
8. Vias are optional depending on application, refer to device data sheet. If any vias are implemented, refer to their locations shown on this view. It is recommended that vias under paste be filled, plugged or tented.
9. Size of metal pad may vary due to creepage requirement.

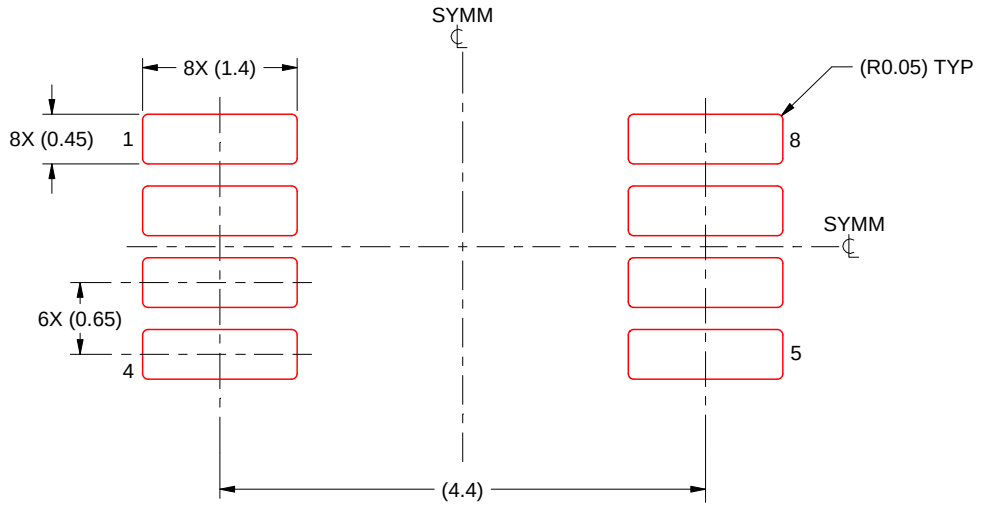

SOLDER PASTE EXAMPLE
SCALE: 15X

4214862/A 04/2023

NOTES: (continued)

11. Laser cutting apertures with trapezoidal walls and rounded corners may offer better paste release. IPC-7525 may have alternate design recommendations.
12. Board assembly site may have different recommendations for stencil design.

PACKAGE OUTLINE

D0014A

SOIC - 1.75 mm max height

SMALL OUTLINE INTEGRATED CIRCUIT

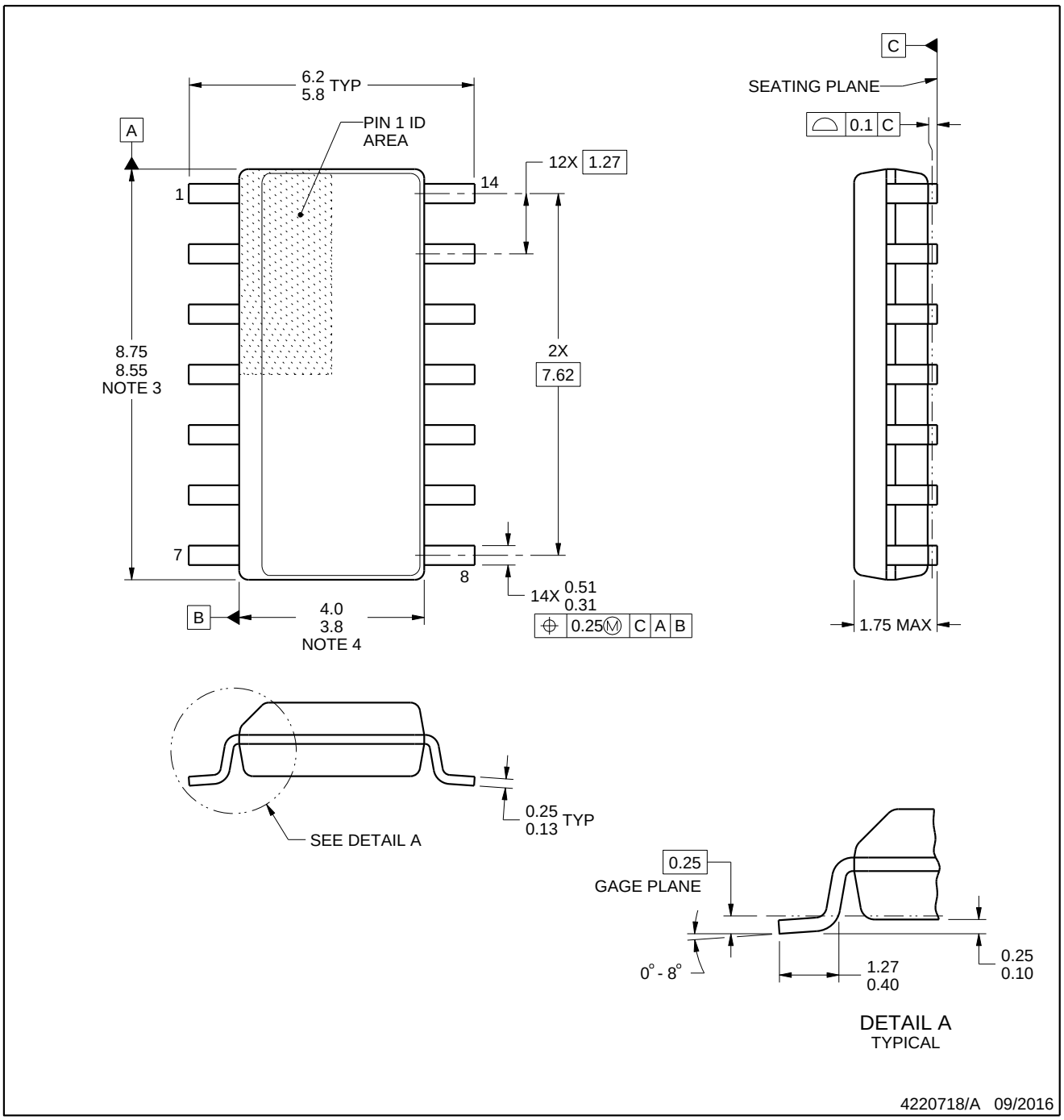

NOTES:

1. All linear dimensions are in millimeters. Dimensions in parenthesis are for reference only. Dimensioning and tolerancing per ASME Y14.5M.
2. This drawing is subject to change without notice.
3. This dimension does not include mold flash, protrusions, or gate burrs. Mold flash, protrusions, or gate burrs shall not exceed 0.15 mm, per side.
4. This dimension does not include interlead flash. Interlead flash shall not exceed 0.43 mm, per side.
5. Reference JEDEC registration MS-012, variation AB.

EXAMPLE BOARD LAYOUT

D0014A

SOIC - 1.75 mm max height

SMALL OUTLINE INTEGRATED CIRCUIT

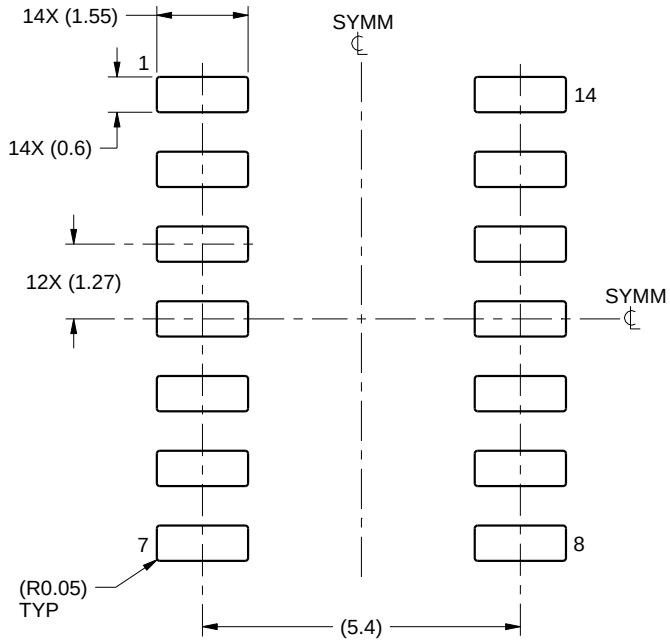

LAND PATTERN EXAMPLE
SCALE:8X

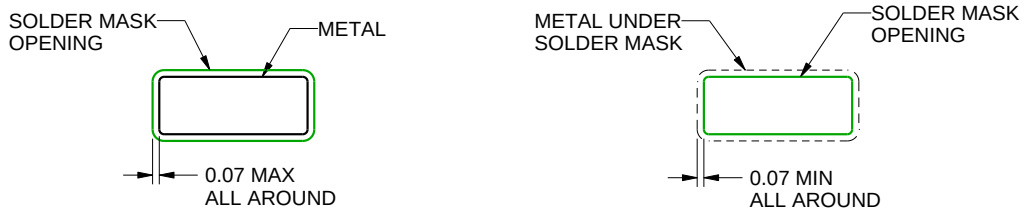

SOLDER MASK DETAILS

4220718/A 09/2016

NOTES: (continued)

6. Publication IPC-7351 may have alternate designs.
7. Solder mask tolerances between and around signal pads can vary based on board fabrication site.

EXAMPLE STENCIL DESIGN

D0014A

SOIC - 1.75 mm max height

SMALL OUTLINE INTEGRATED CIRCUIT

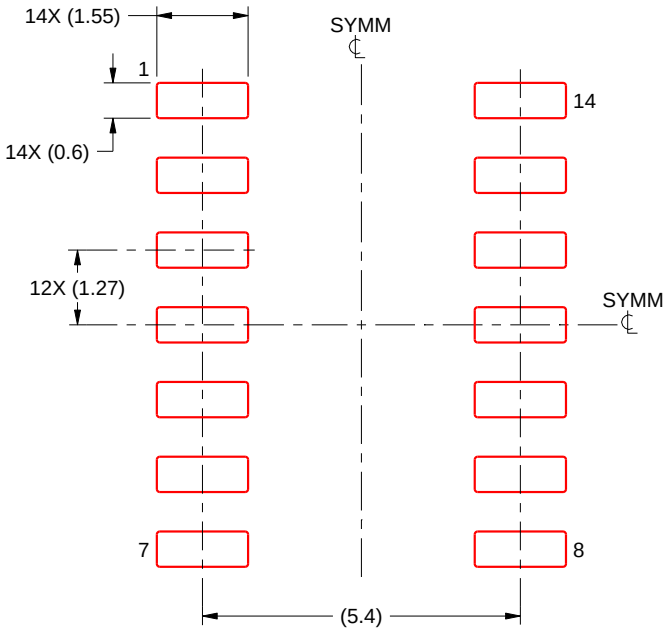

SOLDER PASTE EXAMPLE
BASED ON 0.125 mm THICK STENCIL
SCALE:8X

4220718/A 09/2016

NOTES: (continued)

8. Laser cutting apertures with trapezoidal walls and rounded corners may offer better paste release. IPC-7525 may have alternate design recommendations.
9. Board assembly site may have different recommendations for stencil design.

PACKAGE OUTLINE

D0008A

SOIC - 1.75 mm max height

SMALL OUTLINE INTEGRATED CIRCUIT

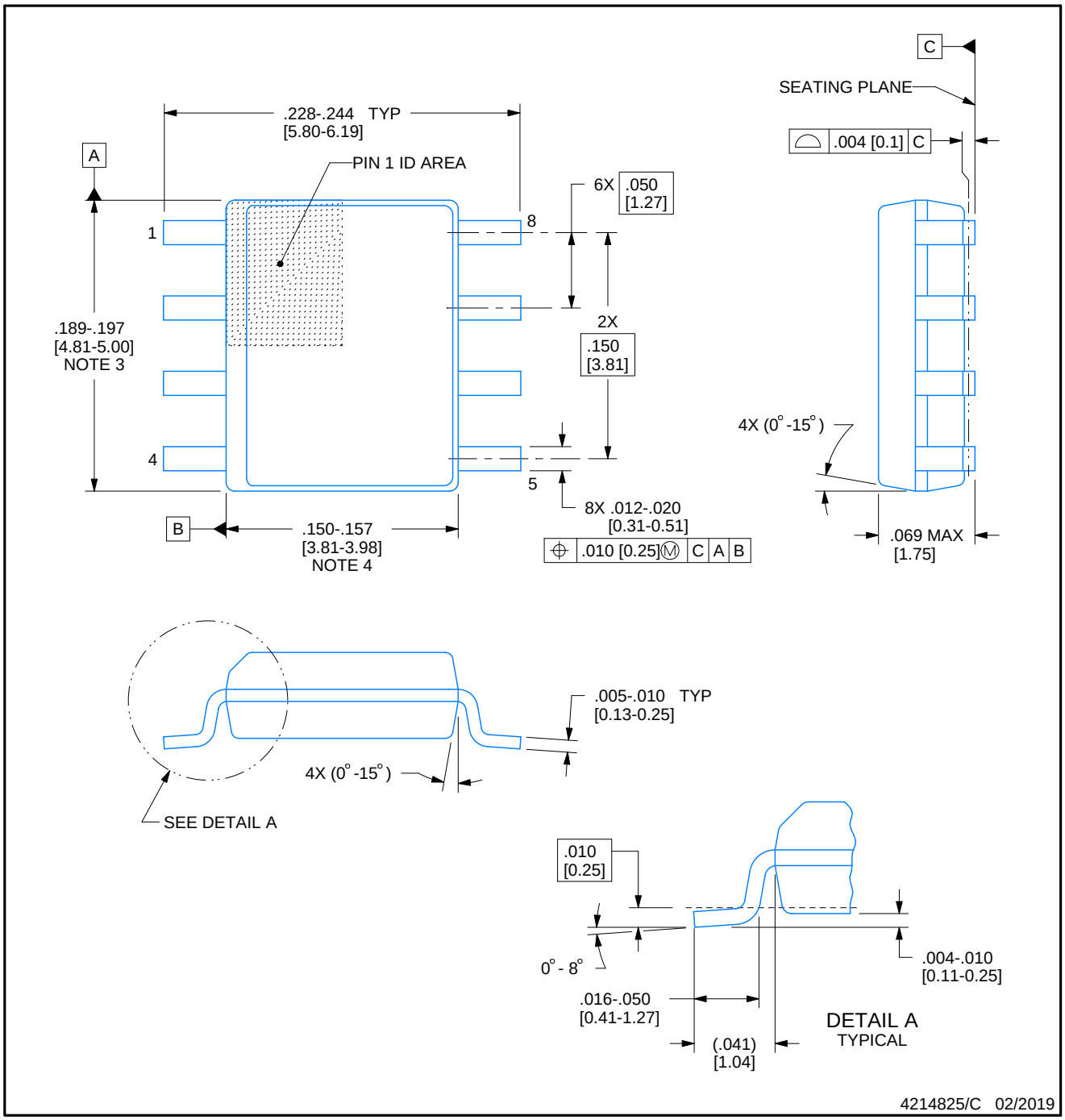

NOTES:

1. Linear dimensions are in inches [millimeters]. Dimensions in parenthesis are for reference only. Controlling dimensions are in inches. Dimensioning and tolerancing per ASME Y14.5M.
2. This drawing is subject to change without notice.
3. This dimension does not include mold flash, protrusions, or gate burrs. Mold flash, protrusions, or gate burrs shall not exceed .006 [0.15] per side.
4. This dimension does not include interlead flash.
5. Reference JEDEC registration MS-012, variation AA.

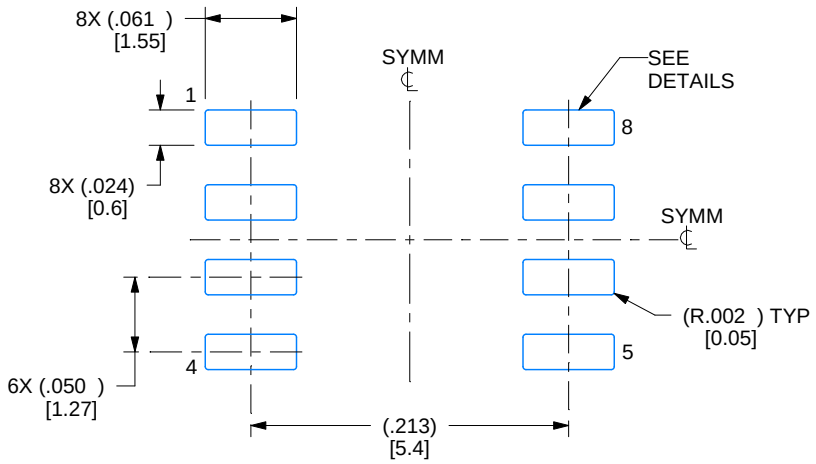

LAND PATTERN EXAMPLE
EXPOSED METAL SHOWN
SCALE:8X

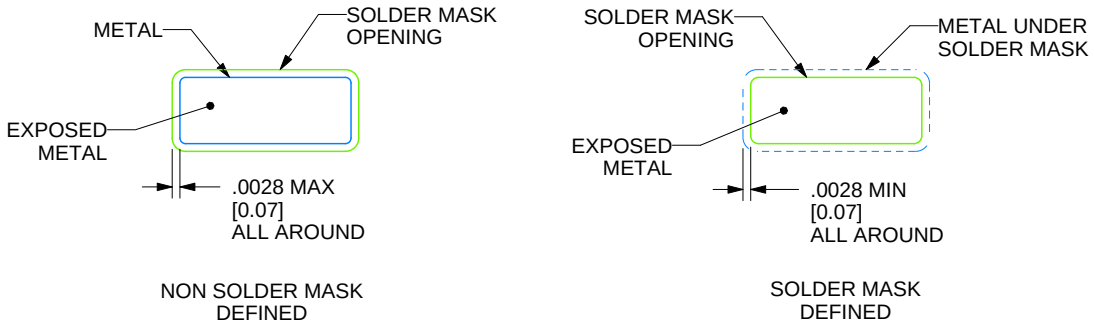

SOLDER MASK DETAILS

4214825/C 02/2019

NOTES: (continued)

6. Publication IPC-7351 may have alternate designs.
7. Solder mask tolerances between and around signal pads can vary based on board fabrication site.

EXAMPLE STENCIL DESIGN

D0008A

SOIC - 1.75 mm max height

SMALL OUTLINE INTEGRATED CIRCUIT

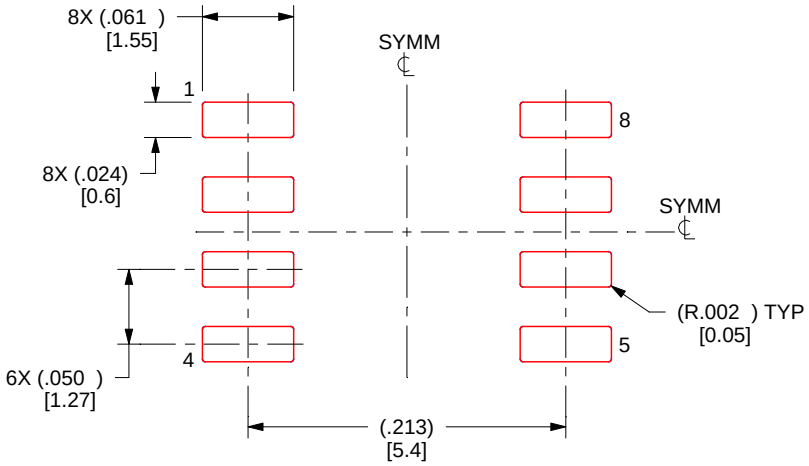

SOLDER PASTE EXAMPLE
BASED ON .005 INCH [0.125 MM] THICK STENCIL
SCALE:8X

4214825/C 02/2019

NOTES: (continued)

8. Laser cutting apertures with trapezoidal walls and rounded corners may offer better paste release. IPC-7525 may have alternate design recommendations.
9. Board assembly site may have different recommendations for stencil design.

PACKAGE OUTLINE

PW0014A

TSSOP - 1.2 mm max height

SMALL OUTLINE PACKAGE

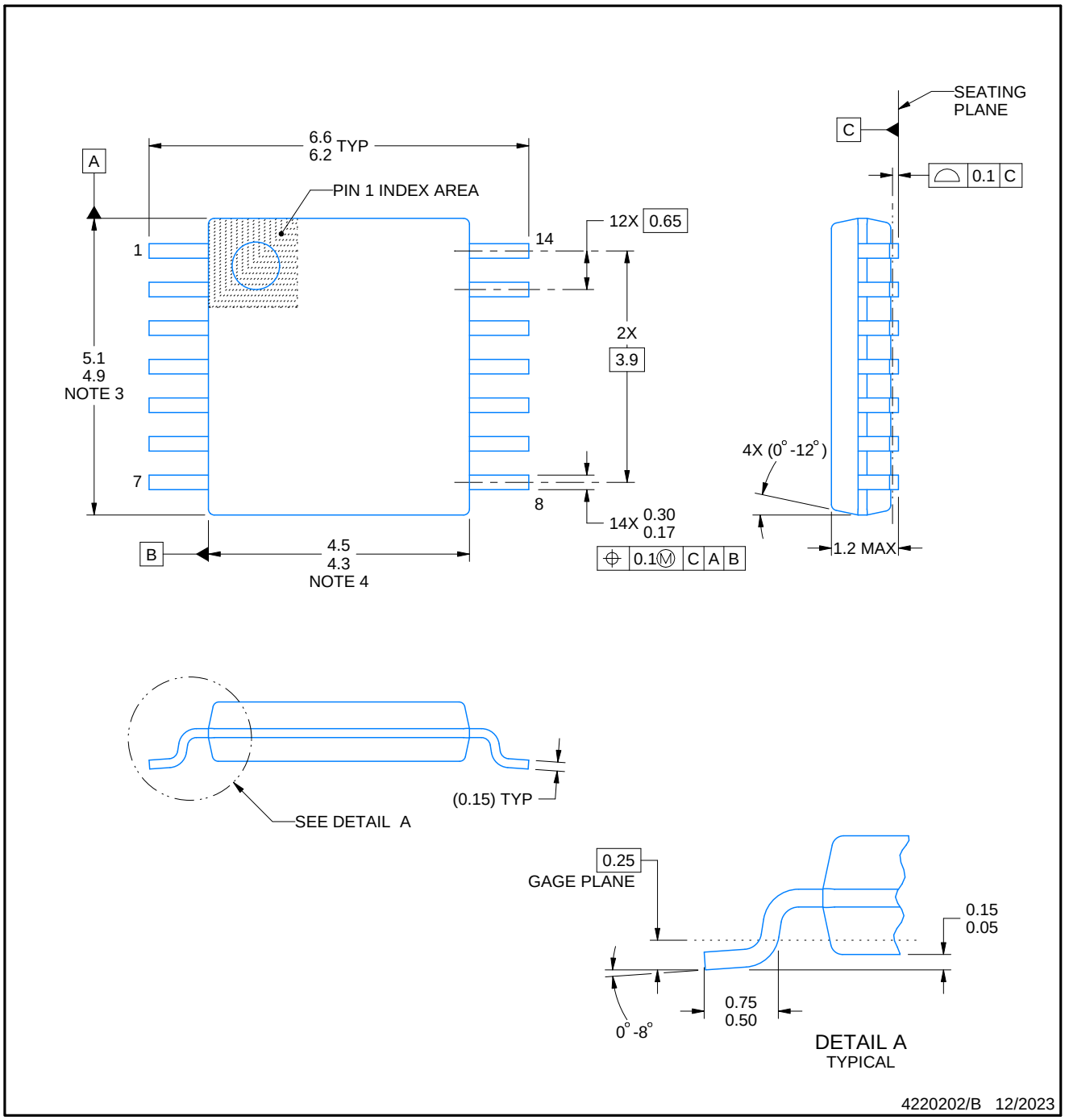

NOTES:

1. All linear dimensions are in millimeters. Any dimensions in parenthesis are for reference only. Dimensioning and tolerancing per ASME Y14.5M.
2. This drawing is subject to change without notice.
3. This dimension does not include mold flash, protrusions, or gate burrs. Mold flash, protrusions, or gate burrs shall not exceed 0.15 mm per side.
4. This dimension does not include interlead flash. Interlead flash shall not exceed 0.25 mm per side.
5. Reference JEDEC registration MO-153.

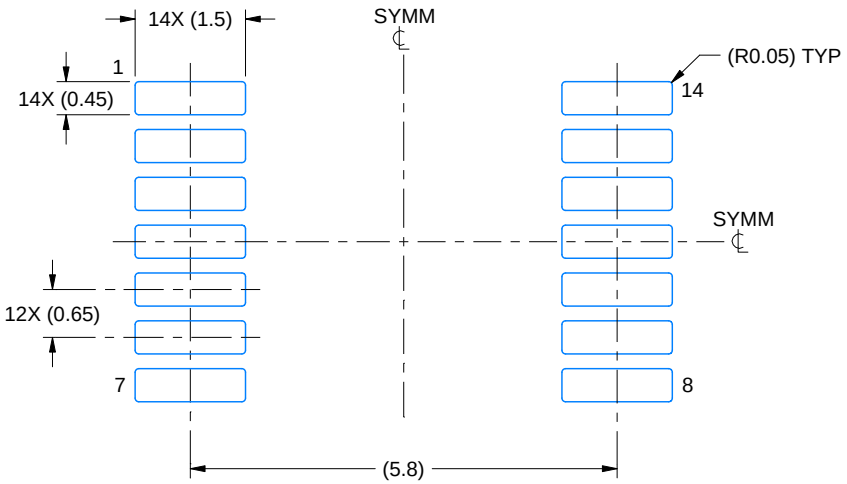

LAND PATTERN EXAMPLE
EXPOSED METAL SHOWN
SCALE: 10X

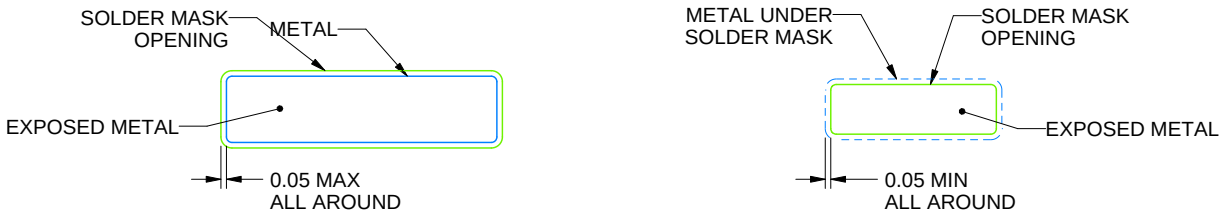

SOLDER MASK DETAILS

4220202/B 12/2023

NOTES: (continued)

6. Publication IPC-7351 may have alternate designs.
7. Solder mask tolerances between and around signal pads can vary based on board fabrication site.

EXAMPLE STENCIL DESIGN

PW0014A

TSSOP - 1.2 mm max height

SMALL OUTLINE PACKAGE

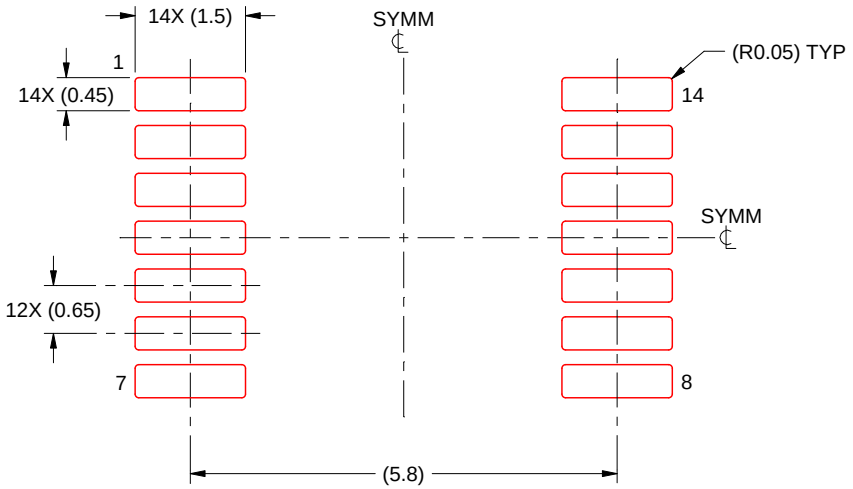

SOLDER PASTE EXAMPLE
BASED ON 0.125 mm THICK STENCIL
SCALE: 10X

4220202/B 12/2023

NOTES: (continued)

8. Laser cutting apertures with trapezoidal walls and rounded corners may offer better paste release. IPC-7525 may have alternate design recommendations.
9. Board assembly site may have different recommendations for stencil design.

IMPORTANT NOTICE AND DISCLAIMER

TI PROVIDES TECHNICAL AND RELIABILITY DATA (INCLUDING DATA SHEETS), DESIGN RESOURCES (INCLUDING REFERENCE DESIGNS), APPLICATION OR OTHER DESIGN ADVICE, WEB TOOLS, SAFETY INFORMATION, AND OTHER RESOURCES “AS IS” AND WITH ALL FAULTS, AND DISCLAIMS ALL WARRANTIES, EXPRESS AND IMPLIED, INCLUDING WITHOUT LIMITATION ANY IMPLIED WARRANTIES OF MERCHANTABILITY, FITNESS FOR A PARTICULAR PURPOSE OR NON-INFRINGEMENT OF THIRD PARTY INTELLECTUAL PROPERTY RIGHTS.

These resources are intended for skilled developers designing with TI products. You are solely responsible for (1) selecting the appropriate TI products for your application, (2) designing, validating and testing your application, and (3) ensuring your application meets applicable standards, and any other safety, security, regulatory or other requirements.

These resources are subject to change without notice. TI grants you permission to use these resources only for development of an application that uses the TI products described in the resource. Other reproduction and display of these resources is prohibited. No license is granted to any other TI intellectual property right or to any third party intellectual property right. TI disclaims responsibility for, and you will fully indemnify TI and its representatives against, any claims, damages, costs, losses, and liabilities arising out of your use of these resources.

TI’s products are provided subject to TI’s Terms of Sale or other applicable terms available either on ti.com or provided in conjunction with such TI products. TI’s provision of these resources does not expand or otherwise alter TI’s applicable warranties or warranty disclaimers for TI products.

TI objects to and rejects any additional or different terms you may have proposed.

Mailing Address: Texas Instruments, Post Office Box 655303, Dallas, Texas 75265